DNA Brick Crystals with Prescribed Depth
Supplementary Information 1

Contents

List of Figures

S1 Summary figure

Fig. S1. DNA crystals with prescribed depth and 3D features.

Artificially aligned

S2   Design strategy for DNA-brick crystals
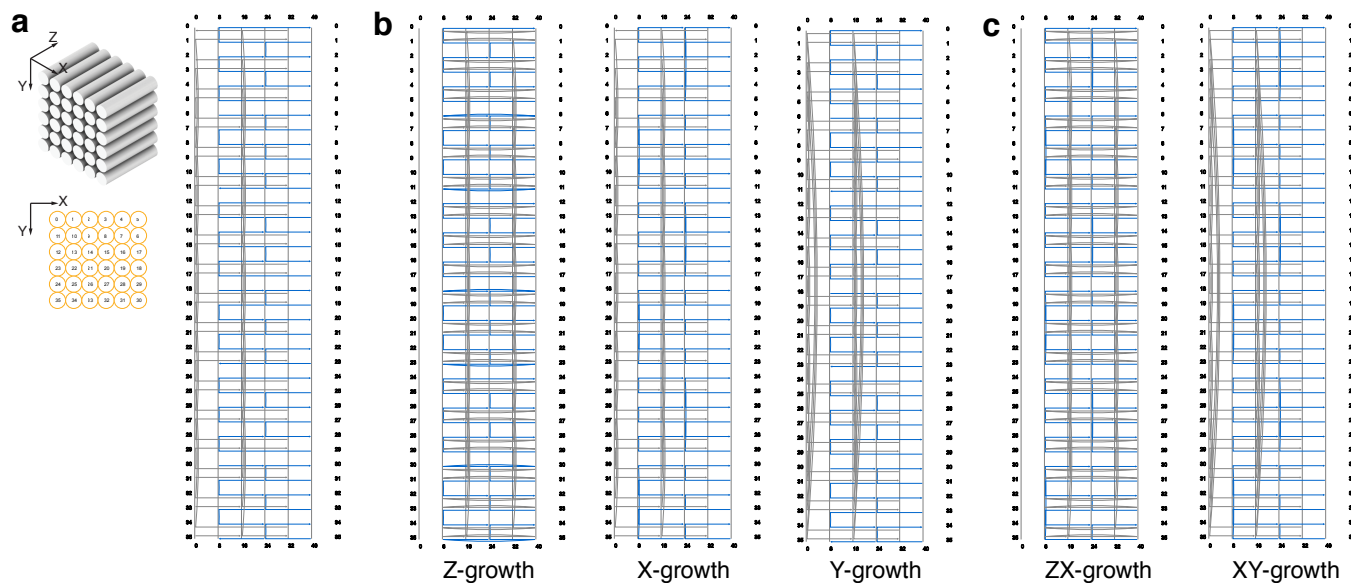
Fig. S2. Strand diagrams illustrating connecting patterns of DNA crystals. a, Top-left, a 6H×6H×24B cuboid discrete DNA-brick structure. Bottom-left, the intersection perpendicular to the DNA helices of the 6H×6H×24B cuboid. Right, the detailed strand diagram of the 6H×6H×24B cuboid. The numbers on the left and the right indicate the helices. The numbers on the top and the bottom indicate the position of the base-pairs along the Z-axis. X-bricks are represented with blue lines, and Y-bricks are represented with gray lines. **b**, Connection patterns of one-dimensional: Z-growth, X-growth, and Y-growth. **c**, Connection patterns of two-dimensional: ZX-growth and XY-growth. Zoom in to see details.

S3 One-dimensional crystals (Z-crystals and X-crystals)

S3.1 TEM images of Z-crystals

Figs. S3 to S11 show TEM images of various Z crystals
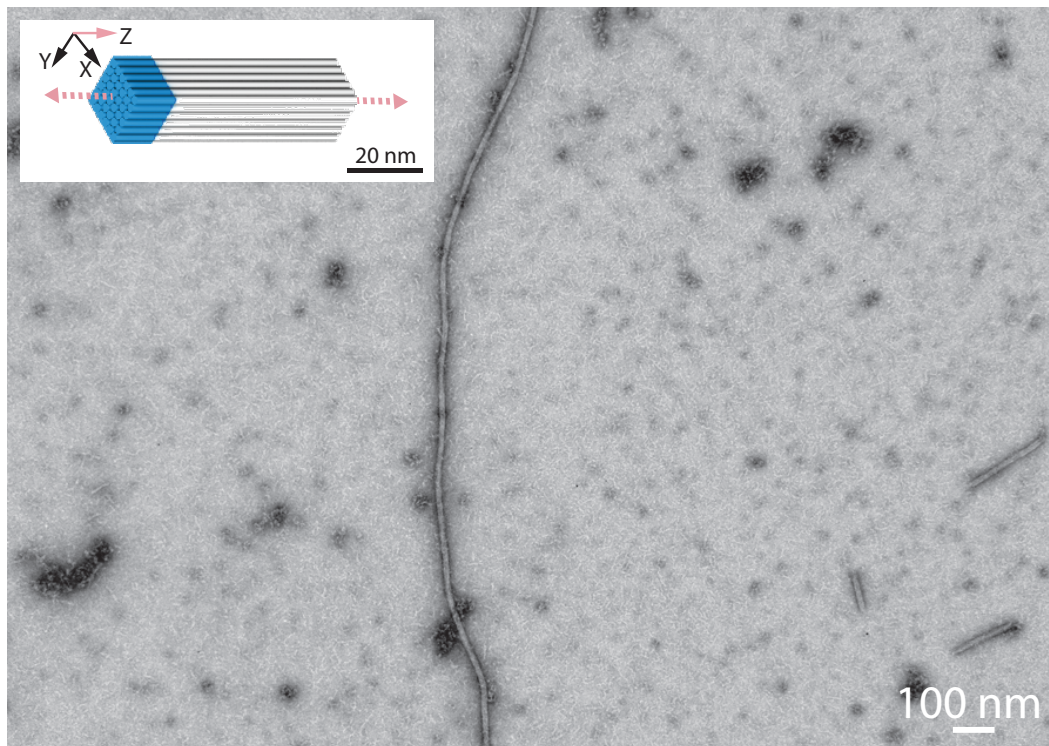
Fig. S3. TEM image of the Z-6H×6H×32B-cuboid crystal.
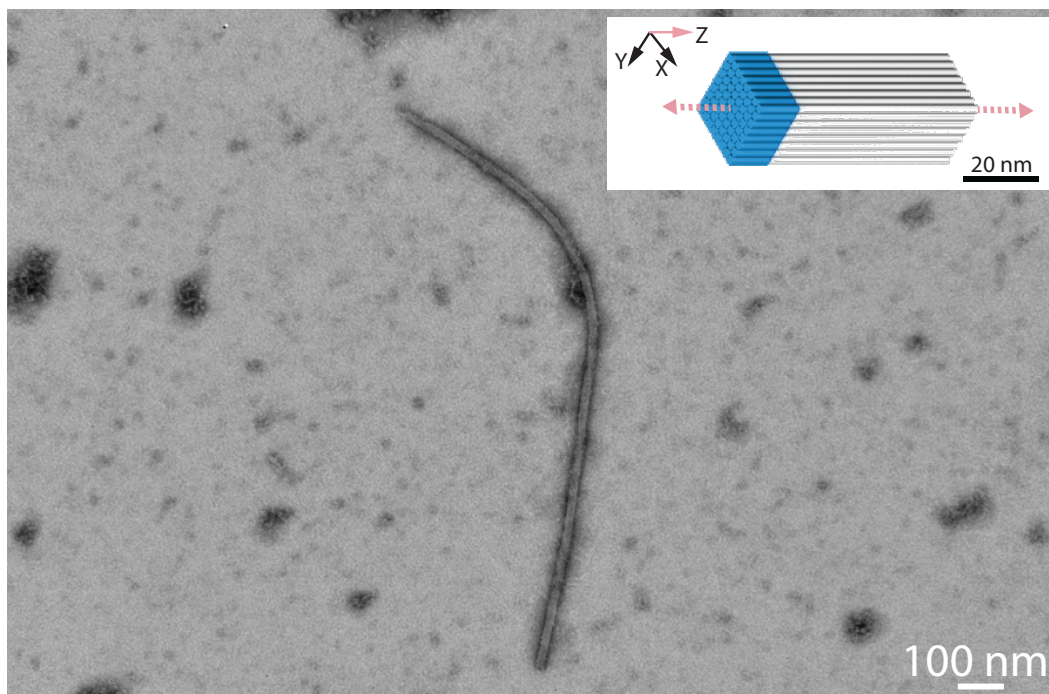
Fig. S4. TEM image of the Z-8H×8H×32B-cuboid crystal.
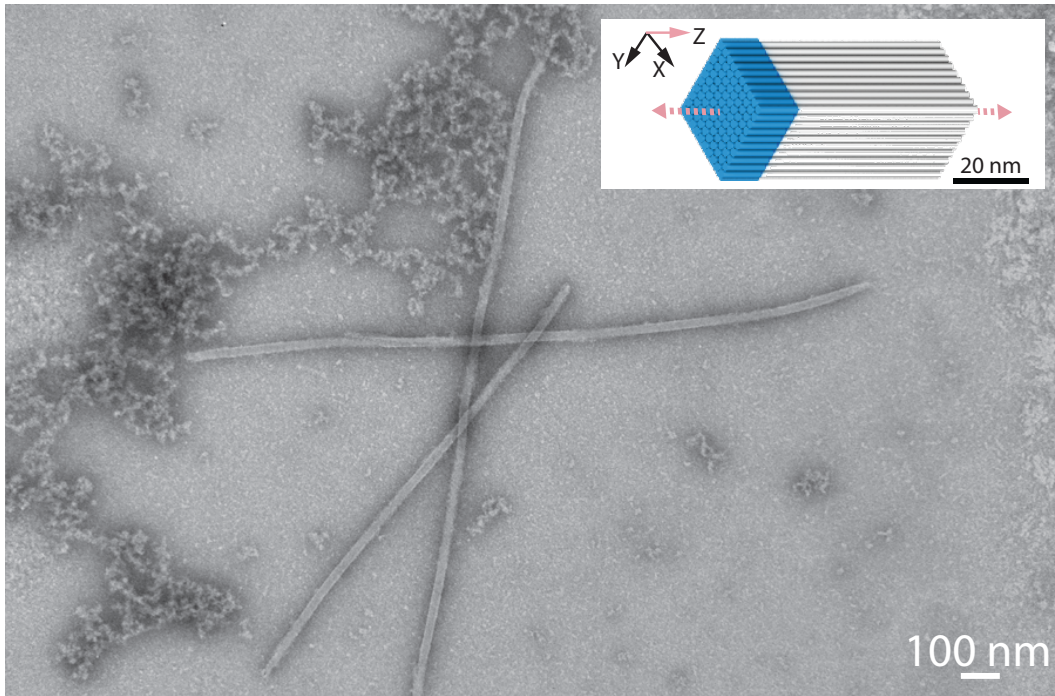
Fig. S5. TEM image of the Z-10H×10H×32B-cuboid crystal.
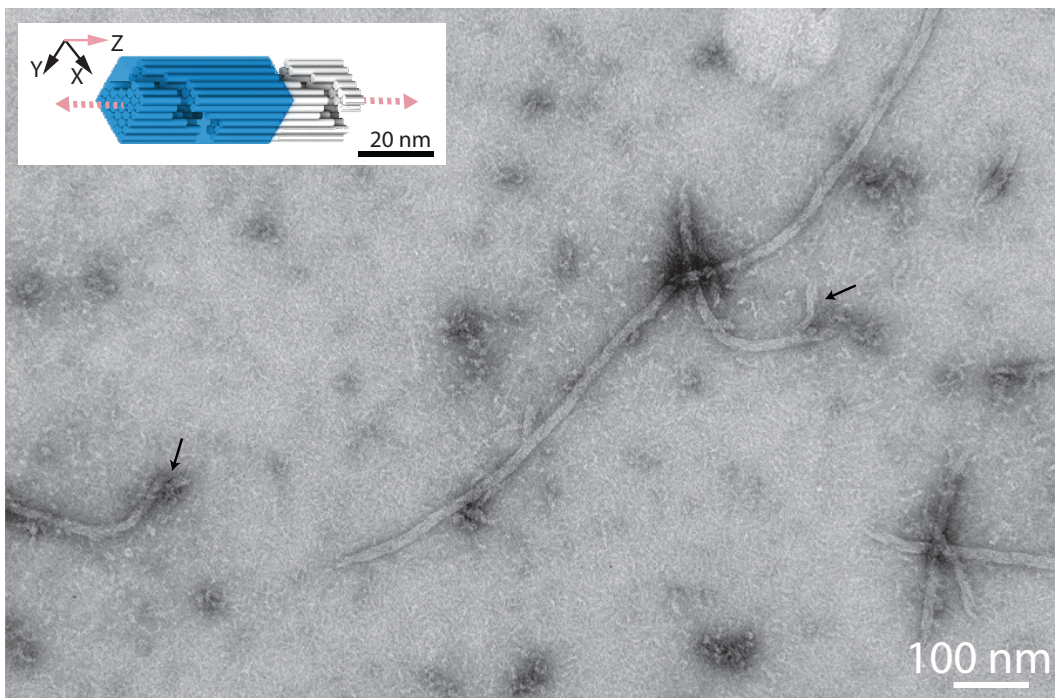
Fig. S6. TEM image of the Z-6H×6H×128B-spiral crystal. Arrows point to broken structures observed.
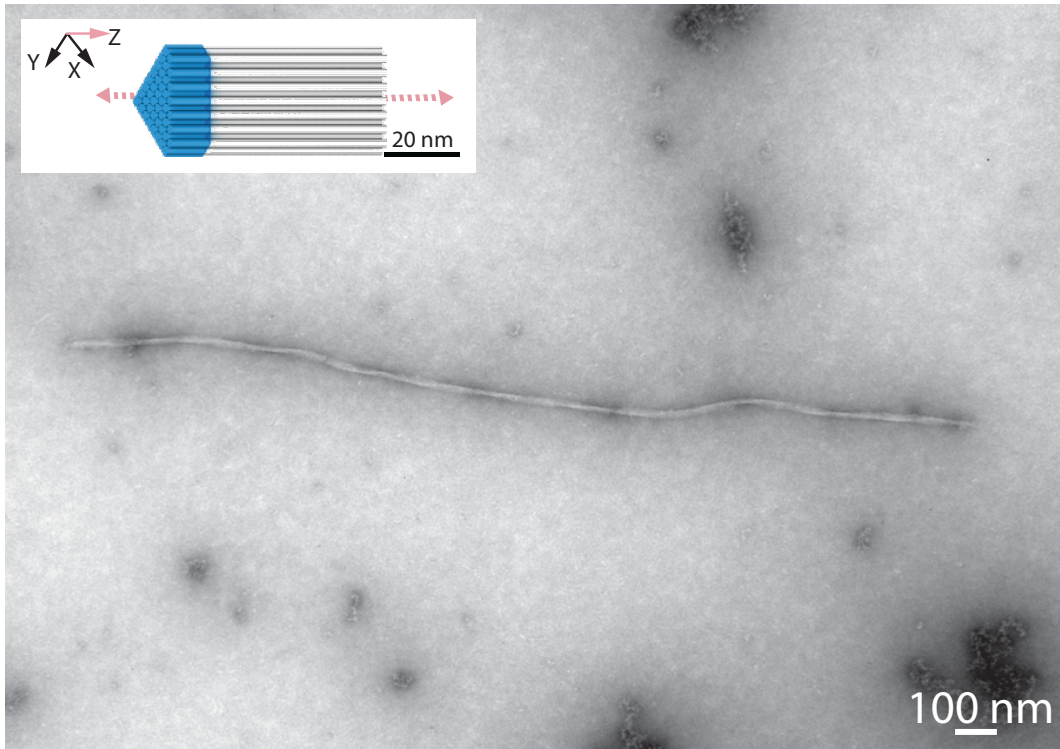
Fig. S7. TEM image of the Z-43H×32B-triangle crystal.
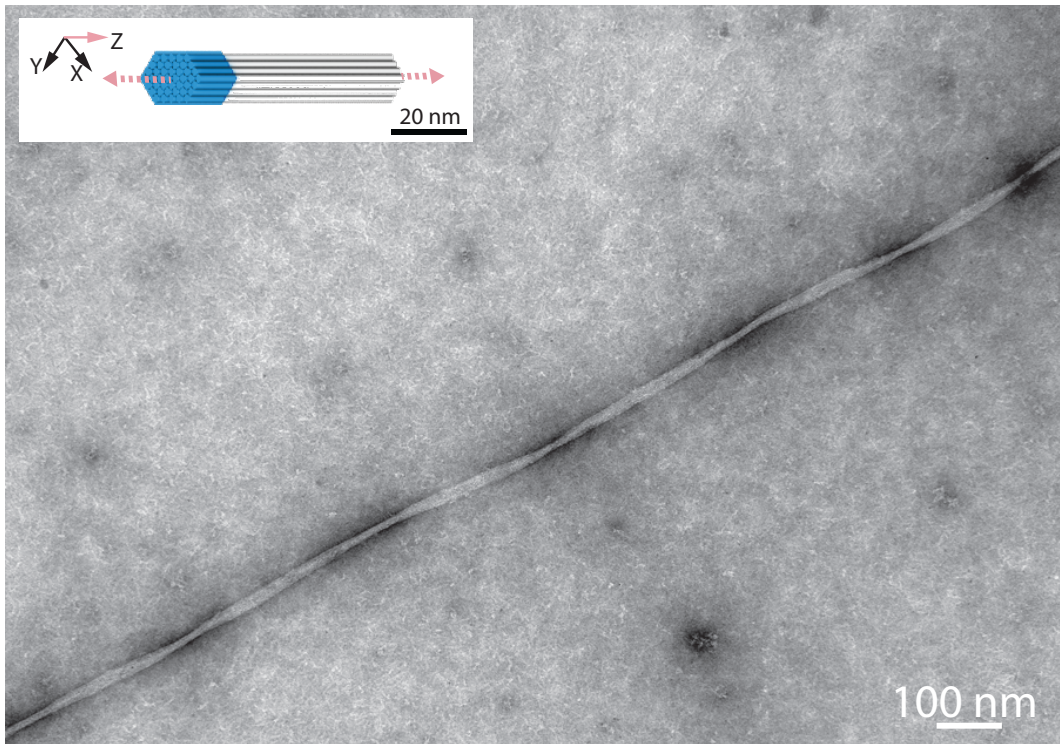
Fig. S8. TEM image of the Z-44H×32B-hexagon crystal.
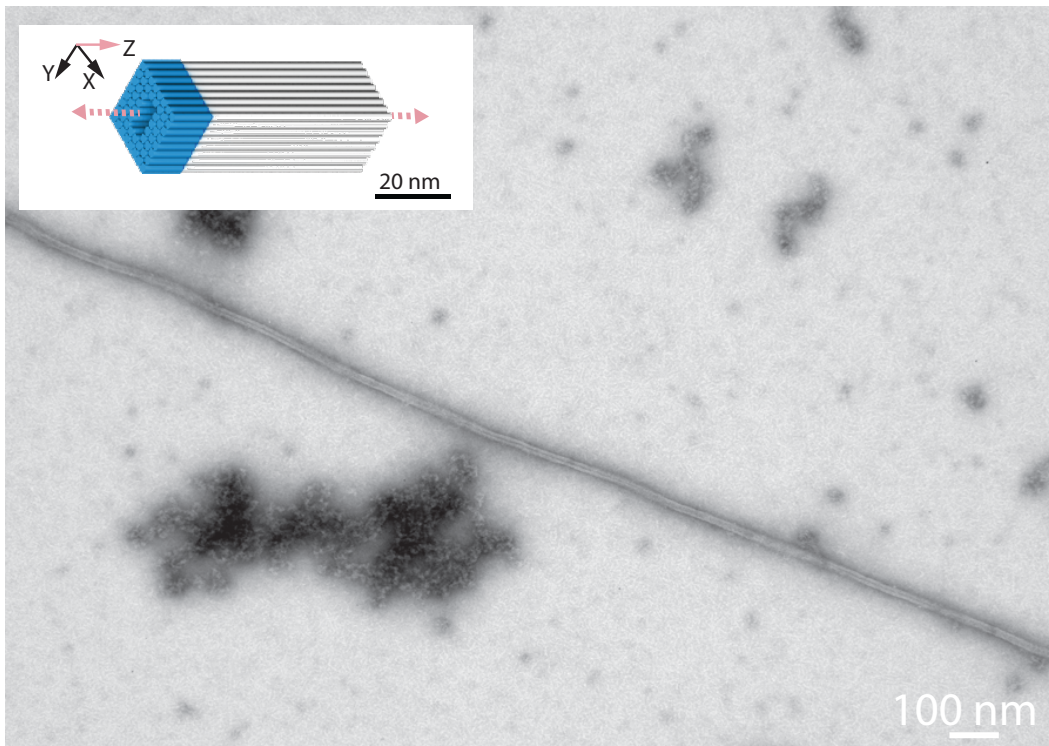
Fig. S9. TEM image of the Z-56H×32B-tunnel crystal.
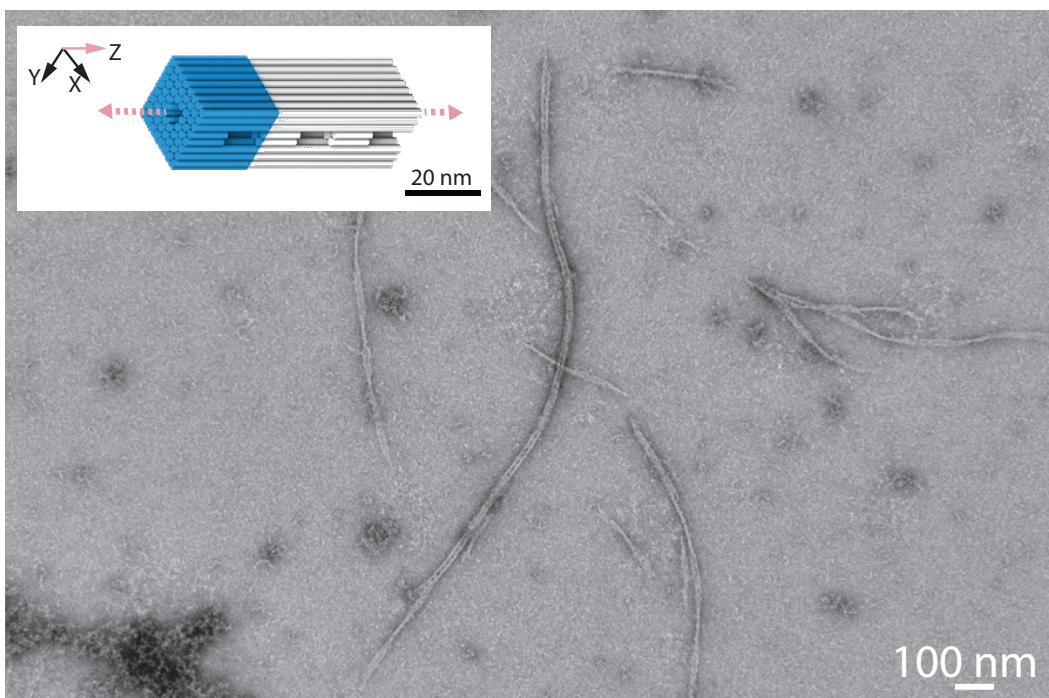
Fig. S10. TEM image of the Z-60H×64B-tunnel crystal.
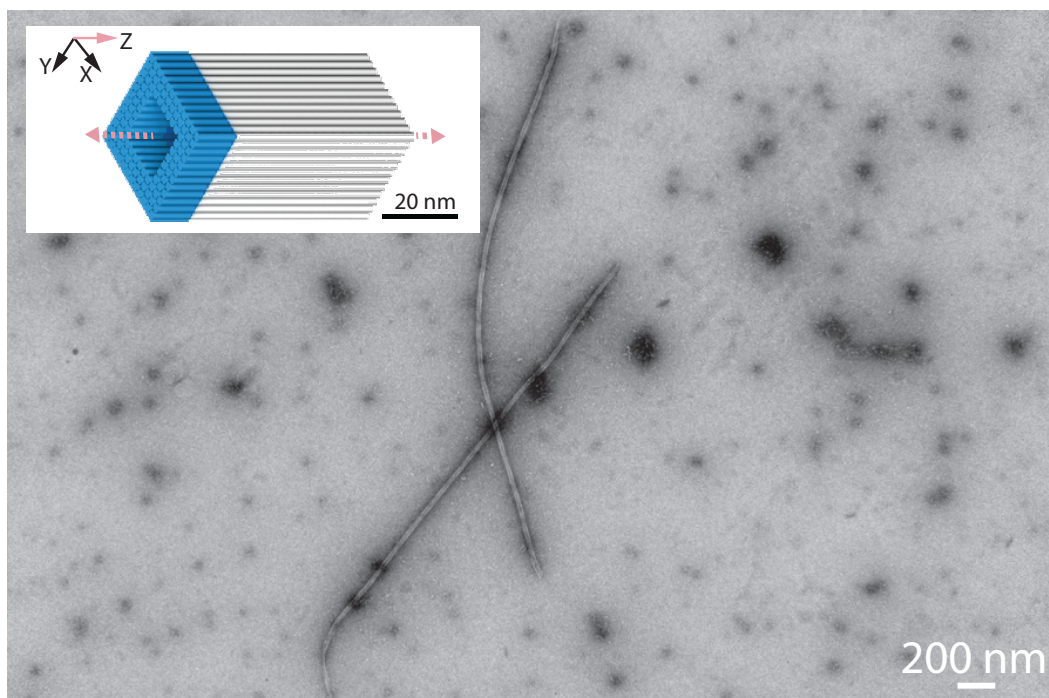
Fig. S11. TEM image of the Z-108H×32B-tunnel crystal.

S3.2 TEM images of X-crystals
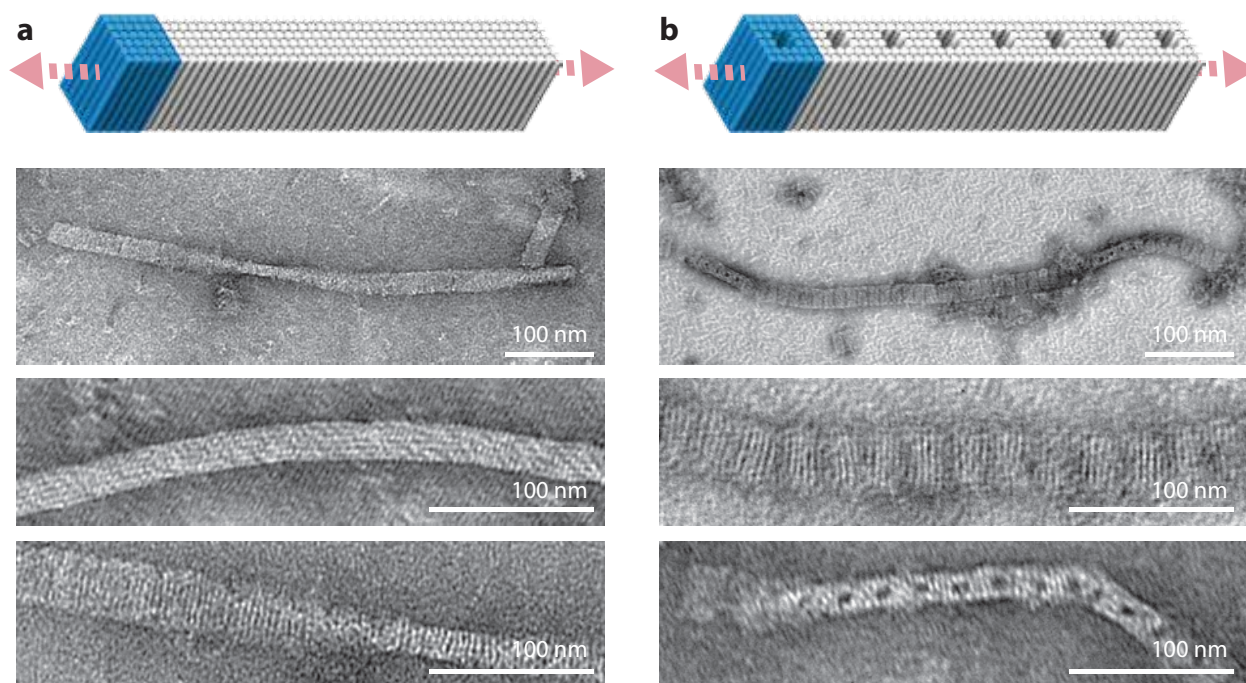
Fig. S12. Design schematics (top) and TEM images (bottom) of X-crystals. a, an X-6H×6H×64B-cuboid crystal. **b**, a 6H×6H X-crystal with 2H×2H pores. Unit cells of crystals are denoted using blue-colored boxes.

S4 Two-dimensional DNA-multilayer crystals (ZX-crystals)

Figs. S13 to S20 show TEM images of various ZX-crystals.

S4.1 TEM images of ZX-crystals
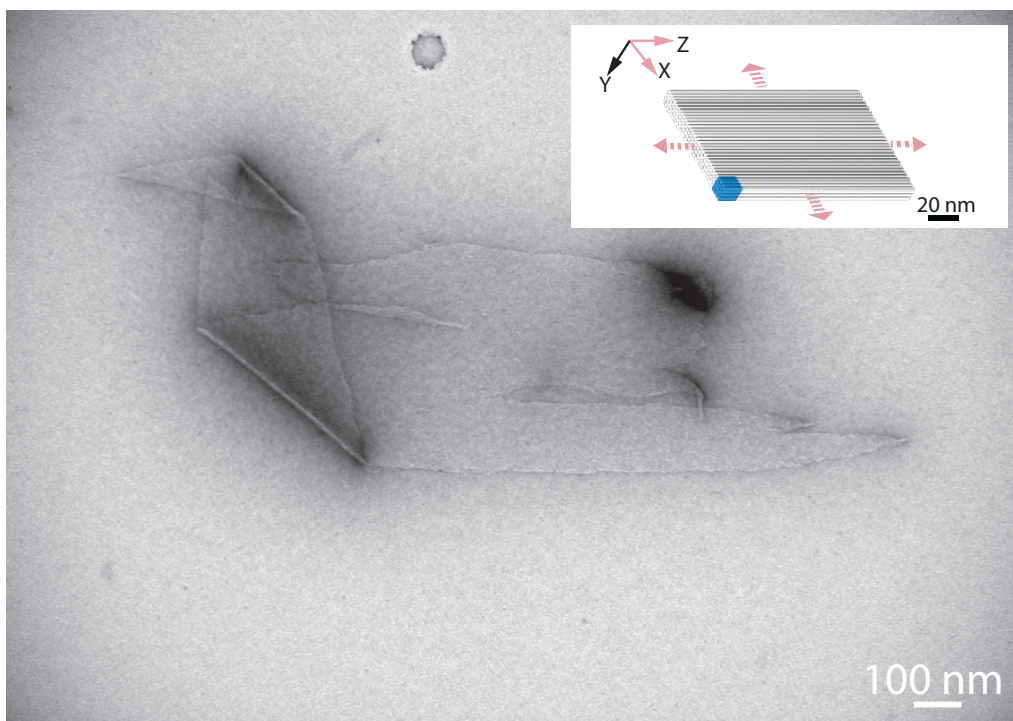
Fig. S13. TEM image of the ZX-4H×4H×32B-cuboid crystal.
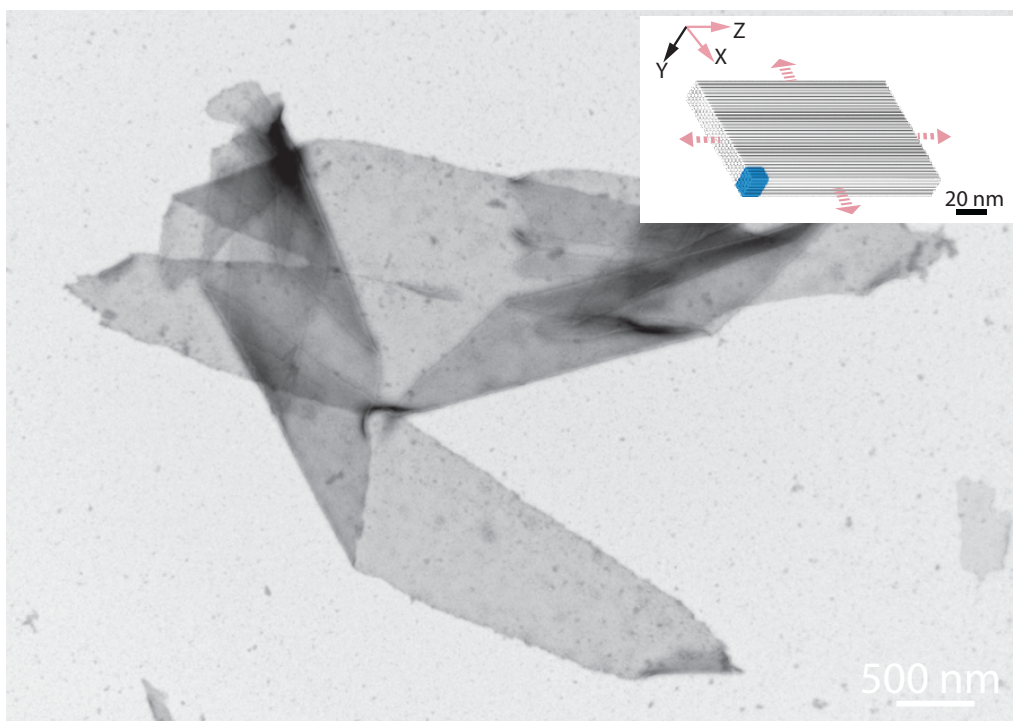
Fig. S14. TEM image of the ZX-4H×6H×32B-cuboid crystal.
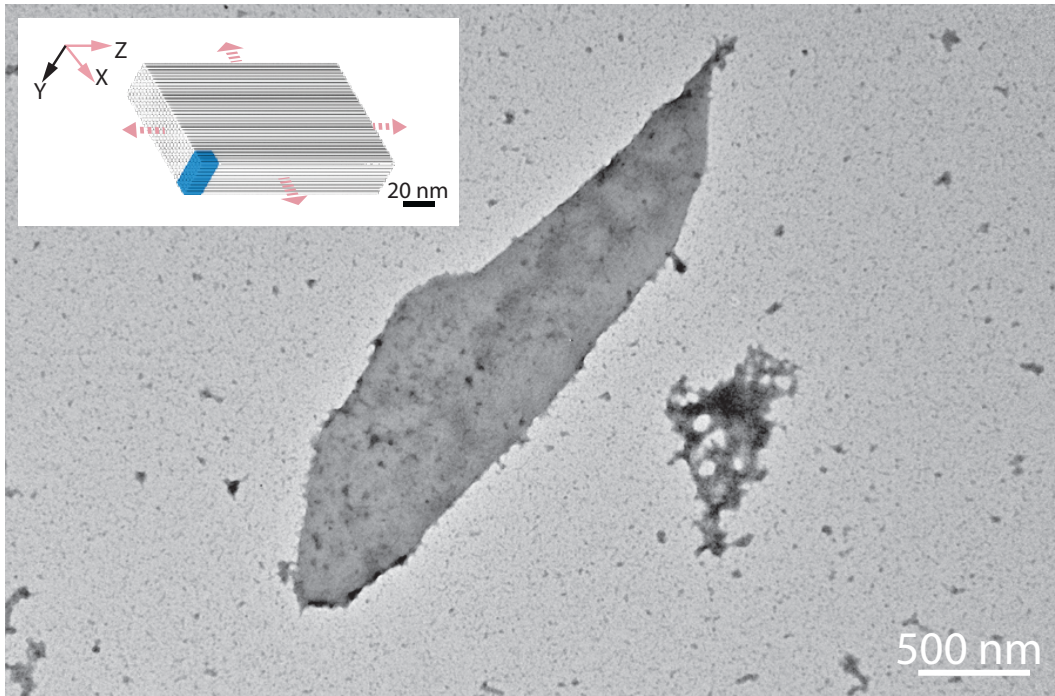
Fig. S15. TEM image of the ZX-4H×10H×32B-cuboid crystal.
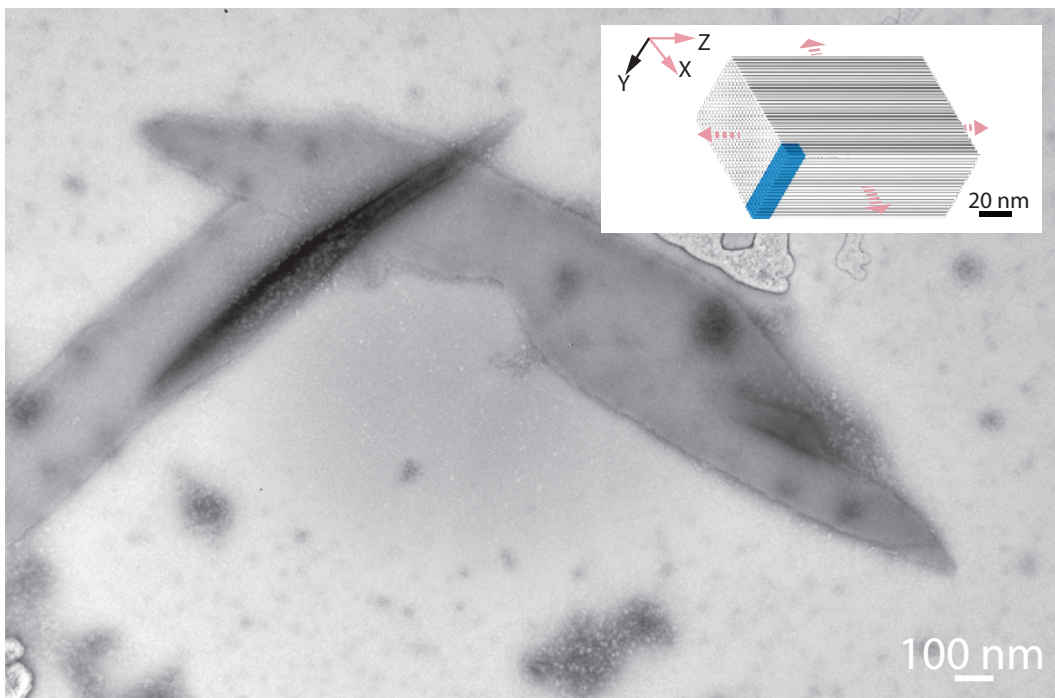
Fig. S16. TEM image of the ZX-4H×20H×32B-cuboid crystal.
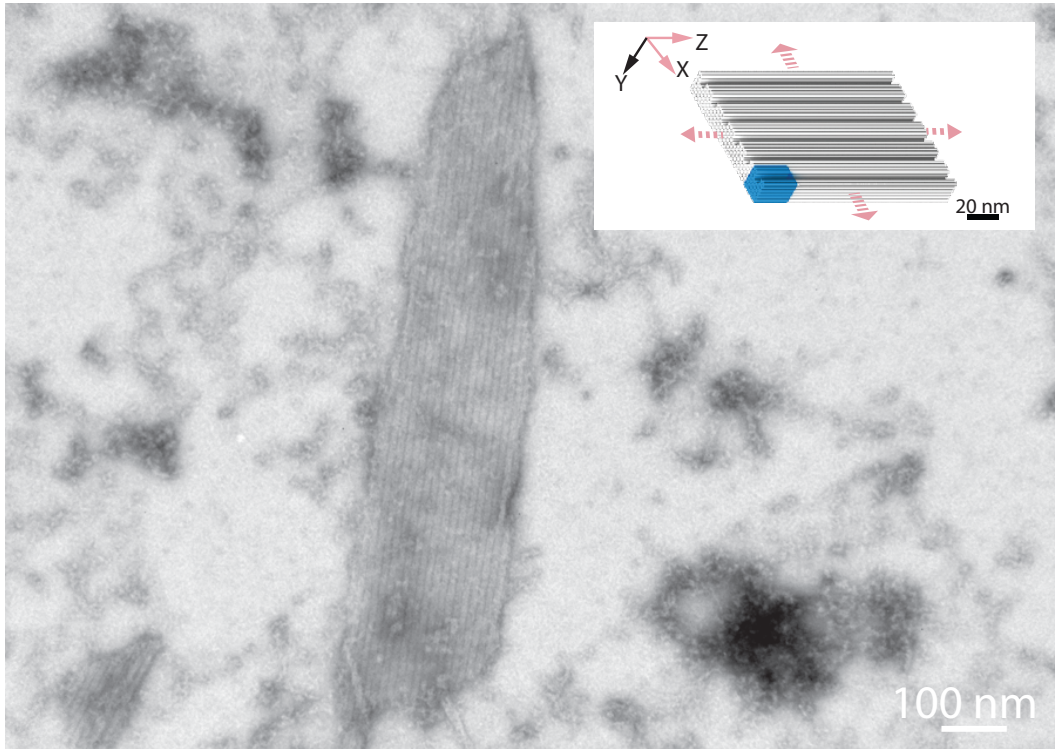
Fig. S17. TEM image of the ZX-32H×64B-channel crystal.
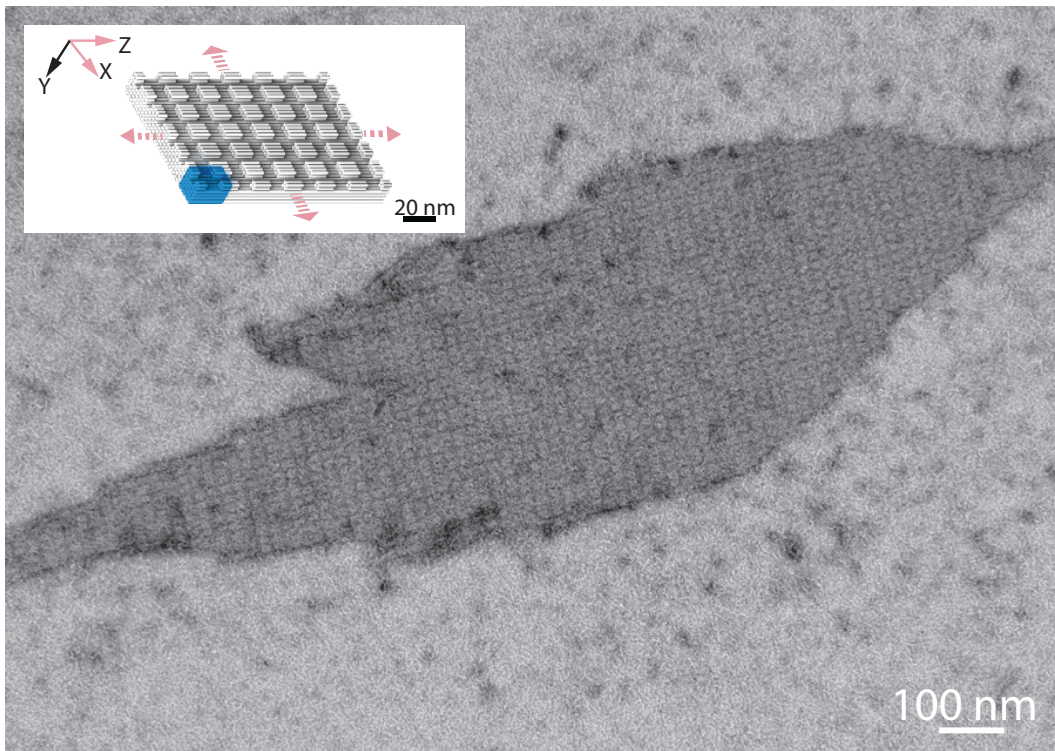
Fig. S18. TEM image of the ZX-32H×64B-cross-channel crystal.
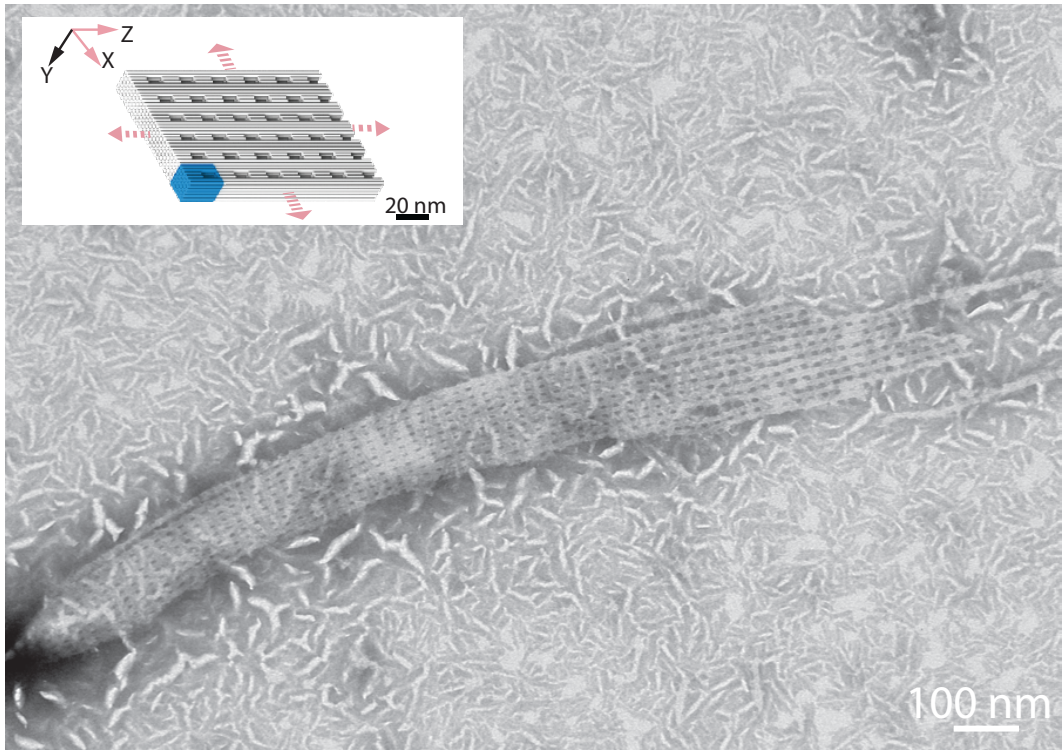
Fig. S19. TEM image of the ZX-6H×6H×64B-pore crystal.
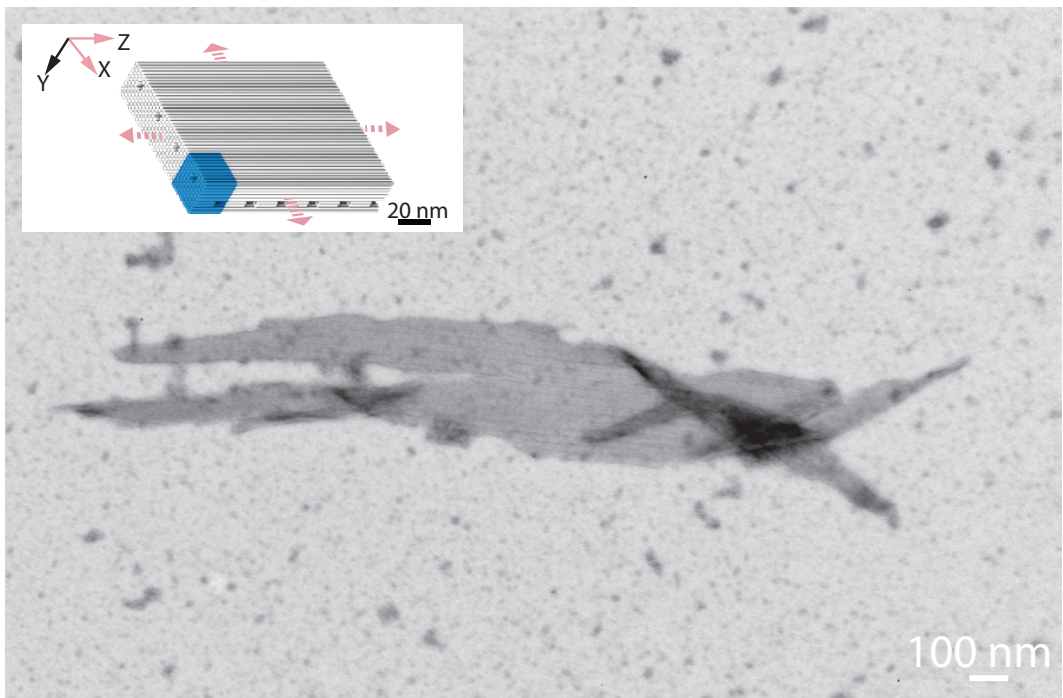
Fig. S20. TEM image of the ZX-96H×64B-cross-tunnel crystal.

S4.2   An offset ZX-crystal
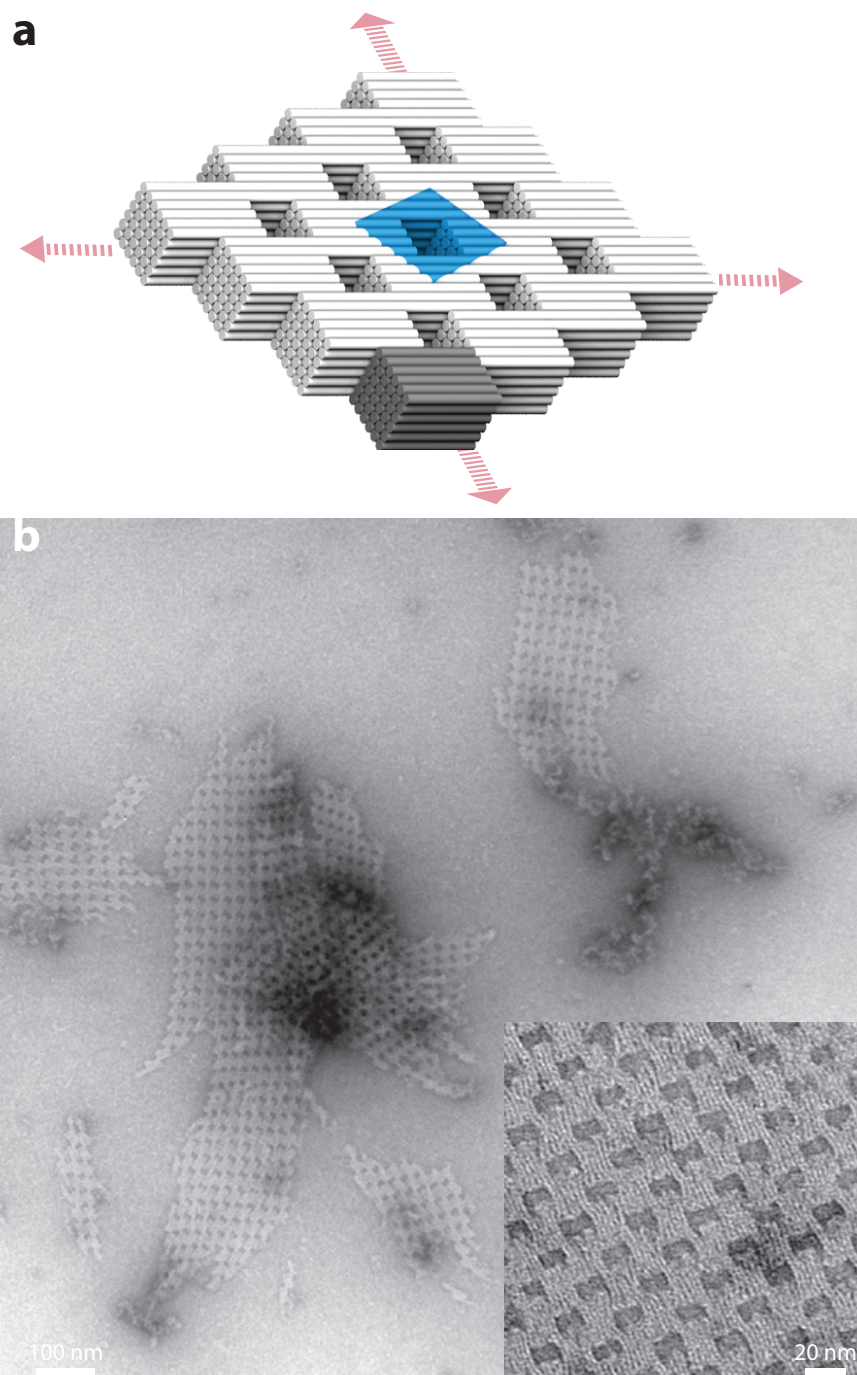
Fig. S21. Design schematic and TEM images of an offset-ZX-crystal. a, Design of the offset-ZX-6H×6H×64B-cuboid crystal. The darker part represents a 6H×6H×64B-cuboid repeating unit. A unit cell of the crystal is denoted using a blue-colored box. **b**, TEM images of the offset-ZX-6H×6H×64B-cuboid crystal.

In this offset-ZX-6H×6H×64B-cuboid crystal design, the crystal's Z-axis extension is shifted 4 duplexes along the X-axis; the crystal's X-axis extension is shifted 32 bp along the Z-axis (Fig. S21a). It is worth noting that the offset connections need to obey the following rules due to the periodicities of DNA-brick structures: shifting along the X-axis or Y-axis can occur only in two-helice intervals; shifting along the Z-axis can only occur in 32-bp intervals.

S5 Two-dimensional DNA-forest crystals (XY-crystals)

S5.1 Cryo-EM images of the XY-32H×64B-pore crystal and the XY-32H×128B-pore crystal
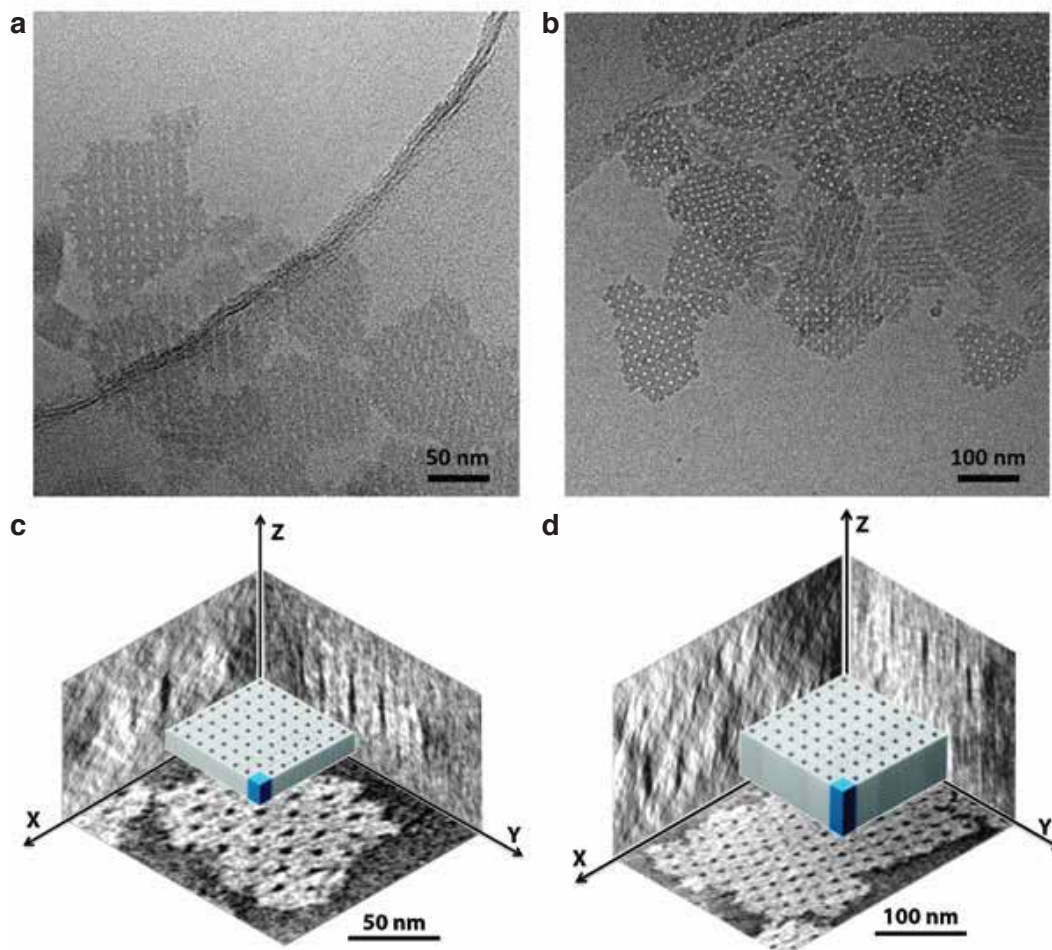
Fig. S22. Cryo-EM images of the XY-32H×64B-pore crystal and the XY-32H×128B-pore crystal a, A representative Cryo-EM image of the XY-32H×64B-pore crystal. **b**, A representative Cryo-EM image of the XY-32H×128B-pore crystal. **c**, Cryo-EM 3D reconstruction images showing the three projection views of a single XY-32H×64B-pore crystal. The 3D model is used to approximately denote the projection views of the crystal. **d**, Cryo-EM 3D reconstruction images showing the three projection views of a single XY-32H×128B-pore crystal. The 3D model is used to approximately denote the projection views of the crystal.

Cryo-EM images and 3D reconstruction date analysis of the 32H×64B-pore crystal (figs. S22a and S22c) and the 32H×128B-pore crystal samples (figs. S22b and S22d). The crystal samples were frozen in amorphous ice for imaging. 3D reconstruction was performed after data collection, and three planes (XY, XZ, YZ) were extracted from 3D reconstruction date for measurement of crystal thickness. The depths of the 32H×64B-pore crystal and the 32H×128B-pore crystal were measured to be 26×2 nm and 45±3 nm, respectively. These values were slightly larger than the theoretical values of the two crystals (21 nm and 42 nm, respectively). This is likely due to the fact that the theoretical estimations of crystal depths did not take the single-stranded poly-T (at the 5′ and 3′ ends of each duplex) into consideration.

S5.2 AFM images of the XY-32H×64B-pore crystal and the XY-32H×128B-pore crystal
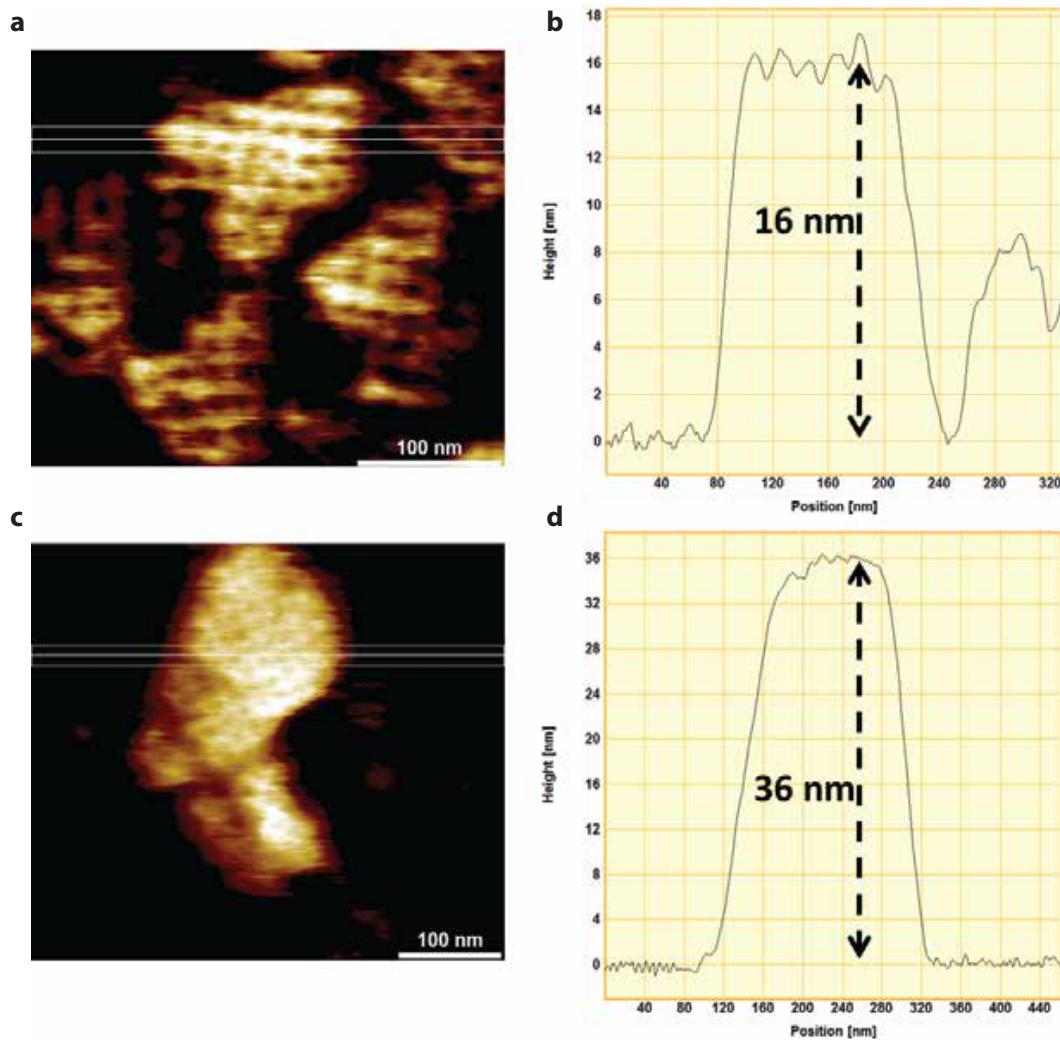
Fig. S23. AFM images of the XY-32H×64B-pore crystal and the XY-32H×128B-pore crystal a, A representative AFM image of the XY-32H×64B-pore crystal. **b**, Height-profile shows the depth of the XY-32H×64B-pore crystal. **c**, A representative AFM image of the XY-32H×128B-pore crystal. **d**, Height-profile shows the depth of the XY-32H×128B-pore crystal.

S5.3   The tube XY-crystal

S5.3.1   Proposed formation mechanism
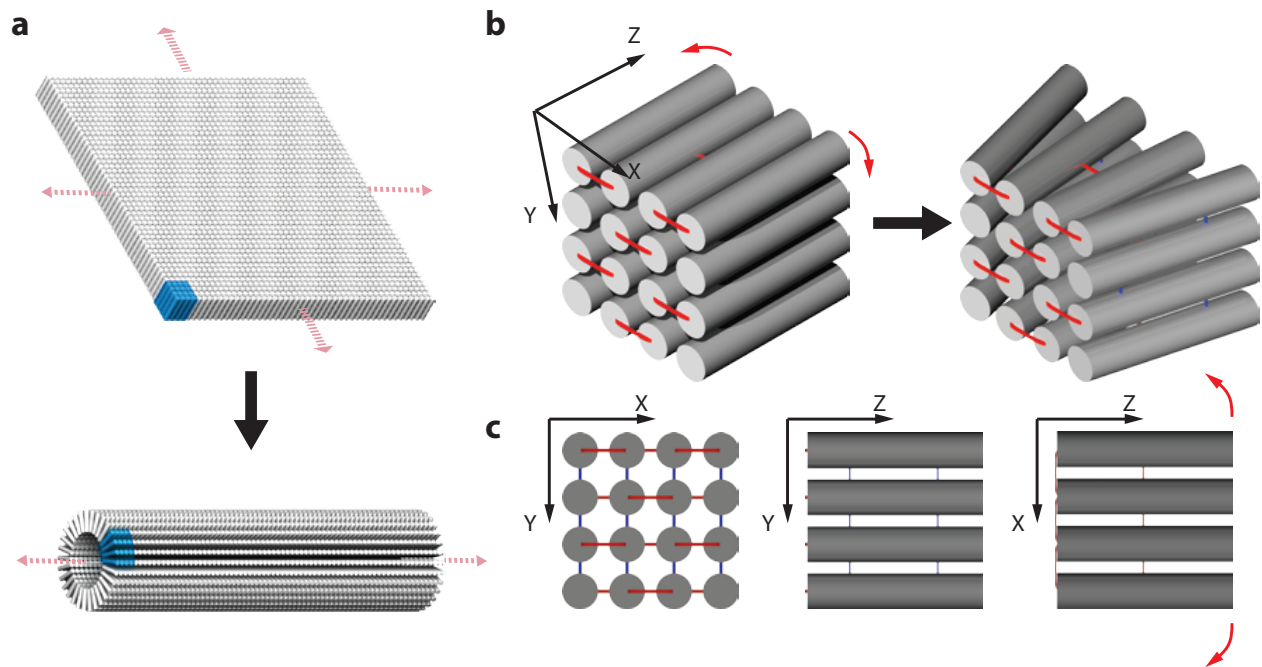
Fig. S24. Proposed formation mechanism for the XY-4H×4H×32B-tube crystal. a, Top, a two-dimensional XY-4H×4H×32B-cuboid DNA-forest crystal design. Bottom, the structure instead forms a tube. Unit cells of crystals are denoted using blue-colored boxes. **b**, A 4H×4H×32B-cuboid repeating unit expands in the X-direction while traversing along the Z-axis. **c**, Projection views of a 4H×4H×32B-cuboid repeating unit. In the ZX-plane projection view, the crossovers are asymmetrically distributed along the Z-axis: half of the crossovers are located at the middle-point of the cuboid, and the other half are located at the left end of the cuboid.

The XY-4H×4H×32B-tube crystal was designed using the same strategy as other XY-crystals. However, this thin XY-crystal (32 bp, or 10.6 nm) forms a tube structure instead of a flat 2D crystal. We hypothesize the tube formation is due to the uneven distribution of connections between helices (Fig S24). Because helices in the XY-4H×4H×32B-tube are relatively short, there is only one connection between each pair of neighboring helices. The connections are evenly distributed along the Y-axis. However, along the X-axis, half of the connections are located in the middle of the structure, and the other half are positioned at one side of the structure Figs. S24c and S64. Therefore, we hypothesize that the spacing between helices on the end with fewer connections can expand to form a crystal with a tube-like structure. These tubes are narrow and can grow to several micrometers in length (Fig. S25). The inner diameters of tubes are about 14 to 20 nm, and the outer diameters are about 34–40 nm.

S5.3.2   TEM images of the XY-4H×4H×32B-tube crystal
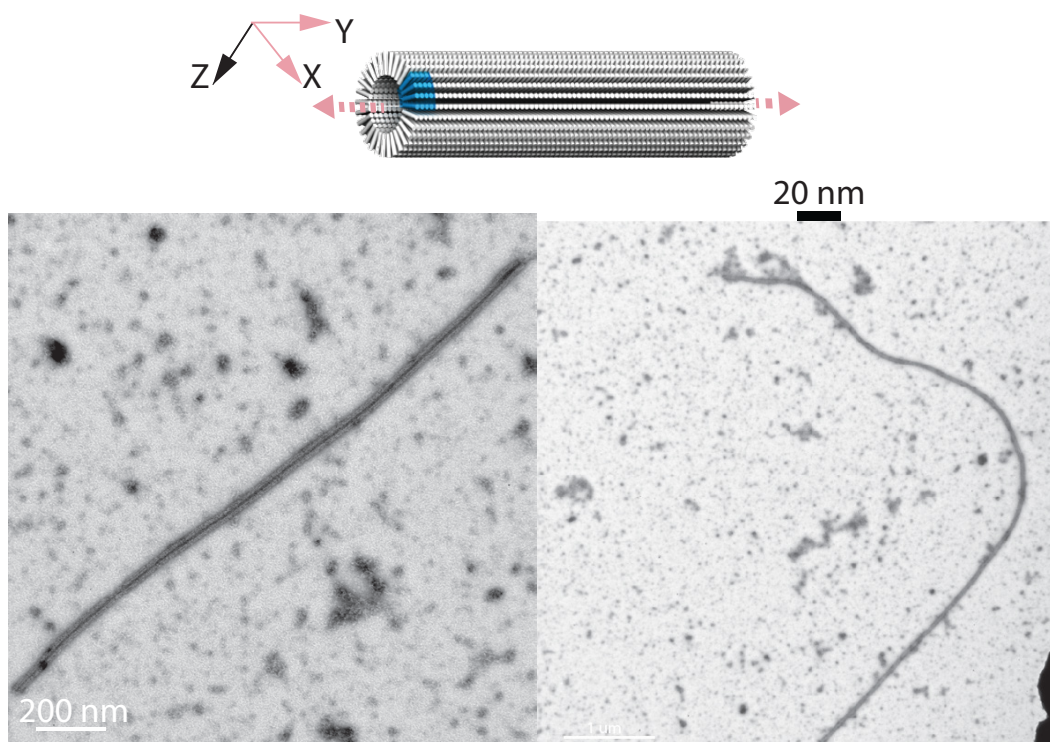
Fig. S25. TEM images of the XY-4H×4H×32B-tube crystal.

S5.3.3   TEM images of the XY-4H×4H×32B-tube crystal annealed at 60 mM of MgCl$_2$
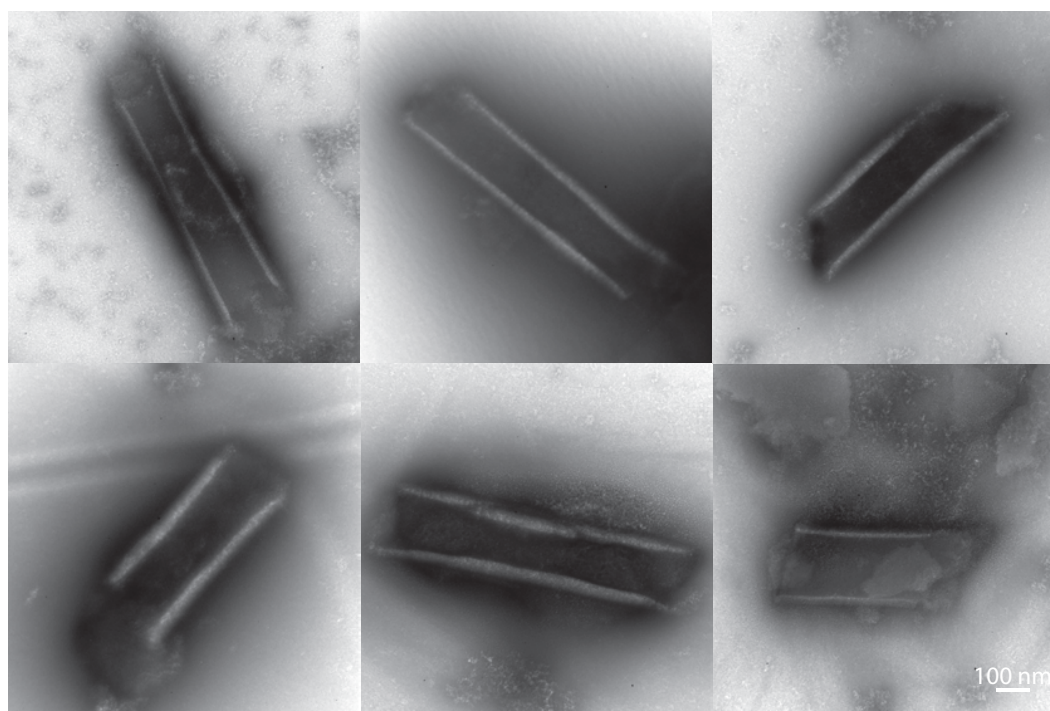
Fig. S26. TEM images of the XY-4H×4H×32B-tube crystal 60 mM of MgCl$_2$.

Annealing the XY-4H×4H×32B-tube at the presence of higher MgCl$_2$ concentration can produce tubes with larger diameters, because Mg^{2+} can reduce the repulsion between negatively-charged DNA helices. At 60 mM MgCl$_2$, we observed many tubes with diameters between 140 nm to 300 nm (Fig. S26).

S5.4 The XY-crystal with alternating DNA-bricks
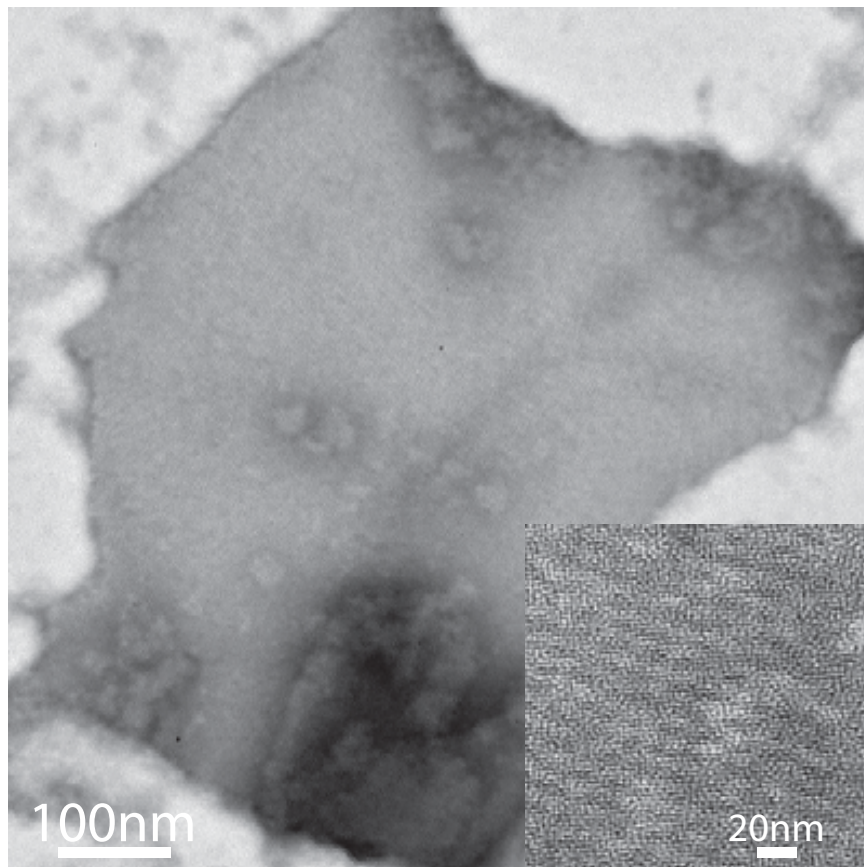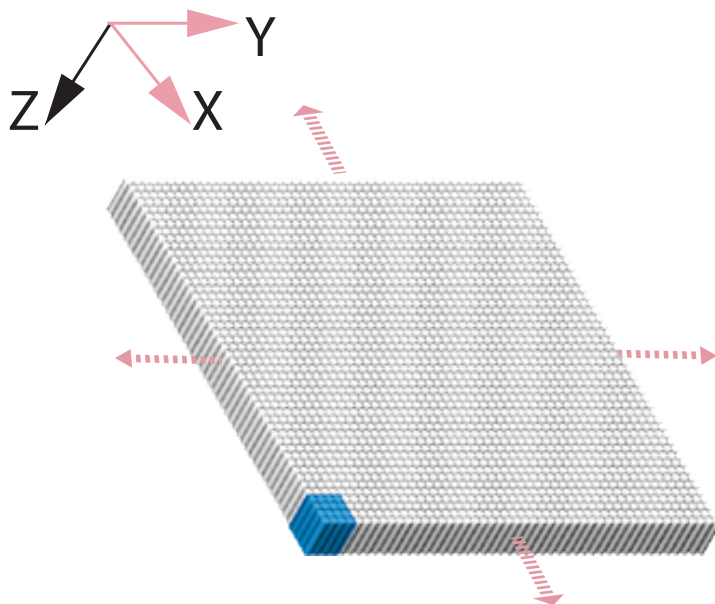
Fig. S27. TEM images of the XY-4H×4H×32B-cuboid crystal using alternating DNA-bricks.

We designed an XY-4H×4H×32B-cuboid crystal in which the DNA bricks are arranged in an alternating fashion between layers (Fig. S65). Connections between helices in this design are symmetrically distributed along both the X-axis and the Y-axis. TEM images prove that this design produces only flat crystal structures (Fig. S27).

S5.5 TEM images of the XY-crystals

Figs. S28 to S34 show TEM images of various XY-crystals.
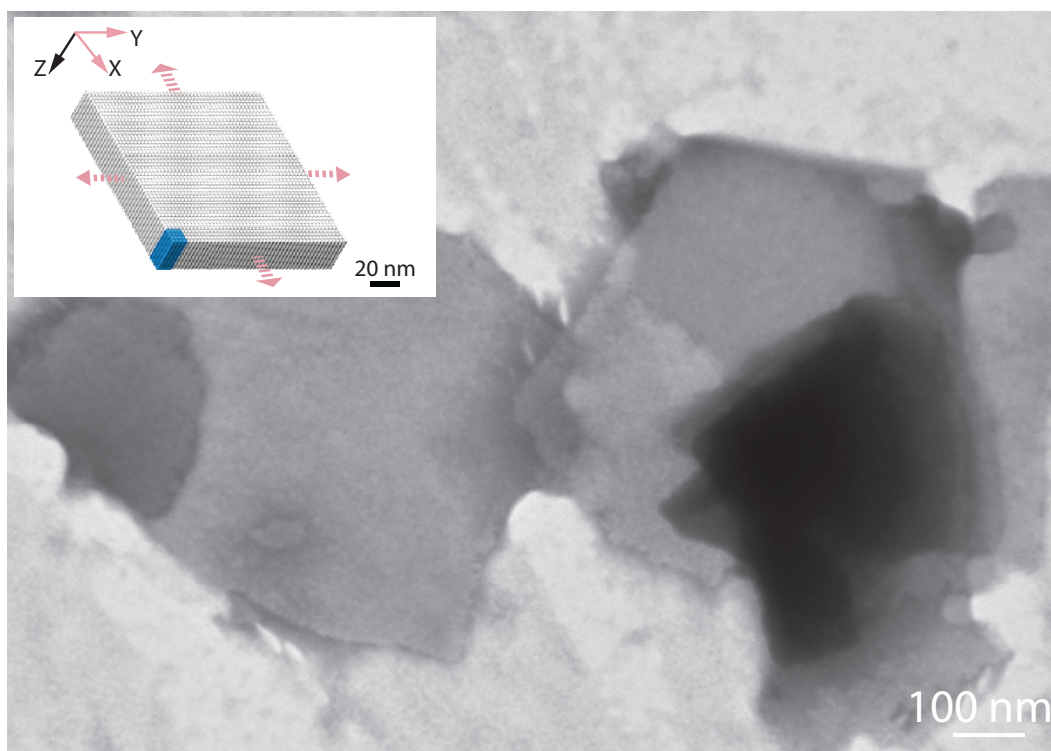
Fig. S28. TEM image of the XY-4H×4H×64B-cuboid crystal.
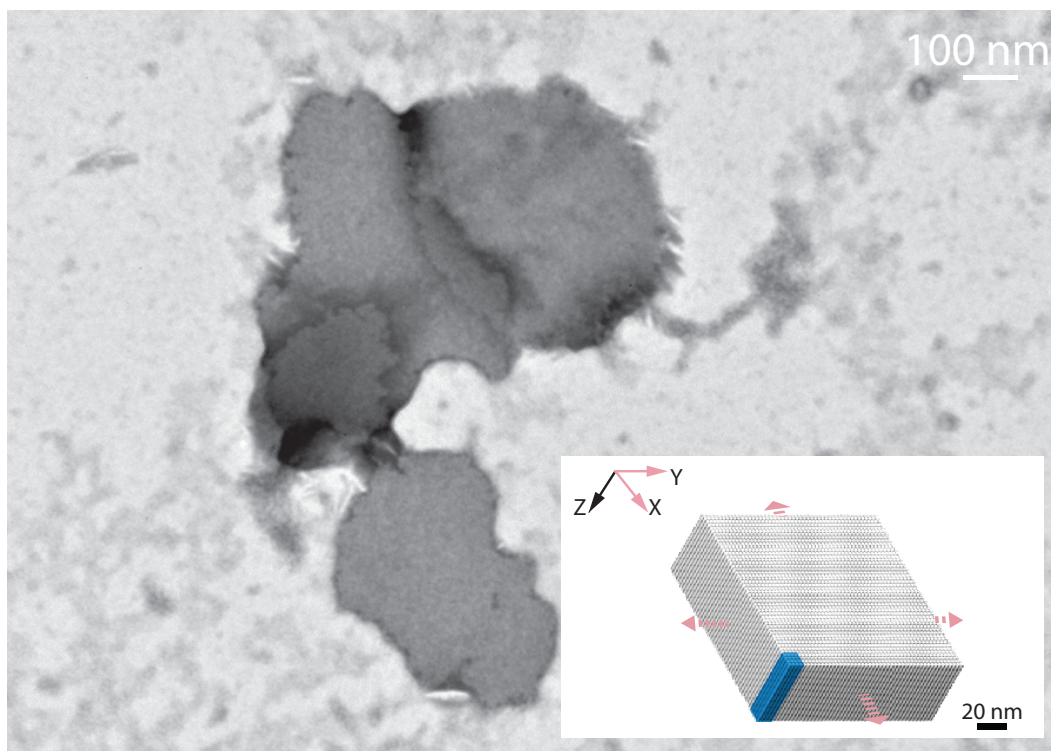
Fig. S29. TEM image of the XY-4H×4H×128B-cuboid crystal.
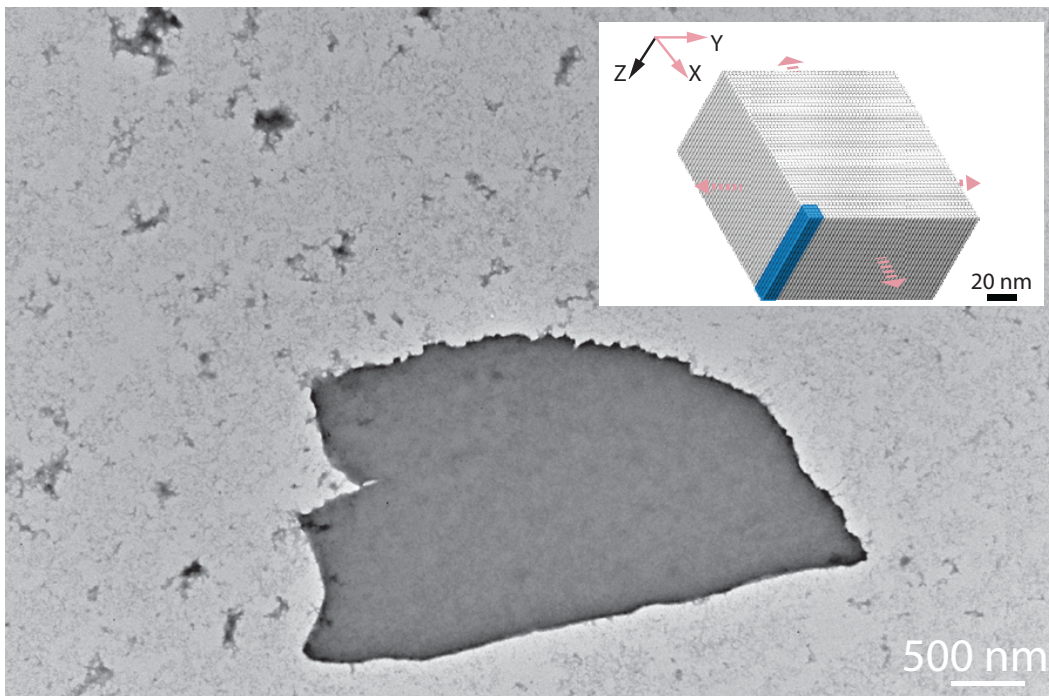
Fig. S30. TEM image of the XY-4H×4H×192B-cuboid crystal.
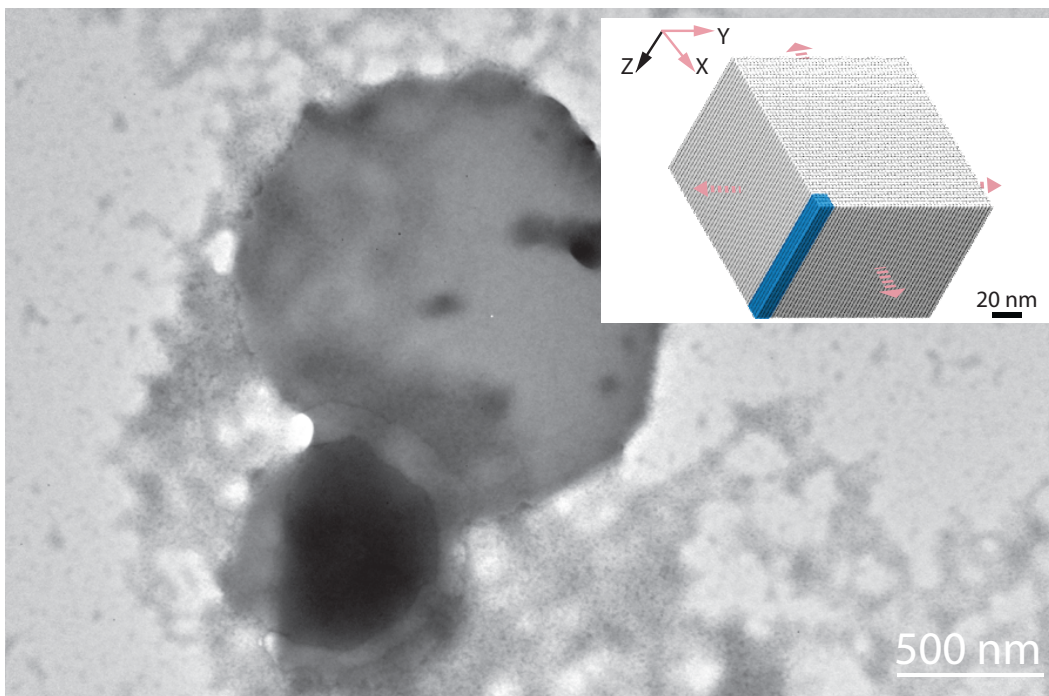
Fig. S31. TEM image of the XY-4H×4H×256B-cuboid crystal.
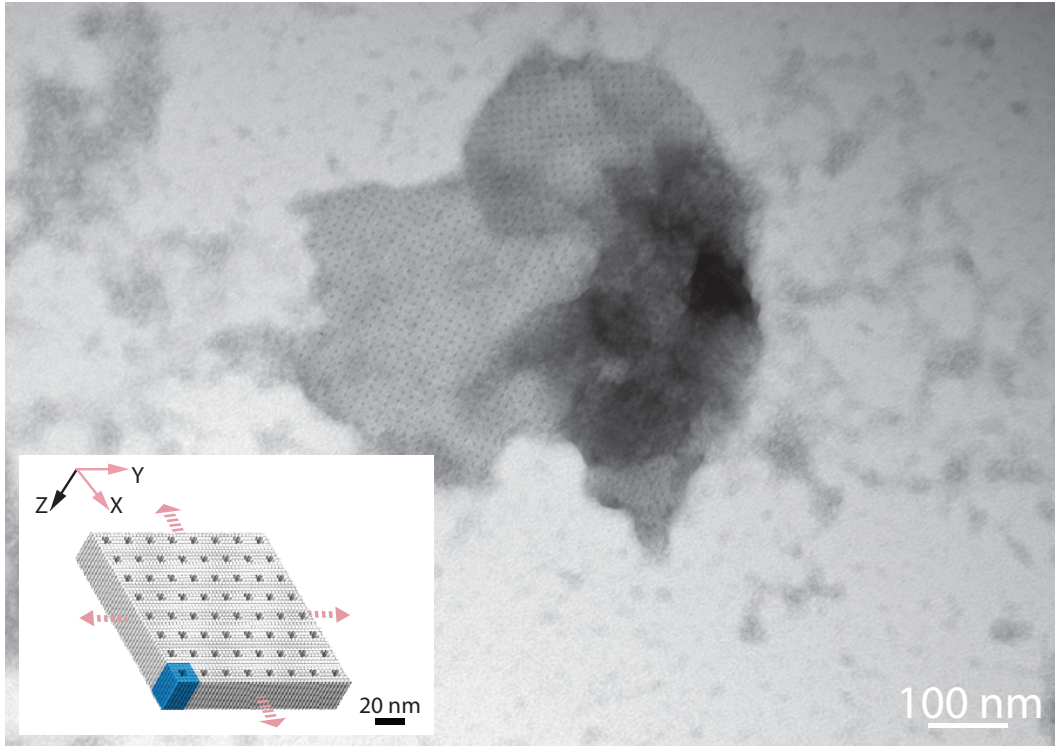
Fig. S32. TEM image of the XY-32H×64B-pore crystal.
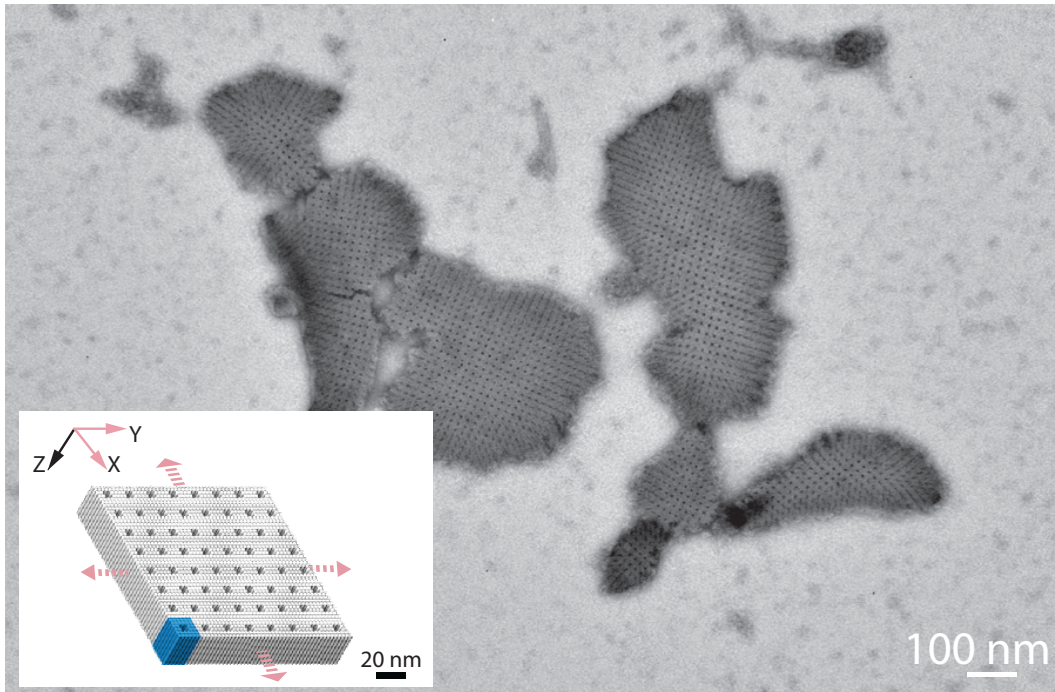
Fig. S33. TEM image of the XY-32H×128B-pore crystal.
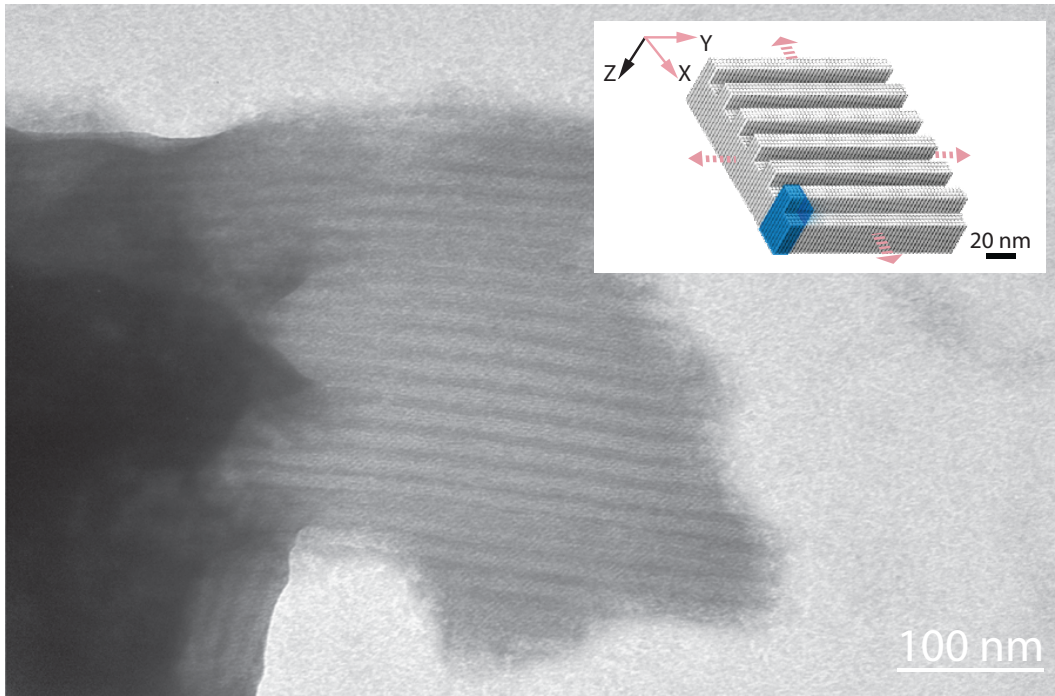
Fig. S34. TEM image of the XY-8H×4H×96B-channel.

S6 Growth mechanism study

S6.1 Boundary analysis

The boundary of a hierarchically assembled 2D DNA lattice[1] was compared with that of the XY-32H×64B-pore crystal to determine whether the edges matched the shape of the designed repeating unit. By selecting structures with a repeating unit containing surface features, we could count each edge unit and analyze whether its shape matched that of the designed repeating unit. An example of such analysis is depicted in fig. S35b. The edges of the hierarchically-assembled structures[1] showed over 90% of edge units matching the designed shape (fig. S36). In contrast, the DNA brick crystal showed only 2% of edge units matching (fig. S37). This result is consistent with our hypothesis of non-hierarchical assembly, as structures grown in a hierarchical manner would first form the monomer before assembling these units together, resulting in a uniform boundary defined by the shape of the repeating unit. In contrast, non-hierarchical assembly would have a single stage growth where individual component strands would be added to the growing crystal, resulting in an arbitrarily-shaped boundary.
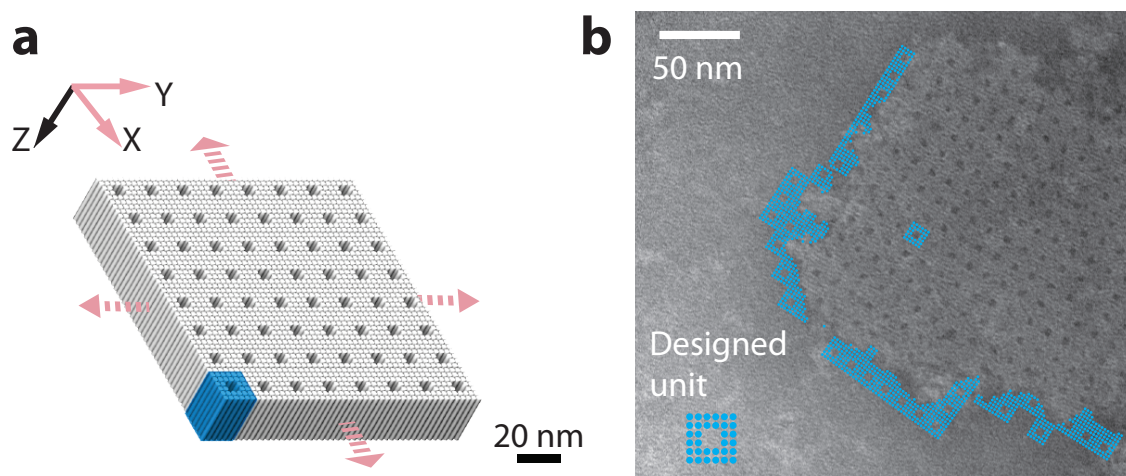
Fig. S35. **(a)** Schematic of the XY-32H × 64B-pore crystal. **(a)** TEM image of the XY-32H × 64B-pore crystal with an overlay depicting how the boundary is analyzed. The designed repeating unit is shown in the lower left and in the center of the crystal. Each blue dot represents a DNA helix. The frame outlining the structure edge shows where the boundary would be if the shape matched that of the designed repeating unit.
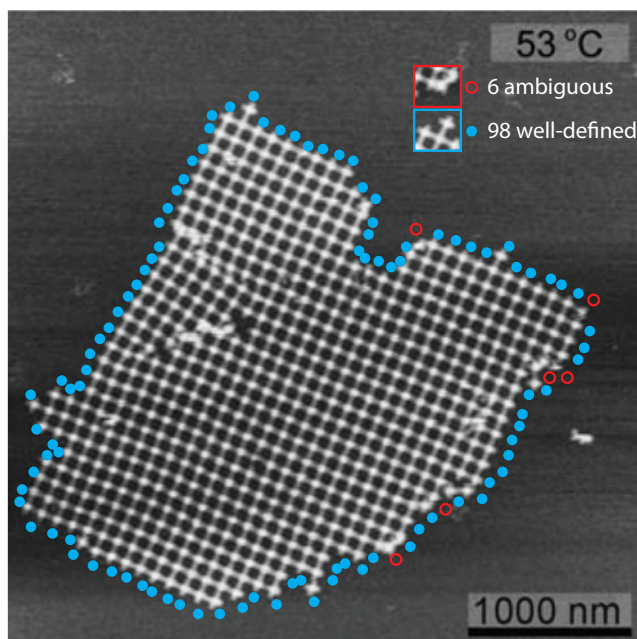
Fig. S36. A hierarchically assembled 2D lattice image obtained from Liu, et al. *Angew. Chem. Int. Ed.* 50, 264 (2011)[1] was analyzed to test whether the boundary matched the designed repeating unit. Each edge unit is marked with a blue dot if it matches the shape of the designed unit or a red circle if it does not or if the shape is ambiguous. An example of each is shown in the insets with a color-matched border. Overall, these ambiguous units comprised only 6% of all counted edge units.
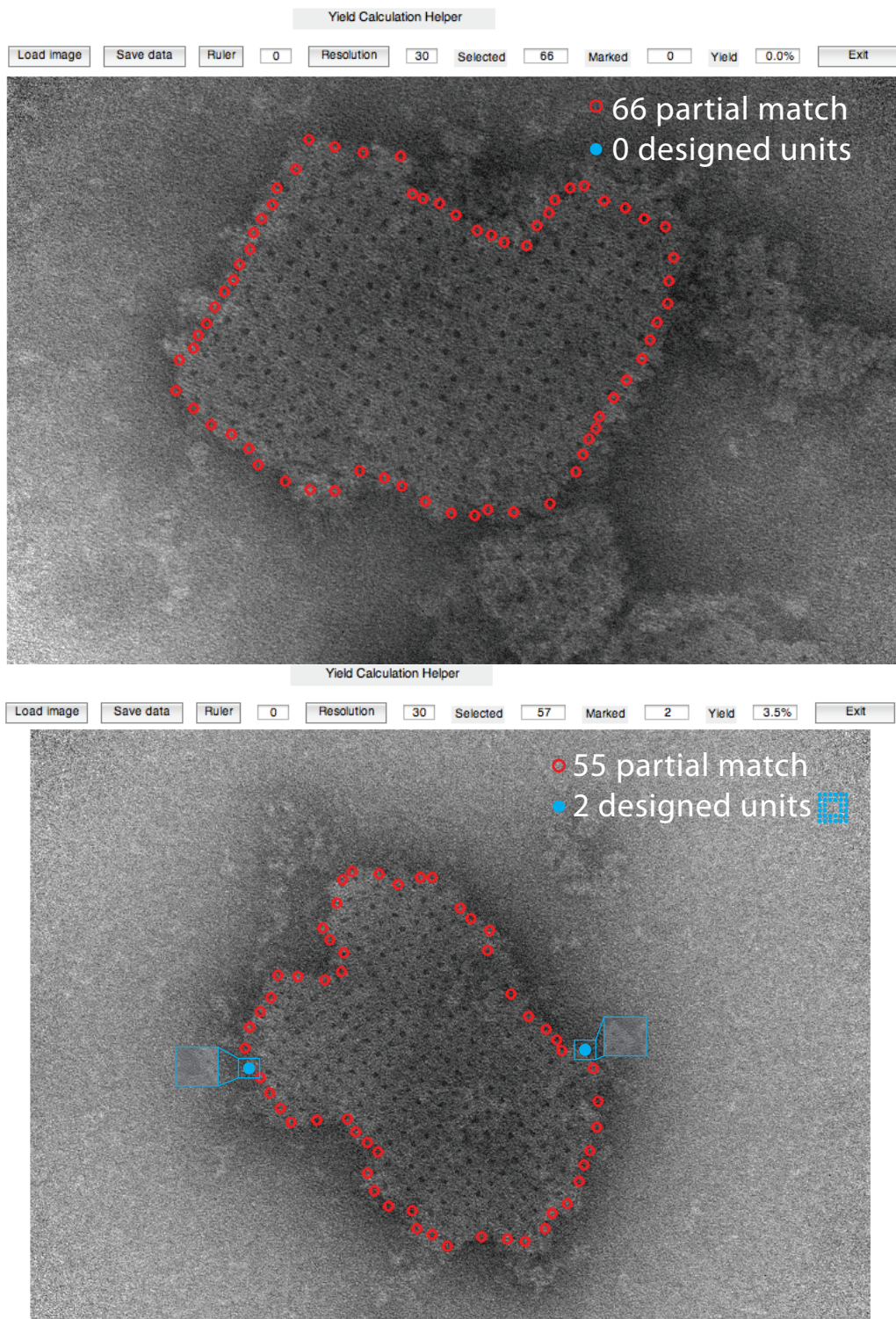
Fig. S37. A XY-32H×64B-pore crystal, where the final crystal structure clearly shows the repeating unit, was counted for the boundary analysis (**a, b**). Each edge unit is marked with a blue dot if it matches the shape of designed unit or a red circle if it does not. A total of 123 units were counted and 98% of them did not match that of the designed unit. The insets outlined in blue depict the edge where it matches that of the designed repeating unit.

S6.2 Annealing curves and the time-lapse analysis with gel electrophoresis and TEM imaging

Annealing curves and analysis was performed on two crystals as case studies: the ZX-4H×20H×32B crystal and the XY-32H×64B-pore crystal (fig. S38a and S39a). The derivative of the fluorescence with respect to temperature was obtained by subtracting two fluorescent intensities obtained one degree apart. For both these structures, a single sharp transition peak was observed for the 3-day annealing curves. For the ZX-crystal, this peak was located around 40°C (fig. S38b), while the XY-crystal had its transition around 30°C (fig. S39b). For hierarchical assembly systems (e.g. lattices formed from multi-stranded tiles), two or more characteristic transition temperatures are typically observed:[1] the lowest transition temperature corresponds to the formation/melting of lattice from the pre-formed tile monomers, and the higher ones correspond to the formation/melting of tile monomers from component strands. In contrast, our results are consistent with a non-hierarchical assembly mechanism, in which there is a single stage where individual strands are added directly into the growing structure without forming a well-defined multi-stranded monomer unit first.

Samples were collected during the annealing process and subjected to gel electrophoresis (fig. S38d and S39d). No discrete band was observed, confirming the lack of formation of a uniformly shaped monomer unit and hence the non-hierarchical growth mechanism.

To further confirm the lack of a well-defined, discrete intermediate structural unit, these time-points were also imaged under TEM. At 60, 43, and 40°C for the ZX-crystal, although some structures were observed, they were amorphous in shape and size and did not match the uniform pattern of the designed crystal (fig. S38e, insets). At 30°C, crystal structures were observed. For the XY-crystal, these small (approximately 100 nm) amorphous clusters were also observed at 60, 40, 32, and 30°C. Starting at 28°C, the designed crystal structure was observed (fig. S39e, inset). At 25°C, well-formed crystals were observed, but they were heavily stacked on top of one another. Overall, TEM imaging showed no uniformly sized and shaped discrete structures (fig. S38e), further confirming the non-hierarchical growth mechanism.

Fig. S38. Annealing and time-lapse analysis of the ZX-4H×20H×32B crystal. (a) Schematic of the ZX-4H×20H×32B crystal. **(b)** Normalized and averaged annealing curves (blue) of the ZX-4H×20H×32B crystal obtained over a 3-day anneal. Controls contain only the x-strands or the y-strands of the structure. The averaged sum of these signals was used as a baseline measurement, and final signals were normalized to fluorescence at 25°C and 80°C. The derivative of the normalized fluorescence over temperature was also calculated (green). **(c)** Raw annealing curves of ZX-4H×20H×32B obtained over a 3-day anneal and used for calculation **b**. **(d)** 2% agarose gel electrophoresis was performed on samples taken at different temperatures along the annealing curves in **b**. **(e)** TEM images of these sample annealing time points obtained in **d**. Insets depict zoomed-in images of the observed structure.

Fig. S39. Annealing and time-lapse analysis of the XY-32H×64B-pore crystal. **(a)** Schematic of the XY-32H×64B-pore crystal. **(b)** Normalized and averaged annealing curve (blue) of the XY-32H×64B-pore crystal obtained over a 3-day anneal. Controls contain only the x-strands or the y-strands of the structure. The averaged sum of these signals was used as a baseline measurement, and final signals were normalized to fluorescence at 25°C and 80°C. The derivative of the normalized fluorescence over temperature was also calculated (green). **(c)** Raw annealing curves of the XY-32H×64B-pore crystal obtained over a 3-day anneal and used for calculating **b**. **(d)** 2% agarose gel electrophoresis was performed on samples taken at different temperatures along the annealing curves in **b**. **(e)** TEM images of these sample annealing time points obtained in **d**. Insets depict zoomed-in images of the observed structure.

S6.3 Isothermal assembly of brick crystals

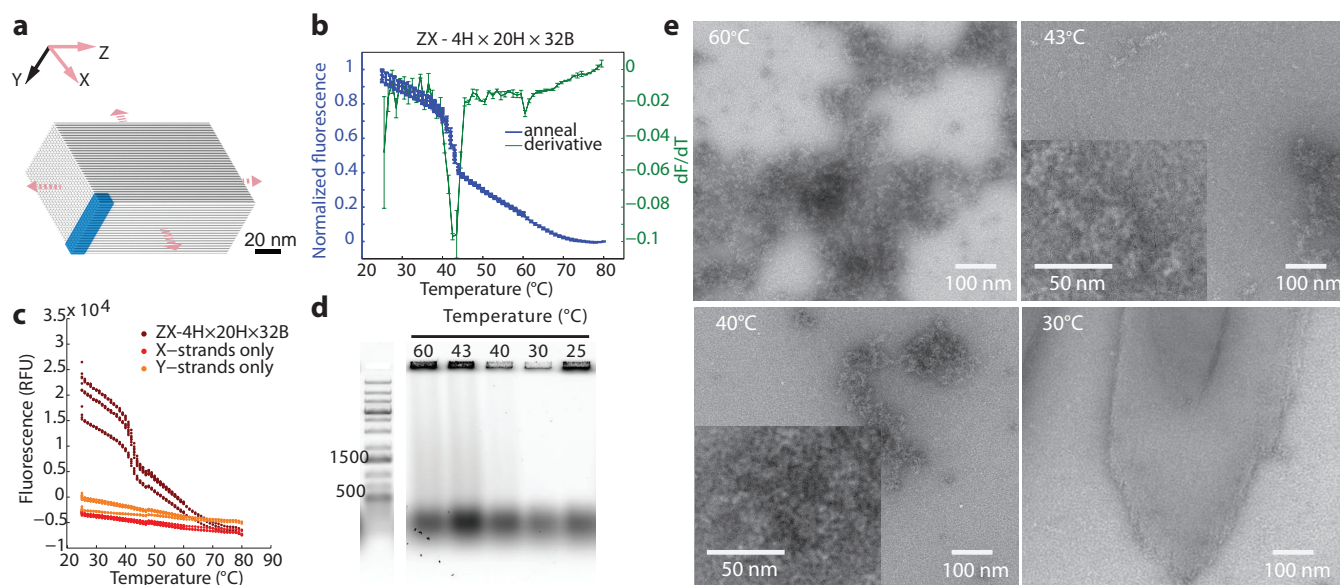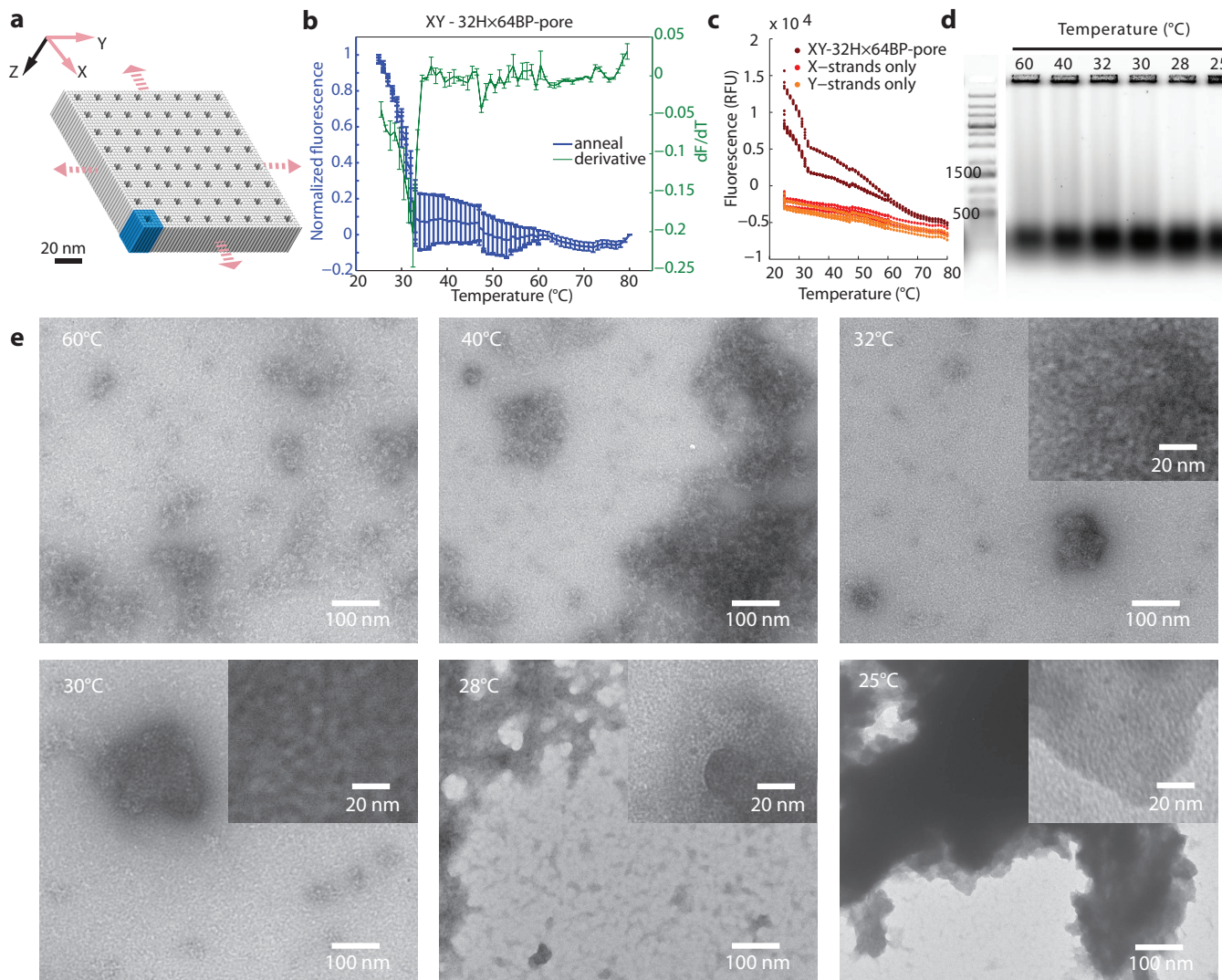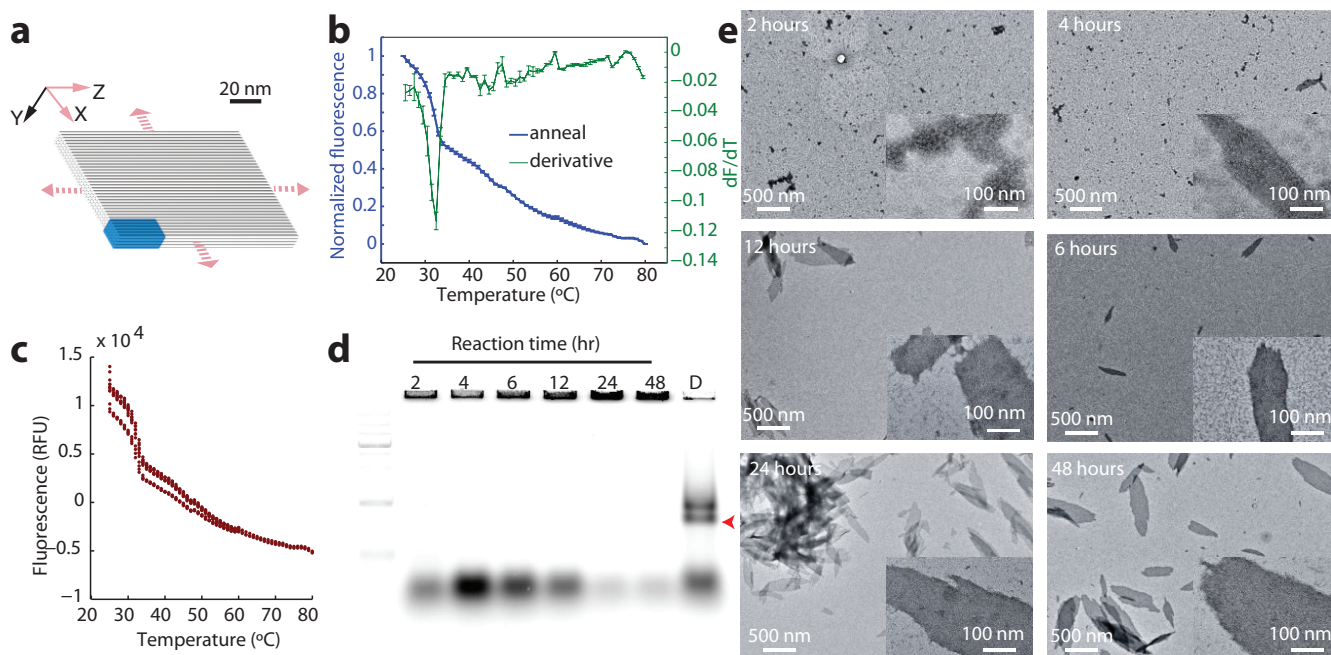**Fig. S40. Isothermal assembly and time-lapse analysis of the ZX-6H×4H×96B crystal.** (a) Schematic of the ZX-6H×4H×96B crystal. (b) Normalized and averaged annealing curve (blue) of the ZX-6H×4H×96B crystal obtained over a 3-day anneal. These signals were normalized to fluorescence at 25°C and 80°C and averaged. (c) Raw annealing curves of ZX-6H×4H×96B crystal obtained over a 3-day anneal and used for calculating **b**. 500 nM of each strand was folded in the presence of 0.3× SYBR Green I. (d) 1.5% agarose gel electrophoresis was performed on samples taken at different times after the reaction was initiated for a 33°C isothermal annealing protocol. Red arrow denotes the location of the band for a discrete 6H×4H×96B cuboid. (e) TEM images of the time-lapse samples obtained in **d**. Insets depict zoomed-in images of the observed structure.

Annealing curves for the ZX-6H×4H×96B crystal was obtained by assembling the crystal in the presence of SYBR Green I (Fig. 5b, S40b,c). Fig. S40c depicts the raw fluorescent data for the ZX-6H×4H×96B crystal for the curves in Figs. 5b and S40b. Signal was directly averaged to obtain the reported fluorescent trace. The derivative of the fluorescence with respect to temperature was obtained by subtracting two fluorescent intensities obtained one degree apart. These curves allowed us to find the peak transition temperature for isothermal folding.

The structure were then isothermally annealed at the obtained peak temperature of 33°C. Time-points were sampled during this annealing process and analyzed by gel electrophoresis (fig. S40d), which showed no discrete monomer band. As a control, a 6H×4H×96B cuboid was also folded and analyzed on the gel (fig. S40d, lane D). The time points obtained for the gel analysis were also used for TEM imaging.

S7 Yield and defects analysis

S7.1 Overview

We used crystal deposition density and strand depletion ratio to study the approximate yield of the brick crystals, and performed defect analysis to determine the quality of the structures formed.

Deposition density. We diluted the isothermally folded ZX-6H×4H×96B sample four times and counted the number of structures within four 40μm $\times$ 32μm regions on a TEM grid. A high density of more than 0.23 structures per μm^2 was observed, suggesting that crystallization of these structures is relatively easy (fig.S41).

Strand depletion ratio. Another metric to estimate the formation yield is the brick strand depletion ratio. We labeled strands with fluorescein and rhodamine on two neighboring helices in a ZX-6H×6H×64B crystal for Förster Resonance Energy Transfer (FRET) experiments (fig. S42). A strand depletion ratio of 80% was found by taking the ratio of the fluorescent signal drop (fig. S42f) with an approximated FRET efficiency (fig. S42c) obtained by analyzing the FRET behavior in a discrete 6H×6H×64B structure. It is to be noted that the strand depletion ratio likely represents an overestimate for crystal formation yield as this ratio does not account for potential quenching between the dye pairs on different repeating units or any quenching observed from random strand aggregation instead of the target structure formation.

Defect analysis. To roughly assess crystal formation quality, we counted the number of defects in the center of the XY-32H×64B-pore crystal, where a pore was considered defective if it is missing or enlarged over 10% of the designed dimensions. A 9.2% defect rate was observed for the features (fig. S43). Note that this ratio is likely an overestimate of the defects as debris adhering to the crystal surface could cause false positives in the analysis (fig. S43d).
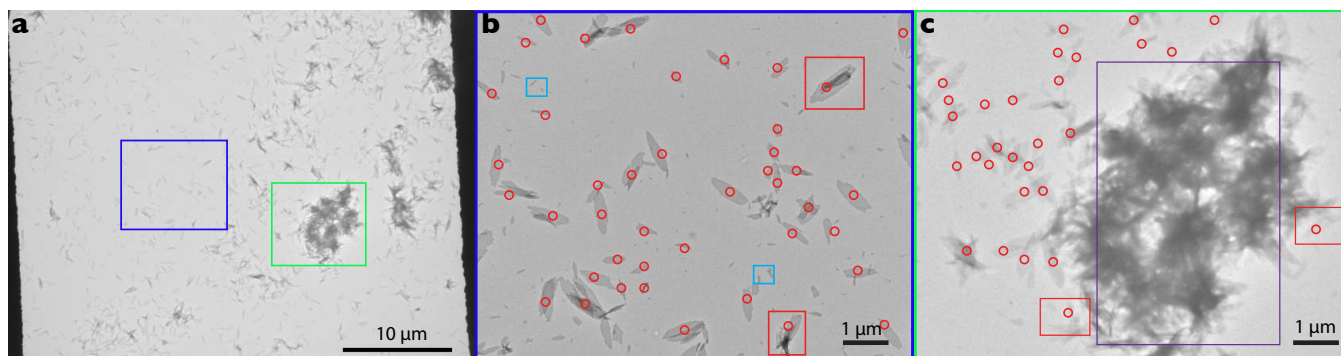
S7.2 Deposition density analysis

Fig. S41. Deposition density analysis of the ZX-6H×4H×96B crystal. **(a)** Large-field-of-view TEM images of the ZX-6H×4H×96B crystal assembled under isothermal conditions at 33°C for 48 hours. The sample was diluted four times before deposition on TEM grids. **(b)** Zoomed-in view of the inset outlined in blue in **a**. Each red circle indicates one counted crystal. The crystal structures that appeared smaller than 200 nm × 100 nm, such as those outlined in light blue, were not counted. Aggregation prevents accurate counting of the crystals on the surface. A few structures were stacked (e.g. those outlined in red), and each stack of crystals was counted only as one crystal. **(c)** Zoomed-in view of the inset outlined in green in **a** showing how structures were counted when there was heavy aggregation. The main aggregate, outlined in purple, was excluded from counting. Some smaller clear structures on the edges were counted (red).

The ZX-6H×4H×96B crystal was formed isothermally for 2 days (Fig. 5). The sample was then diluted four times and deposited on a TEM grid to determine structure deposition density. Four randomly selected 40 μm x 32 μm regions were counted for the number of structures present (fig. S41a). We found more than 300 individual crystals larger than 200 nm × 100 nm in each region (fig. S41b). This results in a deposition density higher than 0.23 crystal per μm^2. Because the structures aggregate together, precise counting is challenging and the reported density is an under-estimate of the total structures present within the selected regions (fig. S41c). Although deposition density does not provide a direct measure for the yield, the large number of structures counted suggests that crystallization of these DNA structures occurs relatively easily.
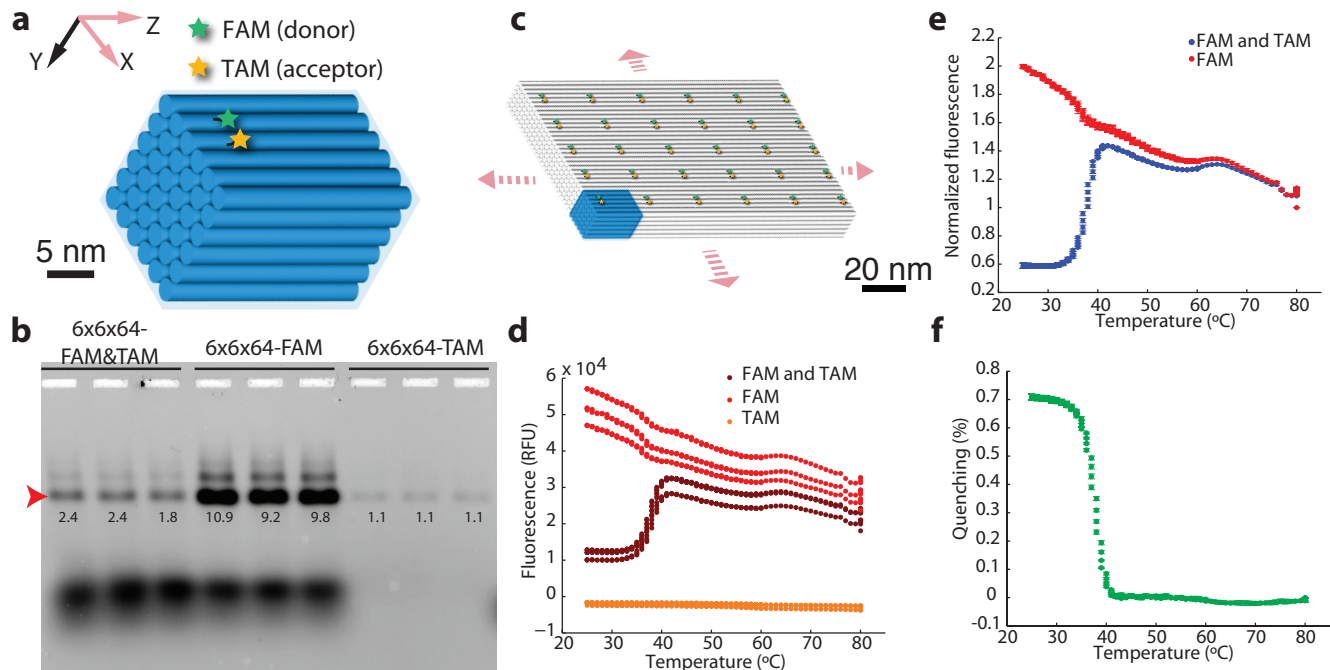
S7.3 Strand depletion analysis

Fig. S42. Strand depletion analysis of the ZX-6H×6H×64B cuboid crystal. (a) Schematic of the 6H×6H×64B cuboid with the locations of the donor and acceptor dye labels denoted by the stars. The green star represents the donor FAM dye and the yellow star represents the acceptor TAM dye. **(b)** 2% gel electrophoresis of the 6H×6H×64B cuboid assembled for 3 days at 100 nM per strand with the presence of both donor and acceptor labels, donor only, or acceptor only. The gel was not stained and scanned using the donor channel only. The red arrow points to the location of the folded structure, and the values below denote the measured intensity of that band. **(c)** Schematic of the ZX-6H×6H×64B cuboid crystal with the locations of the donor and acceptor dyes labeled. Because the ZX-crystal uses a repeating unit that is the same size as the discrete cuboid structure, the relative locations of the dye labels are the same on each monomer. **(d)** Raw donor fluorescence signals of the ZX-crystal assembled at 100 nM per strand for 3 days in the presence of donor and acceptor labels, donor only, or acceptor only. **(e)** Normalized fluorescent signal in the donor channel of the ZX-crystal. The acceptor signal is subtracted for the traces with both labels. All traces are normalized to the signal at 80°C. **(f)** The percentage of quenching observed from the dual-labeled structure relative to that with the donor only labeled structure from **e**. N = 3. Error bars represent standard deviation from the mean.

To determine the strand depletion ratio, we used a discrete 6H×6H×64B cuboid (see fig. S75 for strand diagram) and the ZX-6H×6H×64B cuboid crystal with both FAM and TAM labels or just the FAM or TAM label (fig. S42a,c). In our case, the FAM label is the donor dye (D), while the TAM label is the acceptor (A).

FRET efficiency measurement using the discrete cuboid. We first measured the FRET efficiency using the discrete cuboid (fig. S42a). 2% gel electrophoresis was performed on the discrete 6H×6H×64B cuboid and scanned in the donor channel (fig. S42b). The intensity of the band was measured for each of the samples. The FRET quenching efficiency of this structure was estimated by applying these intensities to the equation: $E = 1 - \frac{I_{DA} - I_A}{I_D}$, where I represents the intensity at the donor wavelength. Note that the FRET efficiency calculated here assumes that in the dual-labeled sample every structure with a donor dye also contains the acceptor dye. Additionally, it is assumed that the background acceptor leakage observed in the dual-labelled structure has the same intensity value as the structure with the acceptor only. The FRET efficiency is measured to be 89%.

Bulk fluorescence quenching of the brick crystal. We next measured fluorescence quenching on the ZX-6H×6H×64B cuboid crystal (fig. S42d). The raw fluorescence signals were normalized as follows: $\frac{F_D}{F_{D,80°C}}$ for the sample containing donor dye only and $\frac{F_{DA} - F_A}{F_{DA,80°C} - F_{A,80C}}$ for the sample with both labels (fig. S42e). Here, F_A represents the raw fluorescent signal from the sample containing TAM and the signal was normalized to that at 80°C. These normalized signals were then used to calculate the percentage of quenching: $Q = 1 - \frac{F_{DA}}{F_D}$ (fig. S42f). The final sample quenching was found to be 71%.

Strand depletion ratio. By assuming that the bulk fluorescence quenching observed on the crystals is due only to FRET quenching, we can approximate the strand deletion ratio by $Y = \frac{Q}{E}$, where Q is the bulk quenching and E is the FRET efficiency. Using this method, the estimated strand depletion ratio for the brick crystal is 80%. Note that this measurement likely represents an overestimate for the crystal formation yield because it does not account for potential quenching between the dye pairs on different repeating units or any quenching observed from random strand aggregation instead of the target structure formation.
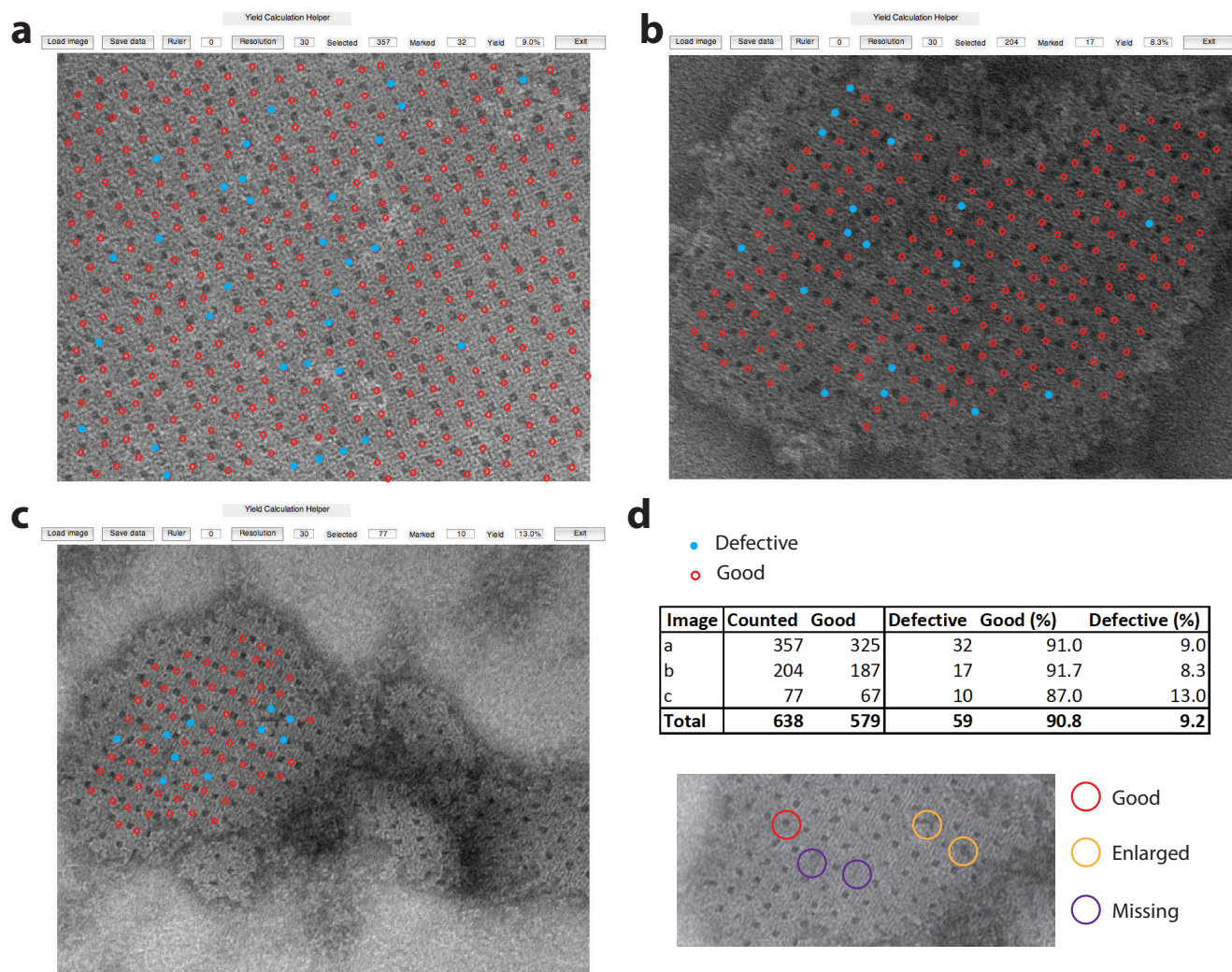
S7.4 Defect analysis

Fig. S43. Defect analysis of the XY-32H×64B-pore crystal. Pores in the XY-32H×64B-pore crystal were counted and categorized to be either "present/good" or "missing/defective" depending on whether the TEM images showed a pore of approximately the correct dimensions and in the correct location (**a-c**). Present pores are marked with a red circle, while the defective ones are indicated with a blue-filled red circle. (**d**) Analysis statistics and methodology. A total of 638 pores were counted, and 91% of them are "good". The image shows how the pores were categorized as either good (red) or defective (enlarged pores [yellow] or missing pores [purple]).

To roughly determine the quality of the crystals, we counted the number of defective pores in a XY-32H×64B-pore crystal. A pore was considered defective if it was either missing from its expected location or was enlarged by more than 2 nm (see examples in fig. S43d). A 9% defect rate of the pores in the XY-32H×64B-pore crystal was observed. The enlarged pores could be caused by missing strands in the structure. Additionally, the crystal surface is often observed to be rather rough, possibly as a result of stacking between structures or non-specific sticking of other strands. From the images, it appeared that such non-specific interactions caused certain materials/structures to adhere on the surface of the crystal and thus fill or block the designed pores. As a result, our estimated defect rate is likely an overestimate due to debris adhering to the crystal surface causing false positives in the analysis.

S8 Patterning of gold nanoparticles

S8.1 Overview

Gold nanoparticles have been arranged into discrete patterns[2–4] and single-layer periodic patterns[5] using DNA structures as templates. However, it remains challenging to form close-packed periodic patterns, especially multi-layer patterns, of gold nanoparticles. In order to demonstrate the capability of the DNA-brick crystals in arranging materials, we designed and constructed two close-packed gold-nanoparticle structures: (1) parallel lines of gold particles arranged on a ZX-4H×6H×96-channel crystal (Figs. 6a and 6b), and (2) parallel gold-nanoparticle monolayers arranged on an XY-4H×4H×64-cuboid (Figs. 6c to 6e).

The design and TEM images of the ZX-4H×6H×96-channel crystal is shown in figs. S44 and S76. A channel is two-helix (5 nanometers) in depth, and 32-bp (10.6 nanometers) in width. Neighboring parallel channels are separated by 64-bp (21.2 nm) distance along the Z-axis. Gold nanoparticles functionalized with poly-A (ten consecutive adenine bases) DNA strands were arranged on the DNA crystals. Within the channels, every helix-end displays a poly-T (ten consecutive thymidine bases) single-stranded DNA for capturing gold nanoparticles. Gold nanoparticles were successfully arranged into parallel lines consistent with our design. Within each line, a single chain of close-packed gold nanoparticles was observed. The average distance between particles with a line is about 2 nanometers, except for some locations with clear defects (Fig. 6b).

Two parallel gold-nanoparticle monolayers were assembled on the XY-4H×4H×64-cuboid crystal in Fig. 4c. The crystals display poly-T sequences at each helix-end on both surfaces for capturing 10-nanometer gold nanoparticles functionalized with poly-A strands (Fig. 6d, inset). The average distance between particles appeared to be about 1 to 2 nanometers (Fig. 6d). The structures sometimes curved on the edges (Fig. 6e). The edge-to-edge distance between the two monolayers of gold nanoparticles were measured to be about 25 nm, consistent with the designed crystal thickness.

Aligning gold nanoparticles into micron-scale ordered low-dimensional arrays is required in diverse plasmonic applications. In particular, nanoparticle arrays with less than 2 nm face-to-face spacing are expected to exhibit strong plasmonic coupling.[6] With DNA nanostructures as templates, gold nano particles have been arranged into chiral,[3] linear,[7,8] and branched patterns.[9,10] However, most of these structures are discrete sub-100 nm structures, which lacks long-range ordering at micron scale. In addition, decreasing the interparticle spacing down to 2 nm is also challenging. DNA crystals provide unique opportunity towards these challenges. By varying the surface distribution of poly-T binding sites, gold nanoparticles were programmed with different 2D patterns at micron scale, from close-packing patterns to arrays of gold nanoparticle chains with 20-nm inter-chain spacing. The periodicity of poly-T binding site is 2.5 nm on DNA crystals, which produced the inter-particle spacing to around 2 nm.

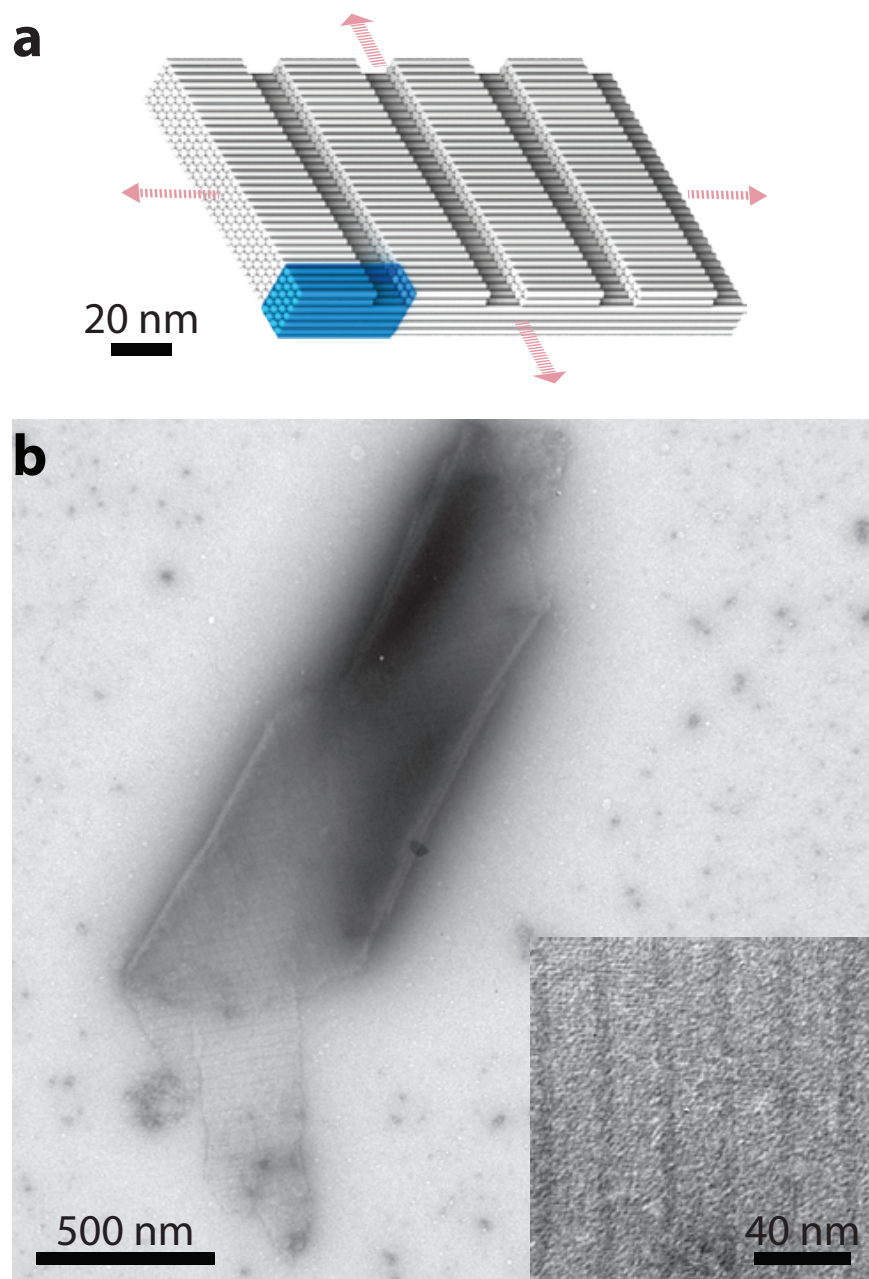## S8.2 Design and TEM images of a ZX-4H×6H×96B-channel crystal

Fig. S44. The design and TEM images of a ZX-4H×6H×96B-channel crystal. a, Design of the ZX-4H×6H×96B-channel crystal. A unit cell of the crystal is denoted using a blue-colored box. **b,** TEM images of the ZX-4H×6H×96B-channel crystal.

In this ZX-4H×6H×96B-channel crystal design, the channels are two-helix (5 nanometers) in depth. Every 5′ or 3′ ends of helices displays a poly-T single stranded overhang. See Fig. S76 for the strand diagram.

S9 Strand diagrams

S9.1 Strand diagrams of the Z-crystals
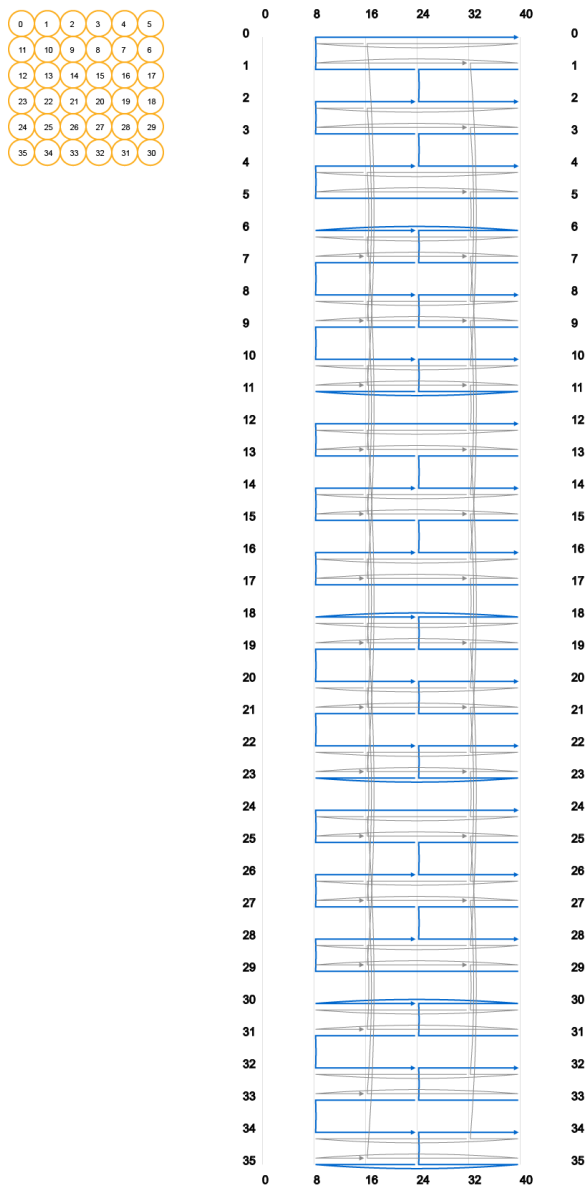
Fig. S45. Strand diagram of the Z-6H×6H×32B-cuboid crystal. Zoom-in to see details.
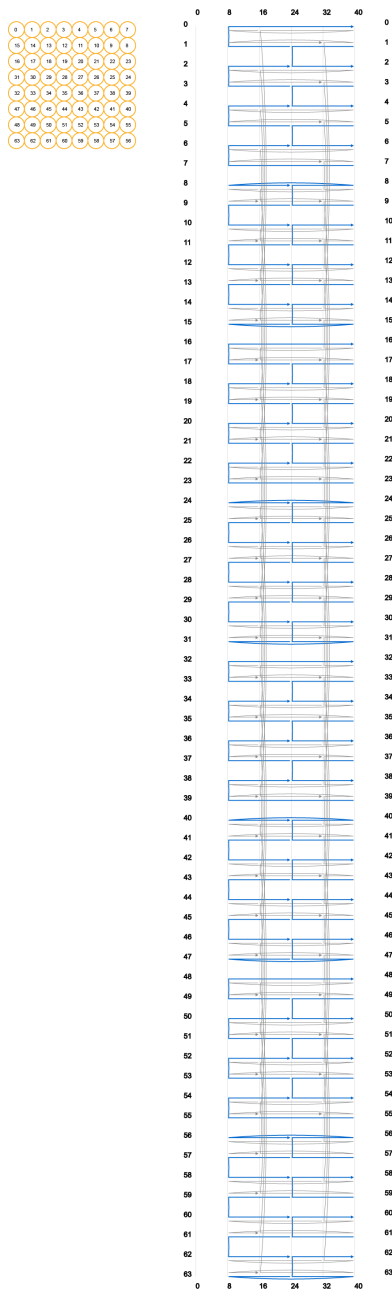
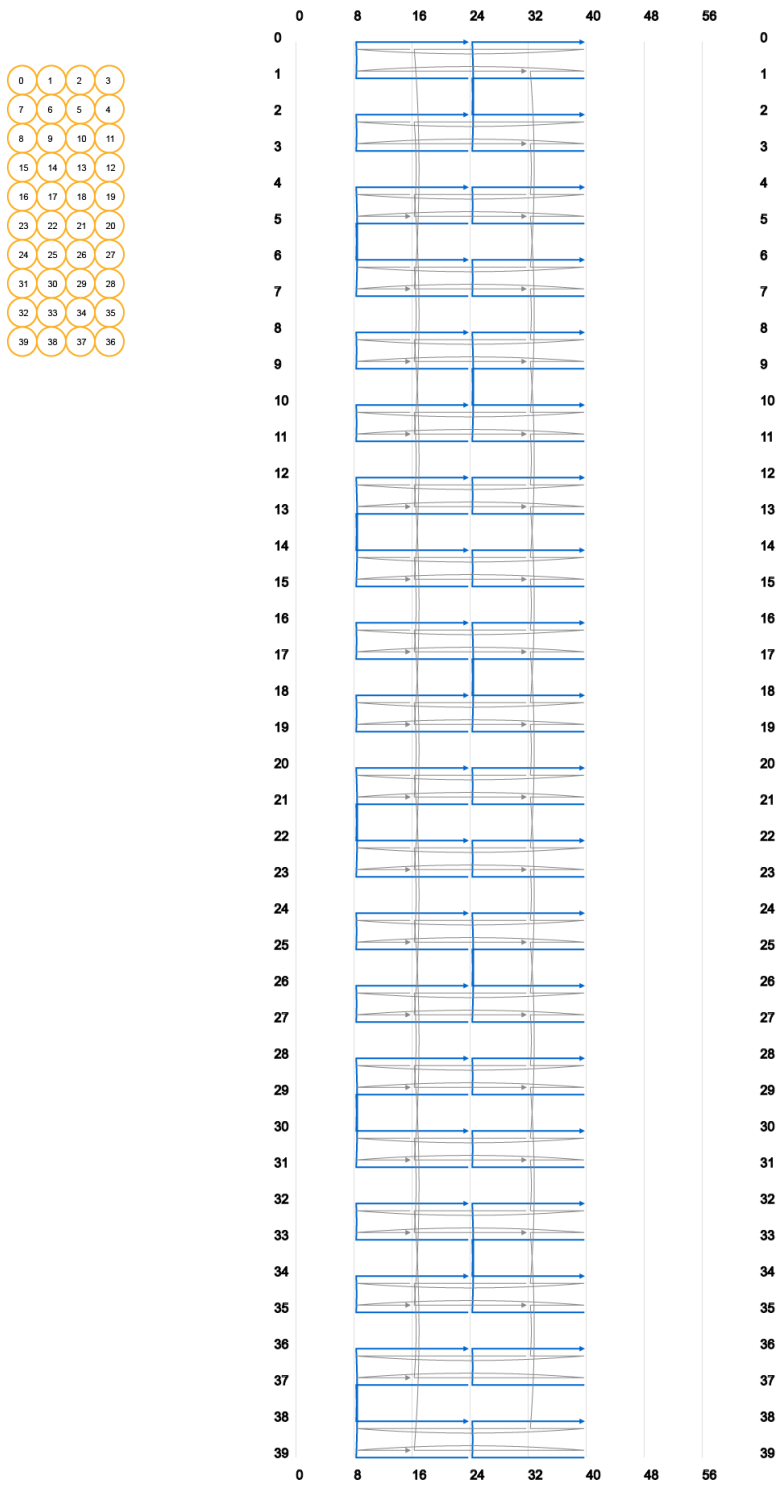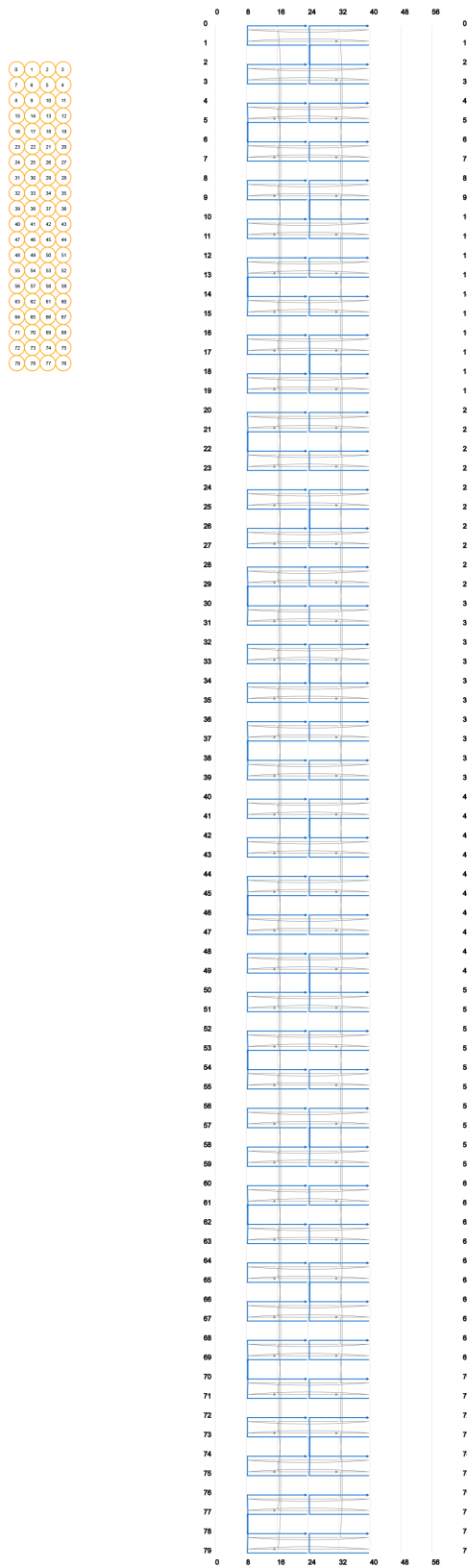**Fig. S46. Strand diagram of the Z-8H×8H×32B-cuboid crystal.** Zoom-in to see details.
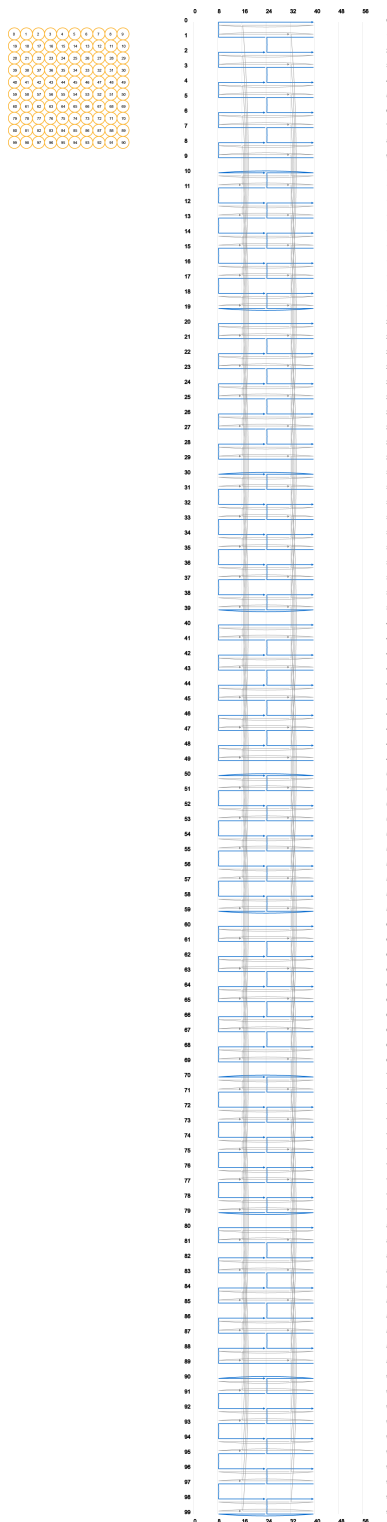
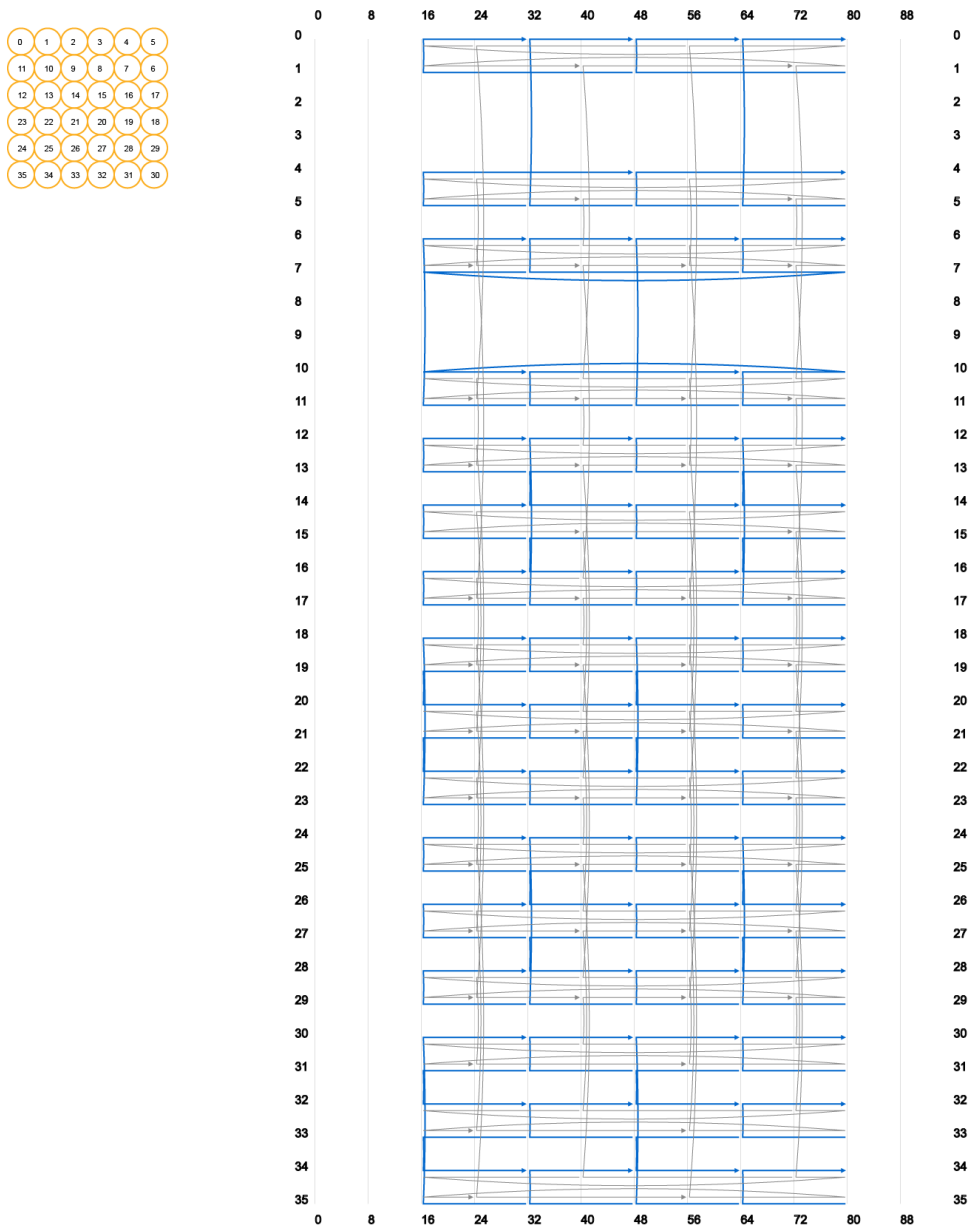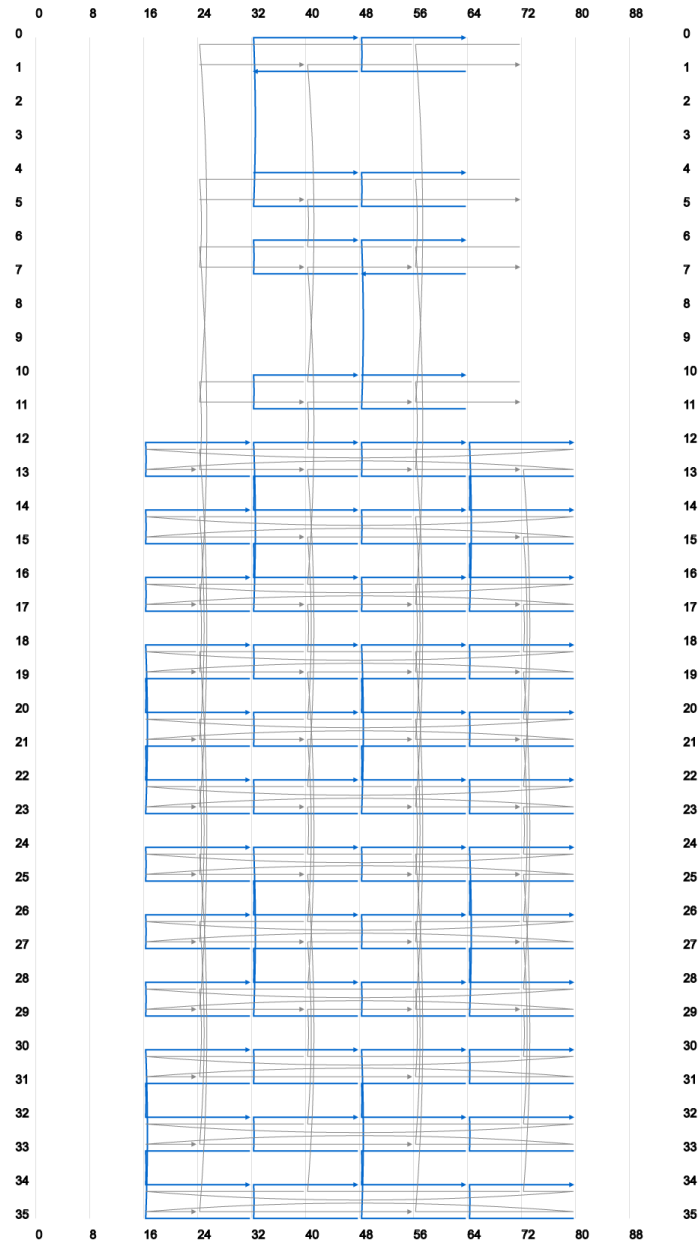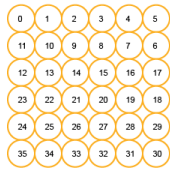**Fig. S47. Strand diagram of the Z-10H×10H×32B-cuboid crystal.** Zoom-in to see details.
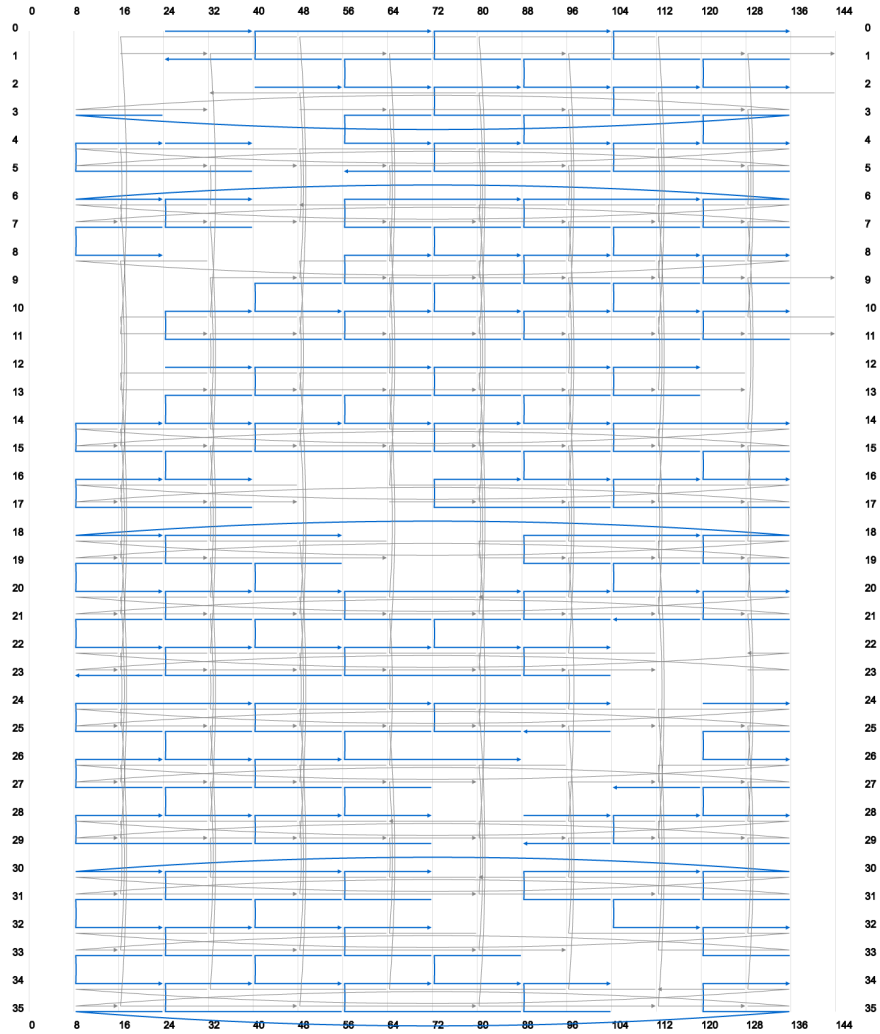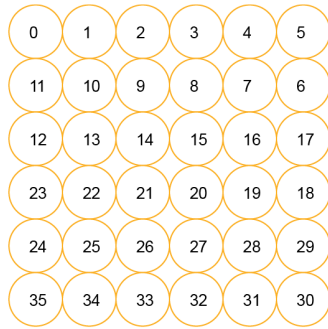
Fig. S48. Strand diagram of the Z-6H×6H×128B-spiral crystal. Zoom-in to see details.
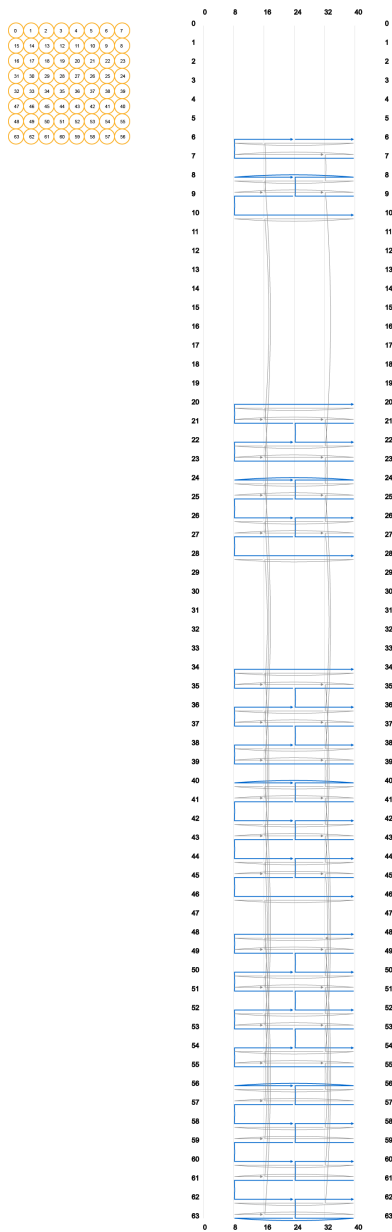
Fig. S49. Strand diagram of the Z-43H×32B-triangle crystal. Zoom-in to see details.
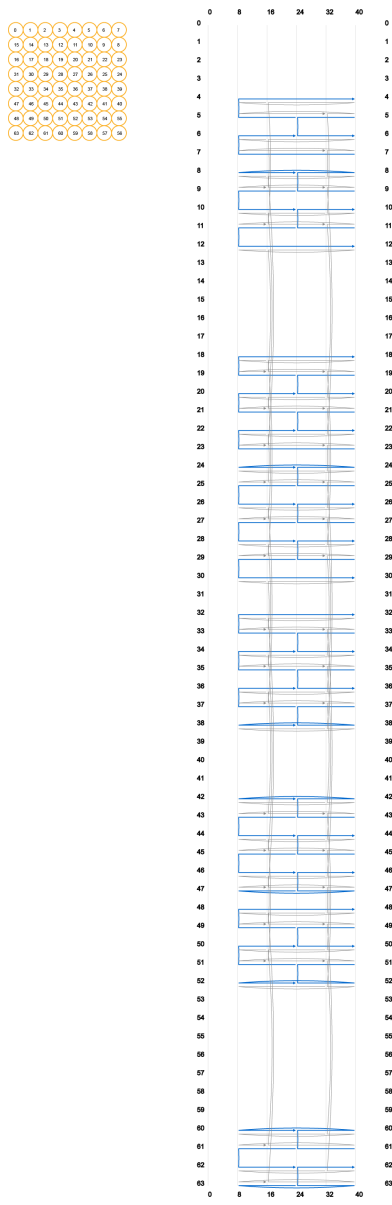
Fig. S50. Strand diagram of the Z-44H×32B-hexagon crystal. Zoom-in to see details.
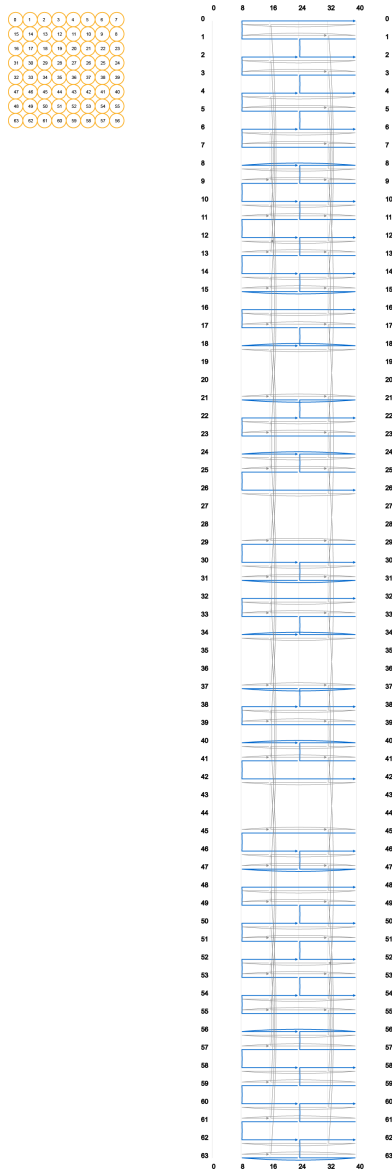
Fig. S51. Strand diagram of the Z-56H×32B-tunnel crystal. Zoom-in to see details.
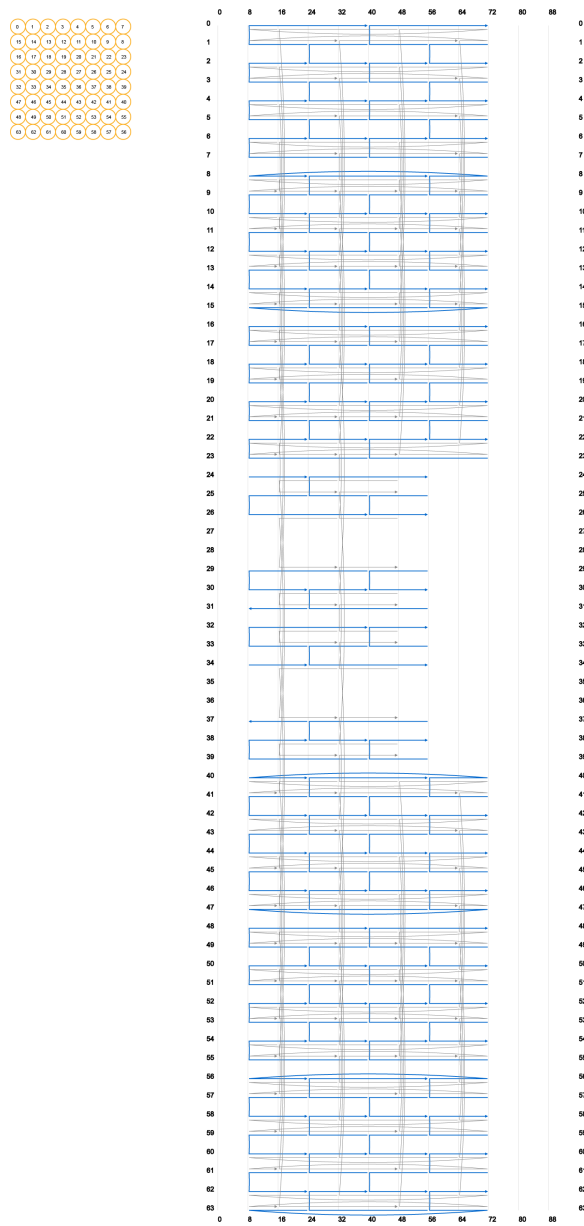
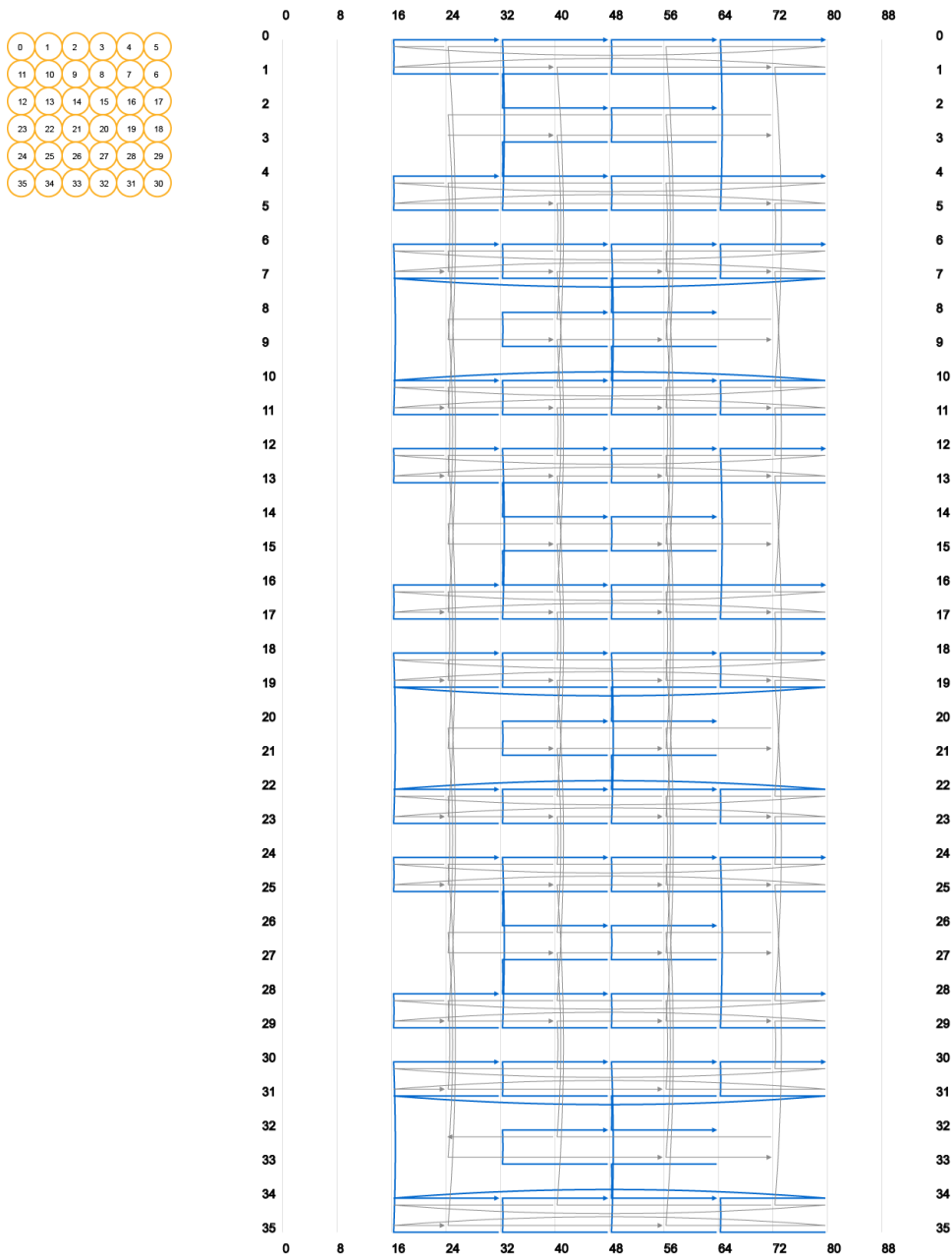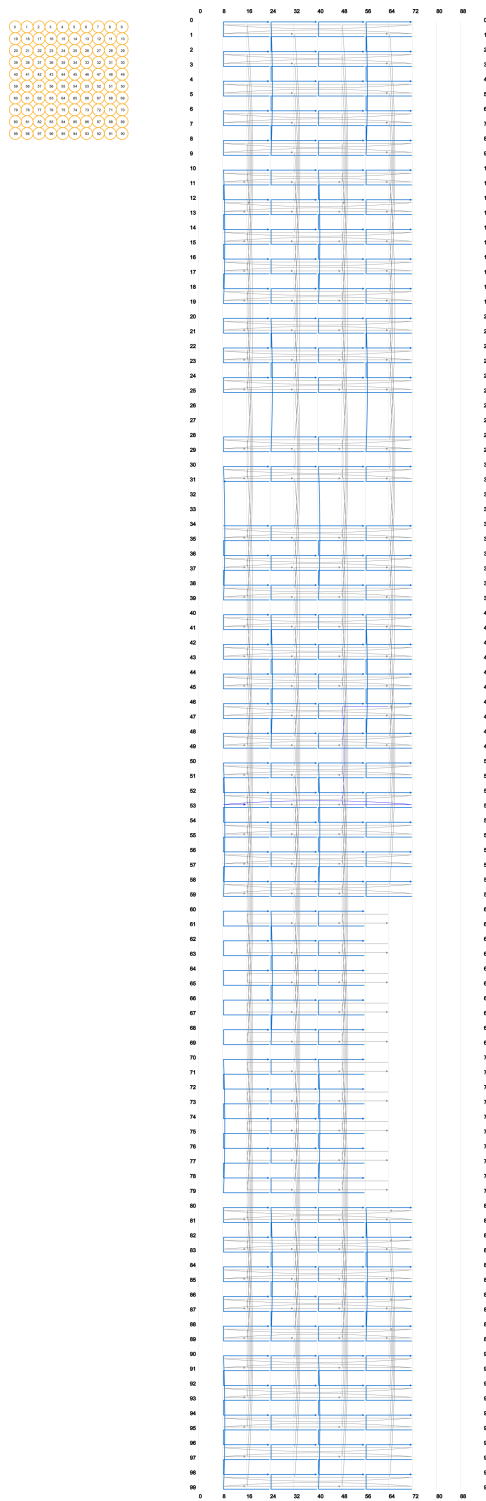**Fig. S52. Strand diagram of the Z-60H×64B-tunnel crystal.** Zoom-in to see details.
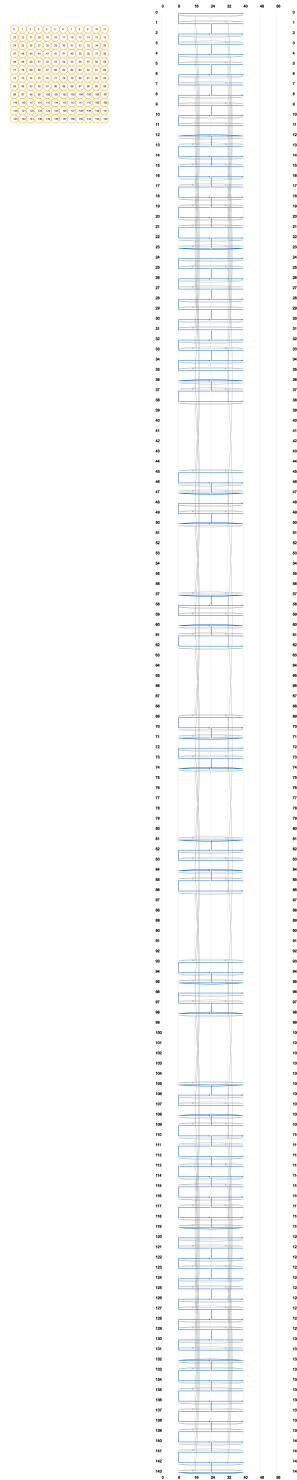
Fig. S53. Strand diagram of the Z-108H×32B-tunnel crystal. Zoom-in to see details.
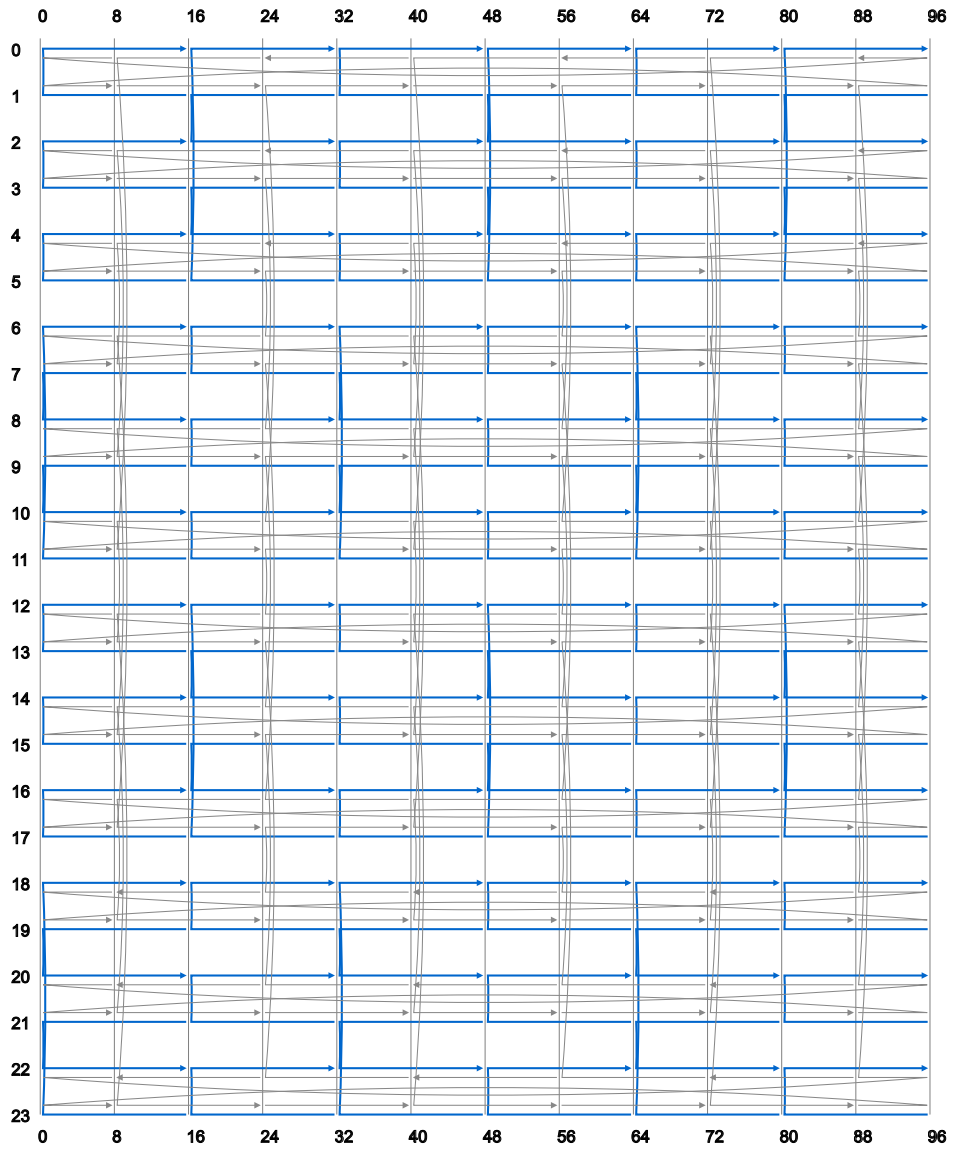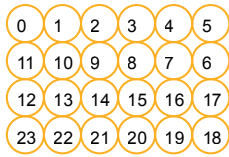
S9.2 Strand diagrams of the ZX-crystals
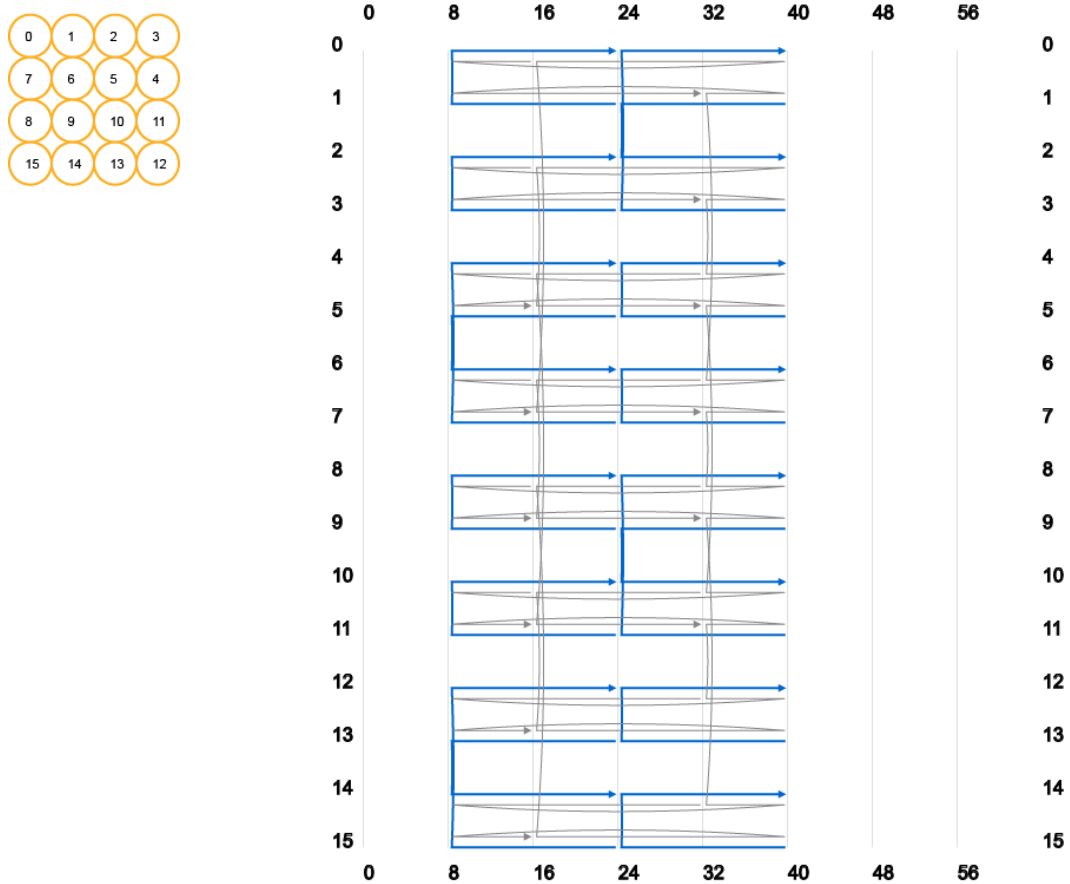
Fig. S54. Strand diagram of the ZX-4H×4H×32B-cuboid crystal. Zoom-in to see details.
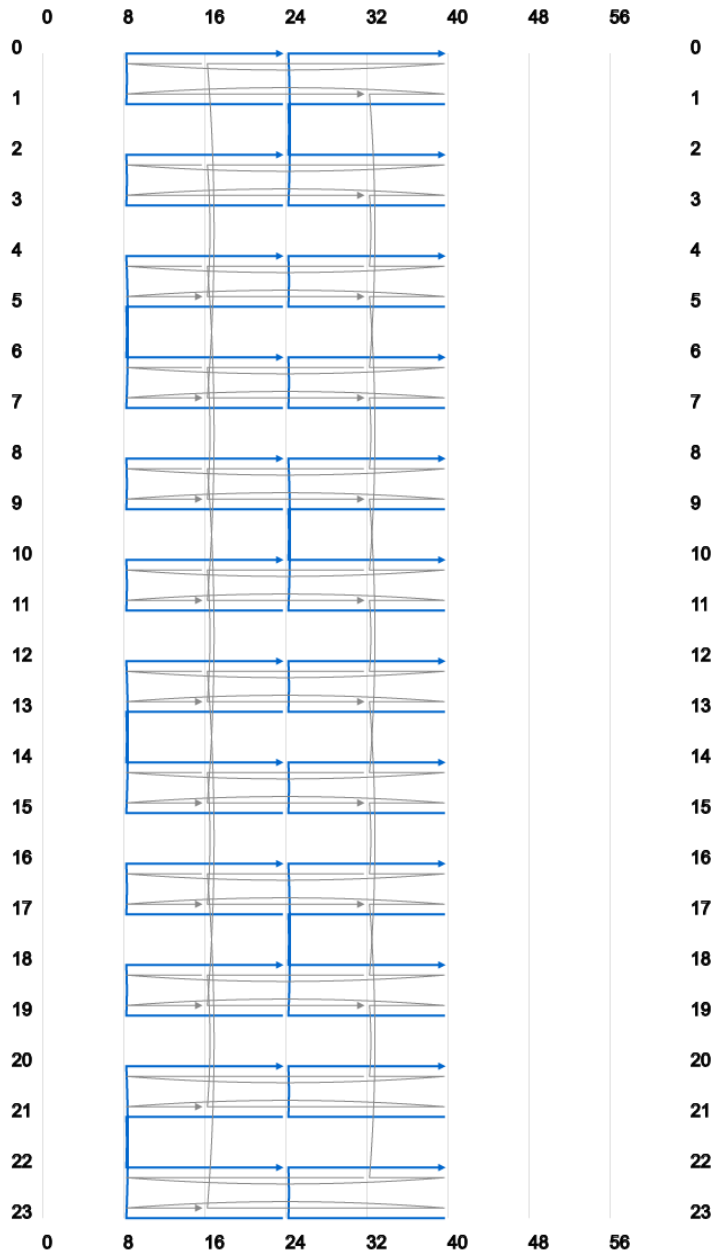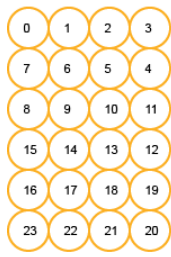
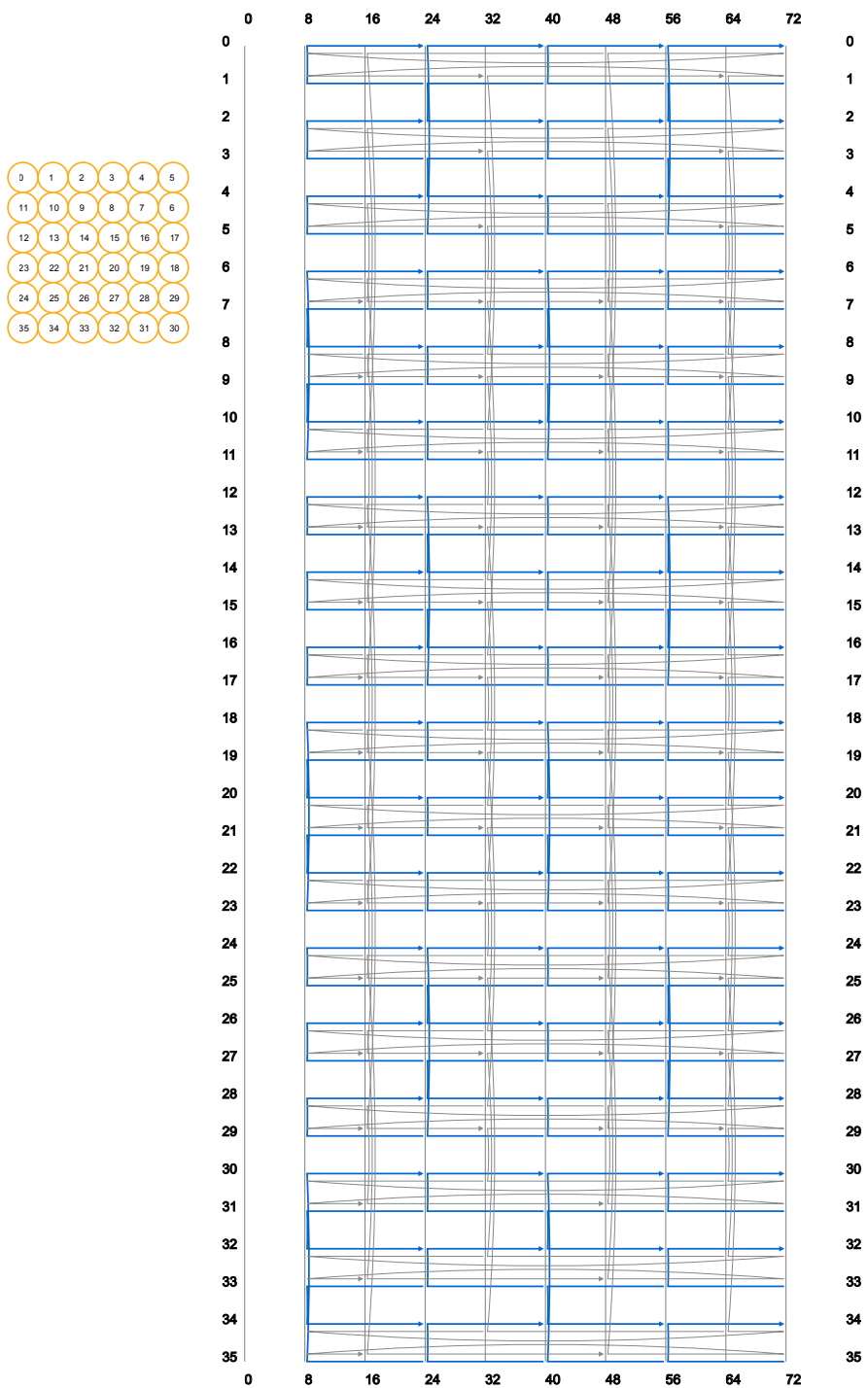**Fig. S55. Strand diagram of the ZX-4H×6H×32B-cuboid crystal.** Zoom-in to see details.
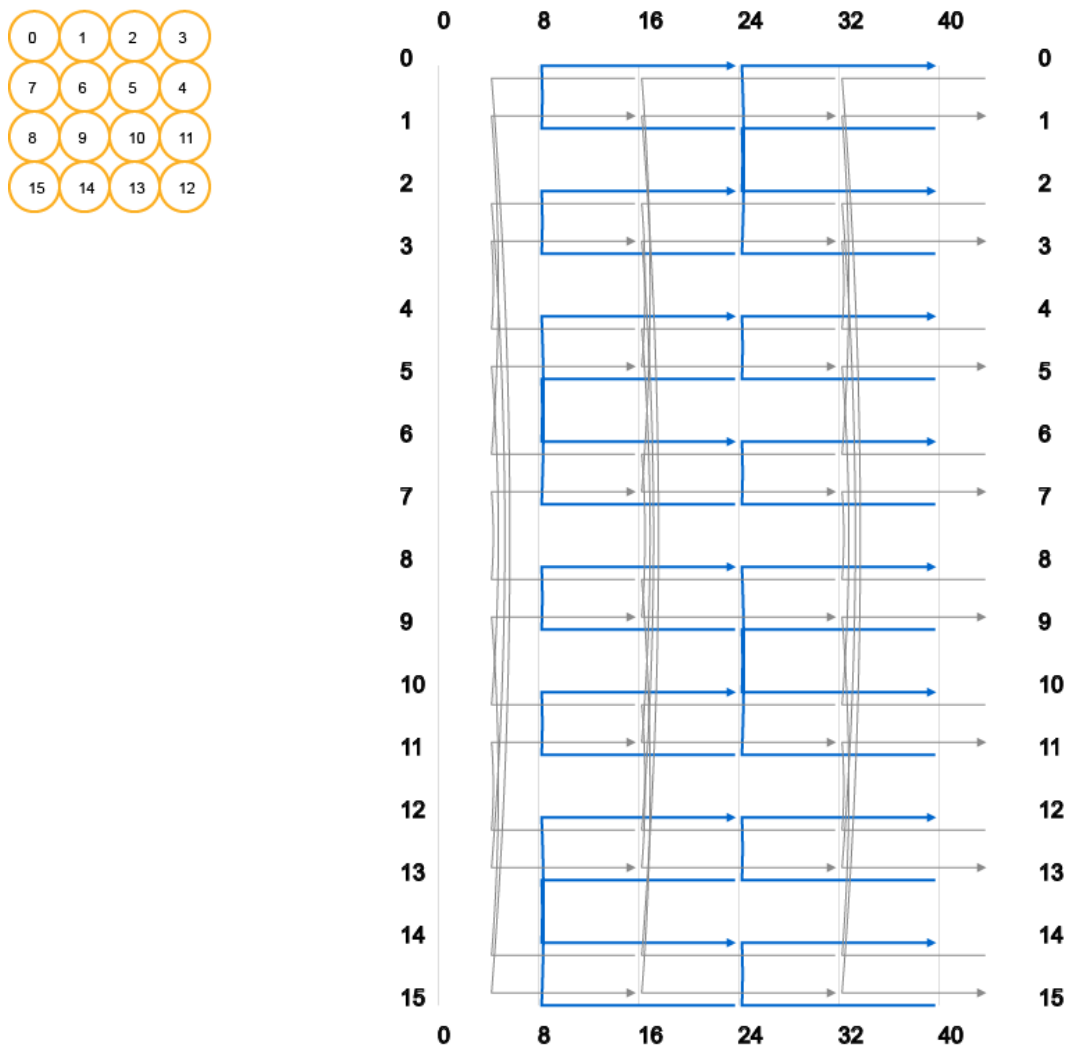
Fig. S56. Strand diagram of the ZX-4H×10H×32B-cuboid crystal. Zoom-in to see details.

Fig. S57. Strand diagram of the ZX-4H×20H×32B-cuboid crystal. Zoom-in to see details.

Fig. S58. Strand diagram of the ZX-32H×64B-channel crystal. Zoom-in to see details.

Fig. S59. Strand diagram of the ZX-32H×64B-cross-channel crystal. Zoom-in to see details.

Fig. S60. Strand diagram of the ZX-6H×6H×64B-pore crystal. Zoom-in to see details.

Fig. S61. Strand diagram of the ZX-96H×64B-cross-tunnel crystal. Zoom-in to see details.

Fig. S62. Strand diagram of the ZX-6H×4H×96B-cuboid crystal. Zoom-in to see details.

Fig. S63. Strand diagram of the ZX-6H×6H×64B-cuboid crystal. Zoom-in to see details.

S9.3 Strand diagrams of the XY-crystals

Fig. S64. Strand diagram of the XY-4H×4H×32B-tube crystal. Zoom-in to see details.
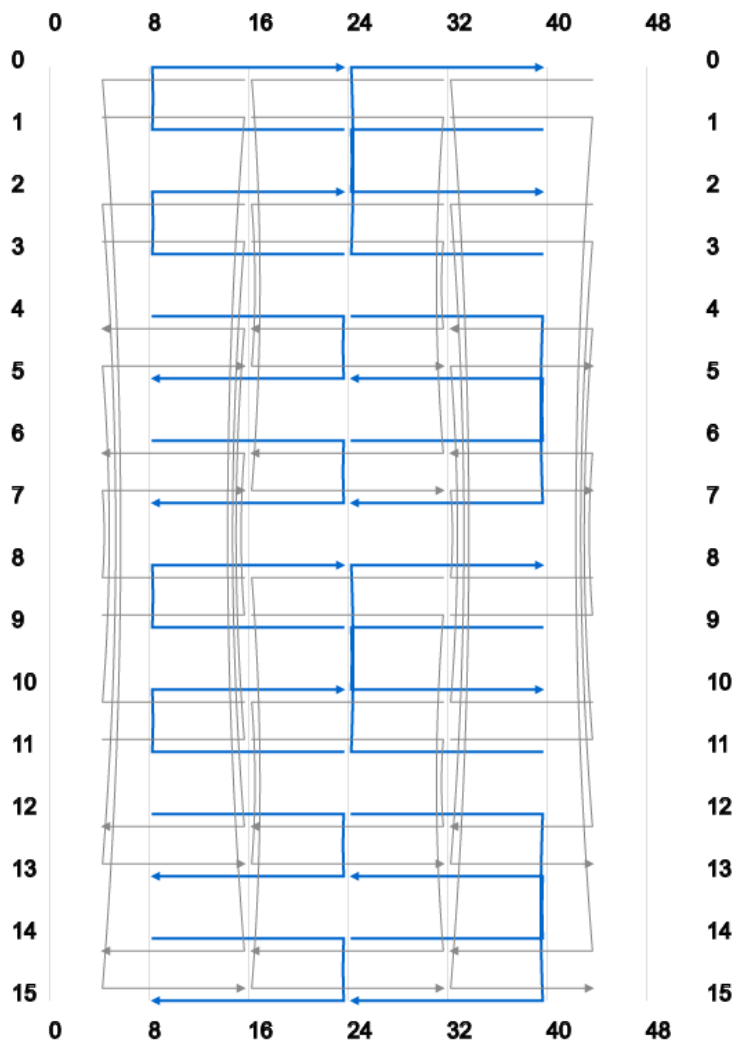
Fig. S65. Strand diagram of the XY-4H×4H×32B-cuboid crystal using alternating DNA-bricks. Zoom-in to see more details.
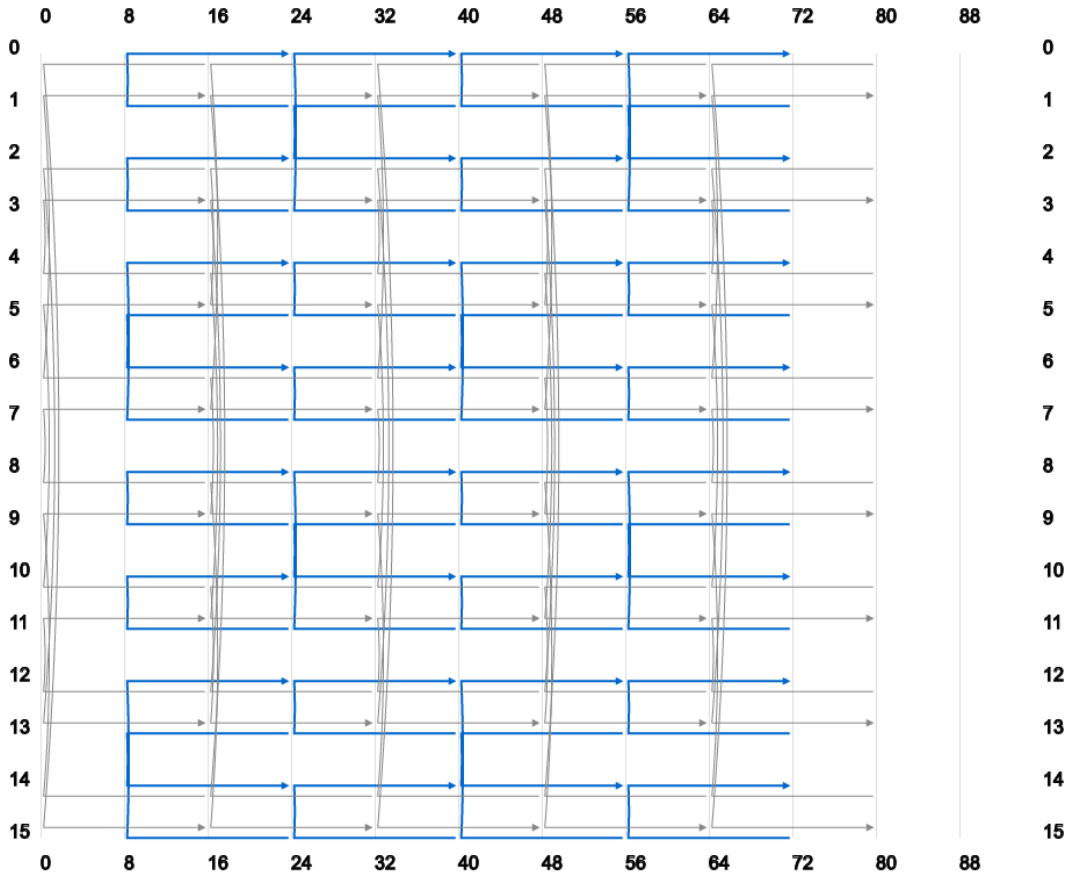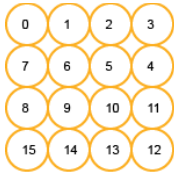
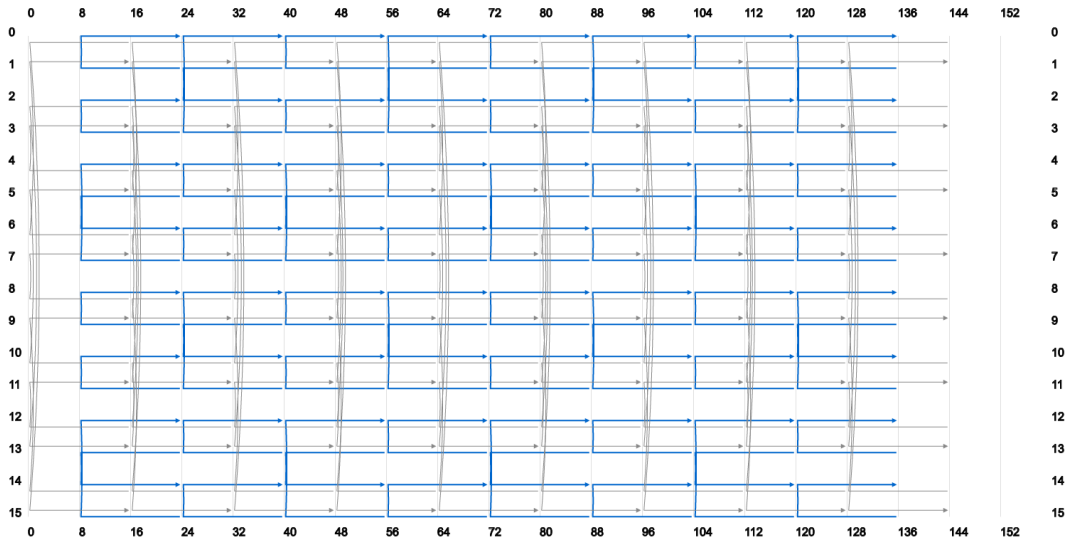**Fig. S66. Strand diagram of the XY-4H×4H×64B-cuboid crystal.** Zoom-in to see more details.

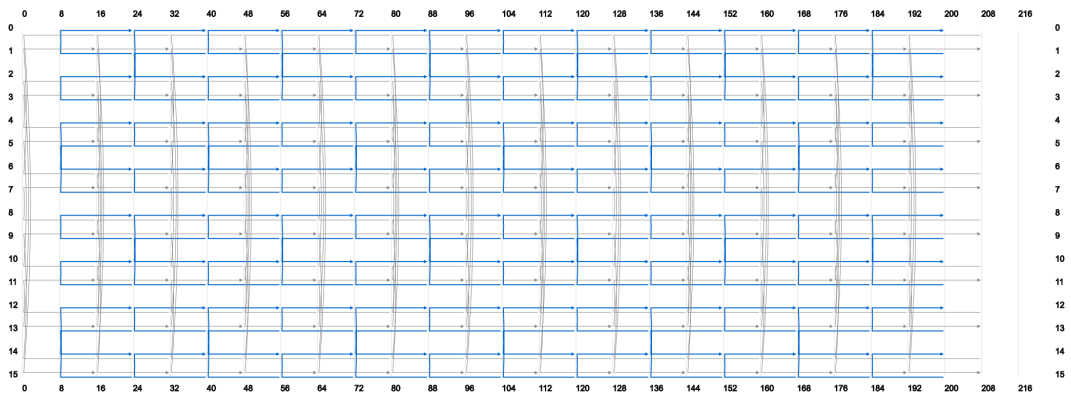**Fig. S67. Strand diagram of the XY-4H×4H×128B-cuboid crystal.** Zoom-in to see more details.

Fig. S68. Strand diagram of the XY-4H×4H×192B-cuboid crystal. Zoom-in to see more details.

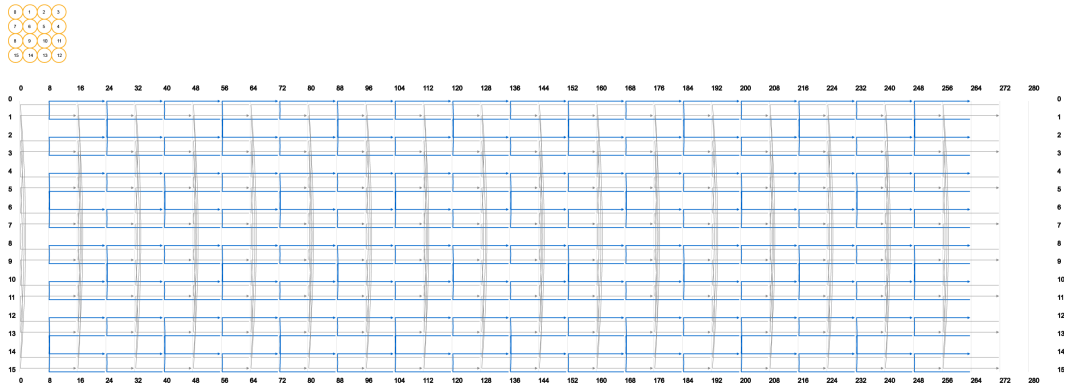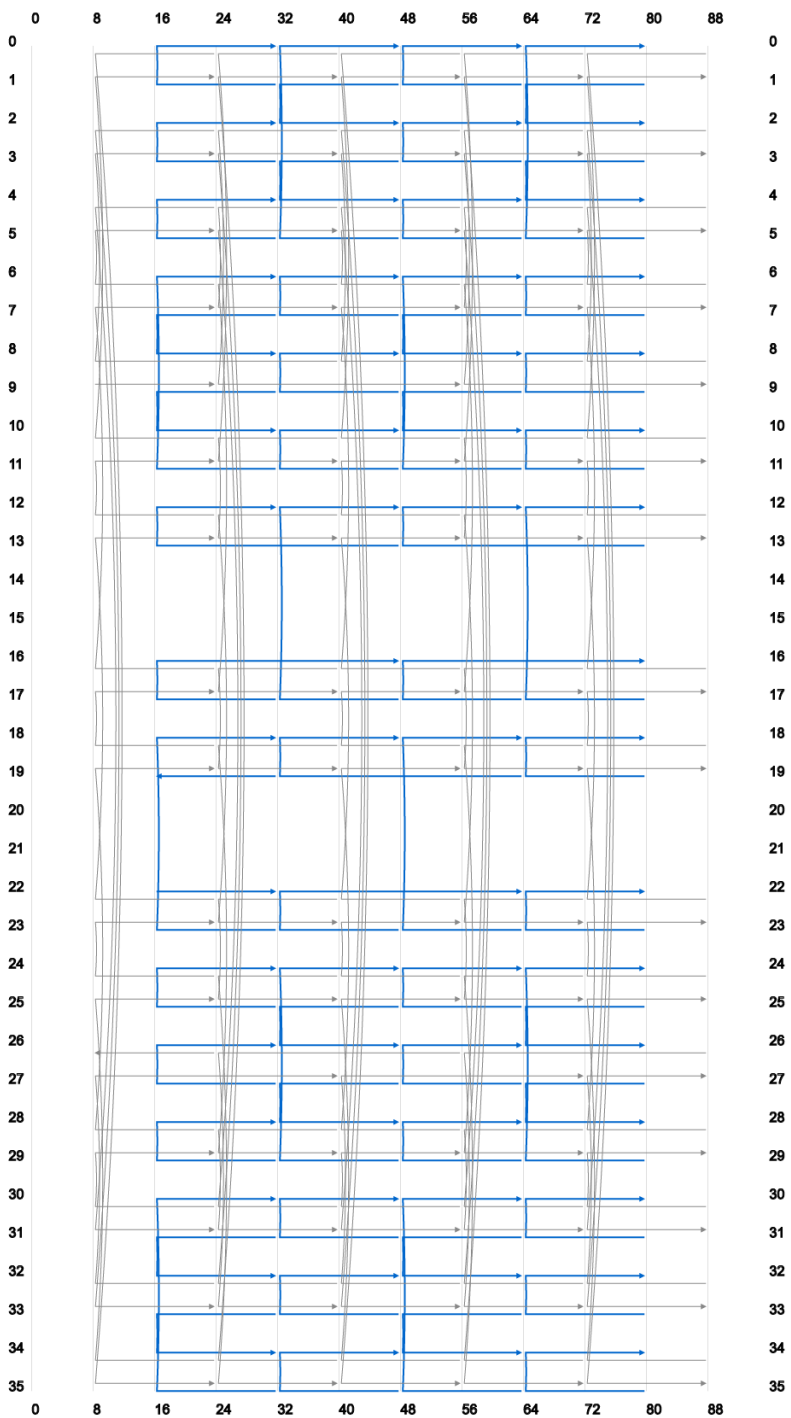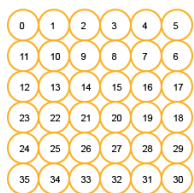**Fig. S69. Strand diagram of the XY-4H×4H×256B-cuboid crystal.** Zoom-in to see more details.

Fig. S70. Strand diagram of the XY-32H×64B-pore crystal. Zoom-in to see more details.
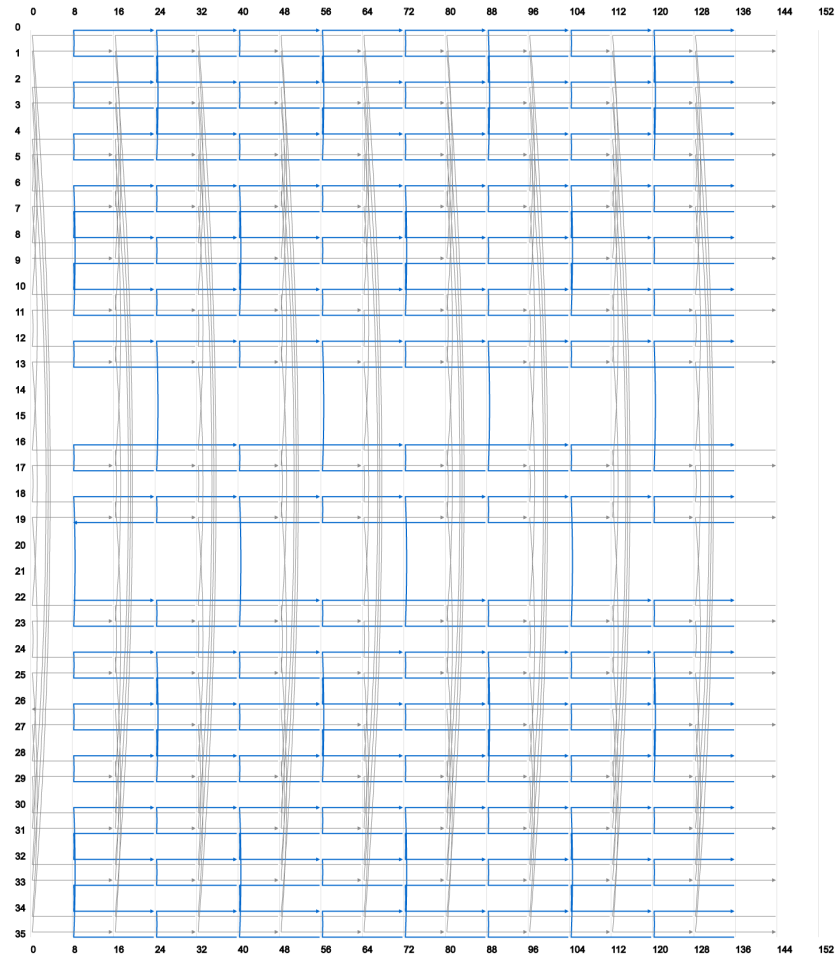
Fig. S71. Strand diagram of the XY-32H×128B-pore crystal. Zoom-in to see more details.
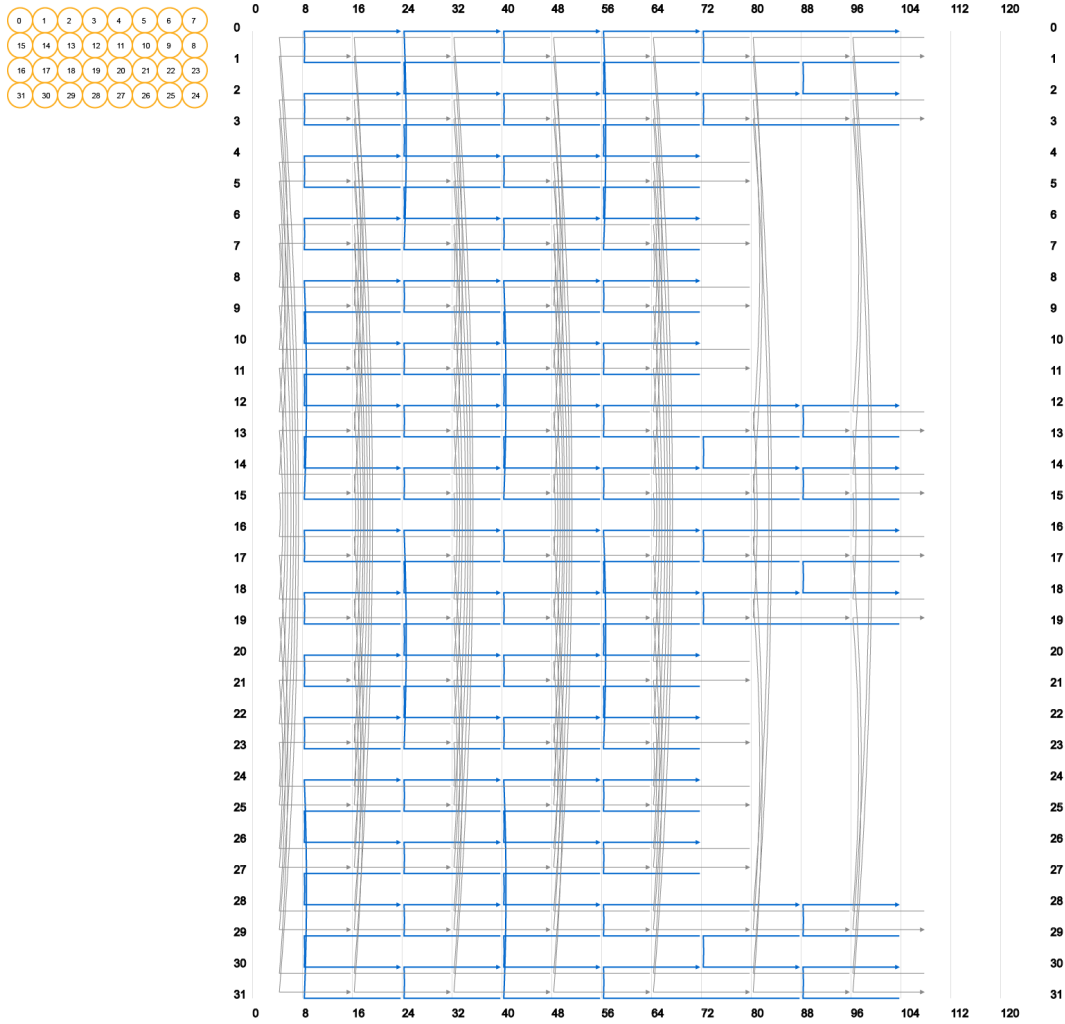
Fig. S72. Strand diagram of the XY-8H×4H×96B-channel. Zoom-in to see more details.
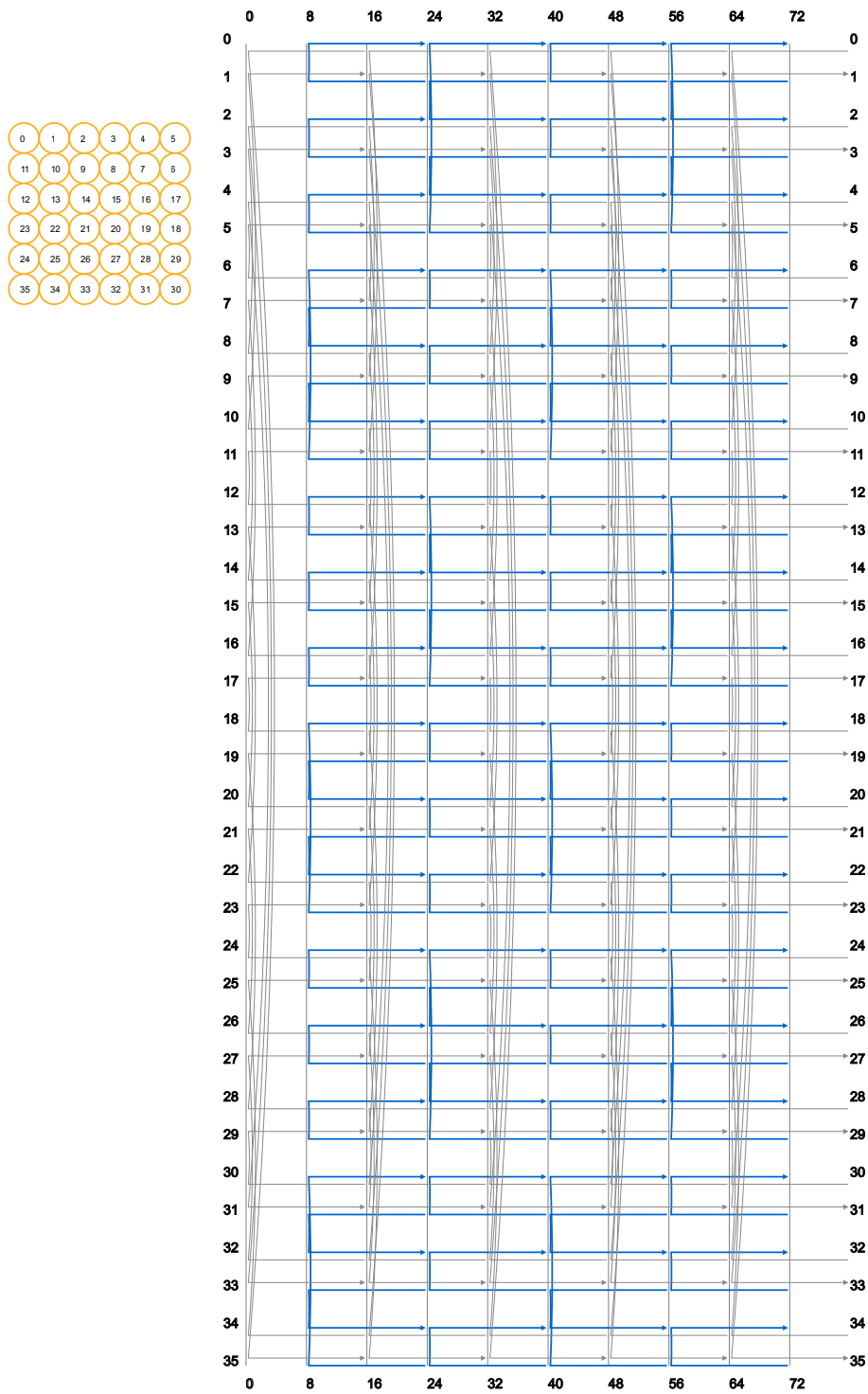
Fig. S73. Strand diagram of the XY-6H×6H×64B-cuboid crystal. Zoom-in to see details.

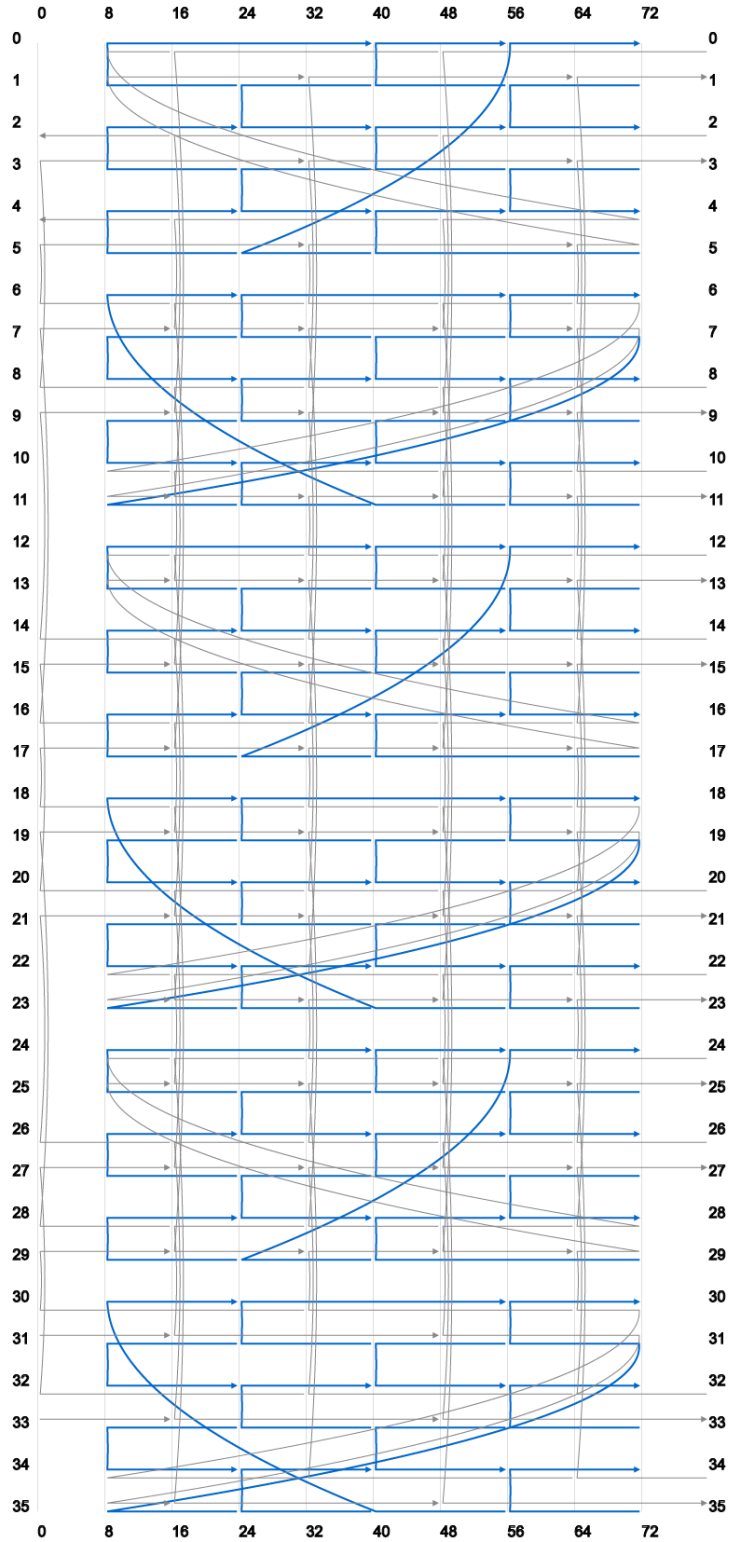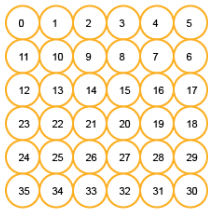## S9.4 Strand diagram of offset ZX-crystals

Fig. S74. Strand diagram of the offset-ZX-6H×6H×64B-cuboidcrystal. Zoom-in to see details.

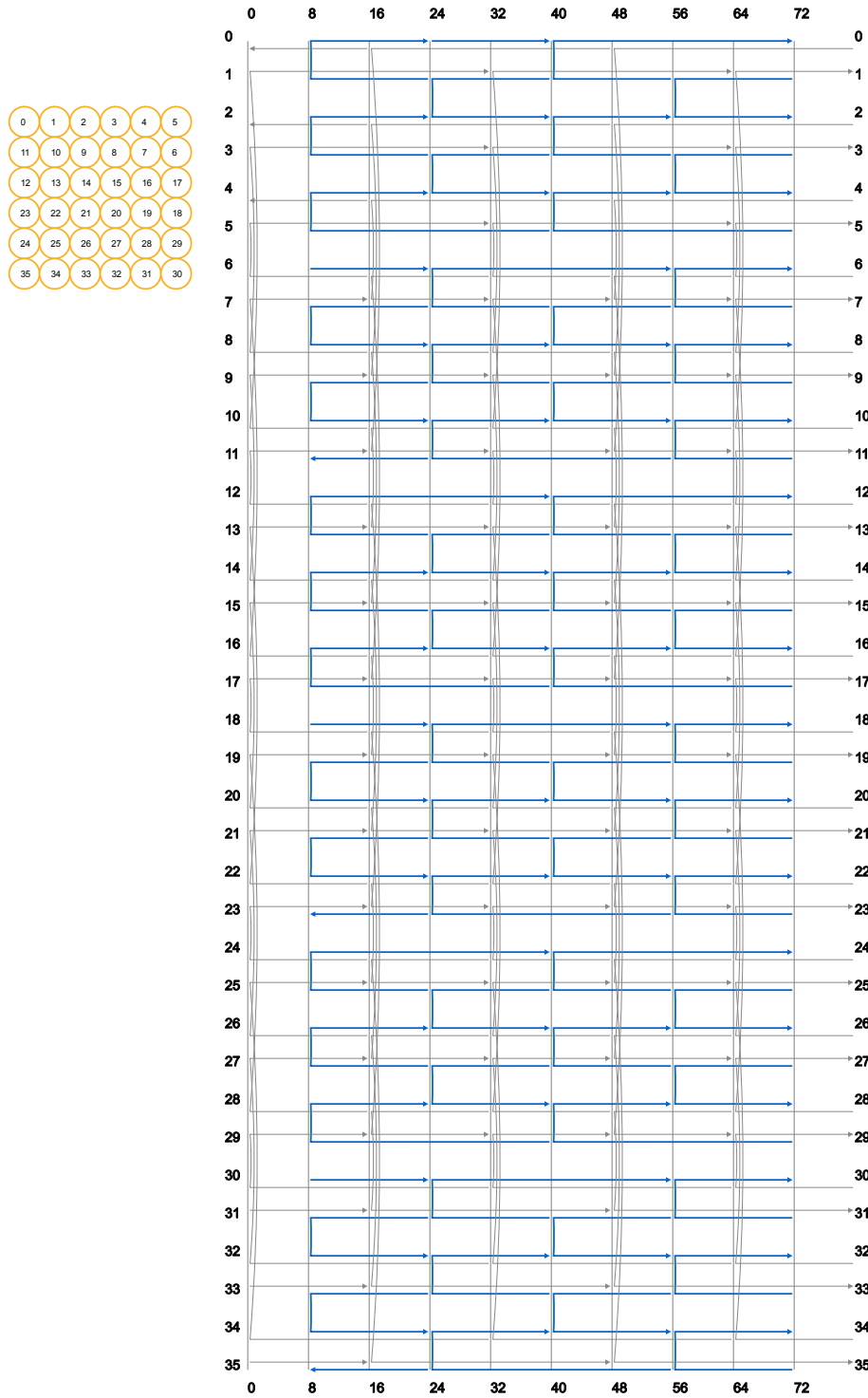**Fig. S75. Strand diagram of the 6H×6H×64B-cuboid.** Zoom-in to see details.

S9.6   Strand diagram of the ZX-4H×6H×96B-channel crystal for patterning gold particles
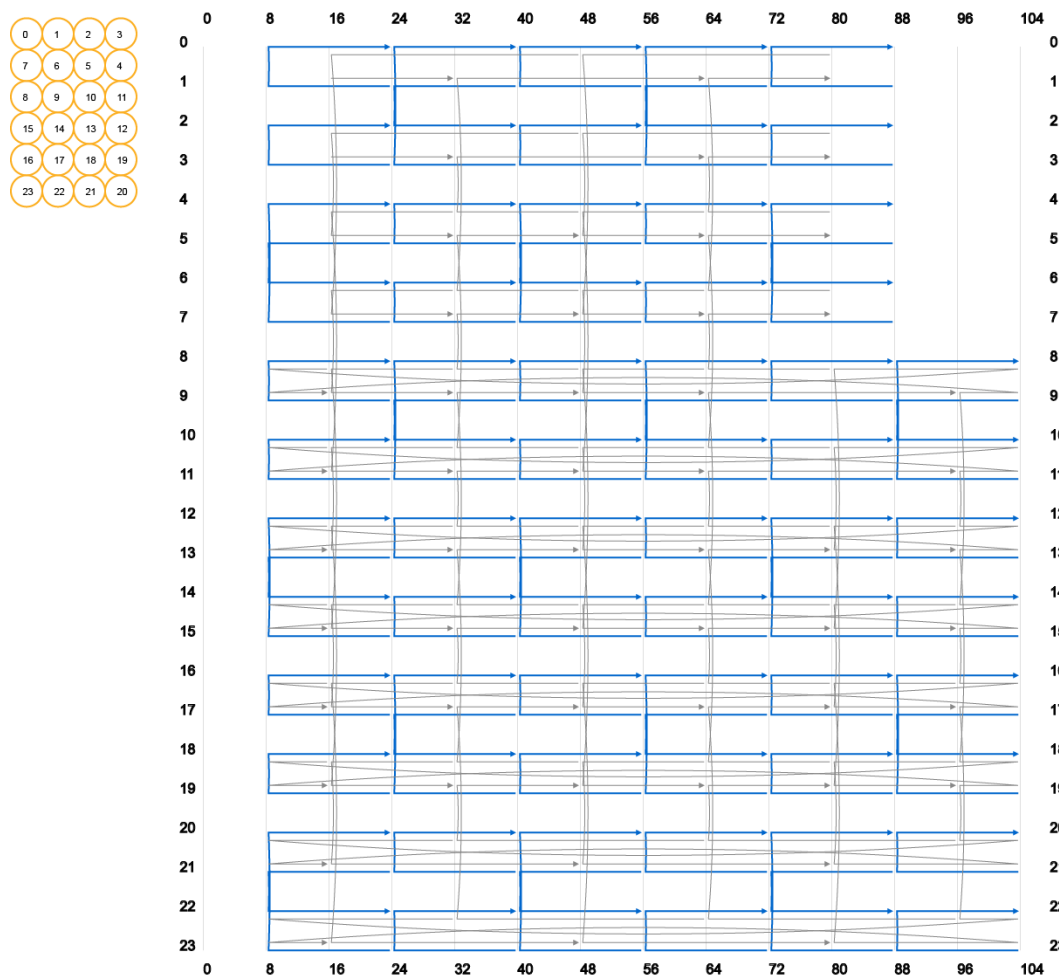

Fig. S76. Strand diagram of the ZX-4H×6H×96B-channel crystal. Zoom-in to see details.

References

1. Liu, W, Zhong, H & Seeman, Nadrain C. Crystalline two dimensional DNA origami arrays. *Angew. Chem. Int. Ed.* **50**, 264–267 (2011).
2. Aldaye, F. A. & Sleiman, H. F. Sequential self-assembly of a DNA hexagon as a template for the organization of gold nanoparticles. *Angew. Chem. Int. Ed.* **45**, 2204–2209 (2006).
3. Kuzyk, A. *et al.* DNA-based self-assembly of chiral plasmonic nanostructures with tailored optical response. *Nature* **483**, 311–314 (2012).
4. Acuna, G P *et al.* Fluorescence enhancement at docking sites of DNA-directed self-assembled nanoantennas. *Science* **338**, 506–510 (2012).
5. Sharma, J. *et al.* Control of self-assembly of DNA tubules through integration of gold nanoparticles. *Science* **323**, 112–116 (2009).
6. Tan, S. F. *et al.* Quantum plasmon resonances controlled by molecular tunnel junctions. *Science* **343**, 1496–1499 (2014).
7. Deng, Z., Tian, Y., Lee, S. H., Ribbe, A. E. & Mao, C. DNA-encoded self-assembly of gold nanoparticles into one-dimensional arrays. *Angew. Chem. Int. Ed.* **44**, 3582–3585 (2005).
8. Ding, B. *et al.* Gold nanoparticle self-similar chain structure organized by DNA origami. *J. Am. Chem. Soc.* **132**, 3248–3249 (2010).
9. Sharma, J., Chhabra, R., Liu, Y., Ke, Y. G. & Yan, H. DNA-templated self-assembly of two-dimensional and periodical gold nanoparticle arrays. *Angew. Chem. Int. Ed.* **45**, 730–735 (2006).
10. Zhang, J., Liu, Y., Ke, Y. & Yan, H. Periodic Square-Like Gold Nanoparticle Arrays Templated by Self-Assembled 2D DNA Nanogrids on a Surface. *Nano Lett.* **6**, 248–251 (2006).